Development and Characterization of a Diverging Cusped Field Thruster and a Lanthanum Hexaboride Hollow Cathode

by

Daniel George Courtney

Submitted to the Department of Aeronautics and Astronautics
in partial fulfillment of the requirements for the degree of

Master of Science in Aeronautics and Astronautics

at the

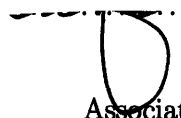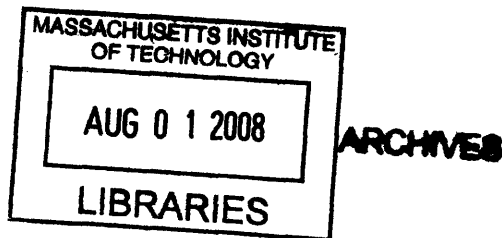MASSACHUSETTS INSTITUTE OF TECHNOLOGY
[June 2008]
May 2008

Author ....
Department of Aeronautics and Astronautics
May 23, 2008

Certified by ......
Manuel Martínez-Sánchez
Professor
Thesis Supervisor

Accepted by ....
David L. Darmofal
Professor
Associate Department Head
Chair, Committee on Graduate Students

Development and Characterization of a Diverging Cusped Field Thruster and a Lanthanum Hexaboride Hollow Cathode

by

Daniel George Courtney

Submitted to the Department of Aeronautics and Astronautics
on May 23, 2008, in partial fulfillment of the
requirements for the degree of
Master of Science in Aeronautics and Astronautics

Abstract

A low power, magnetically confined plasma thruster has been developed and undergone preliminary characterization. The design employs cusped magnetic fields arranged in a divergent fashion to confine electron flow to an anode while providing efficient acceleration of an ion beam, similar to traditional Hall type thrusters. The design, referred to as a Diverging Cusped Field (DCF) thruster, employs aspects of both existing cusped field thrusters and traditional Hall thrusters while including several unique design features aimed at increasing performance. In addition to supporting competitive thrust and efficiency performance, the DCF magnetic arrangement confines the discharge plasma away from the channel walls in order to reduce wall erosion and promote long lifetimes.

The thruster has demonstrated performance levels comparable to typical commercial Hall thrusters. Specifically, a nominal anode efficiency of 44.5% has been achieved while providing $13.4mN$ of thrust at xenon mass flow rate of $8.5sccm$ and consuming $242W$ of anode power. The corresponding nominal specific impulse was $1640s$. Preliminary observations suggest that the arrangement successfully contains the plasma away from the channel walls throughout the majority of the discharge chamber. Unique aspects of the DCF discharge include an apparent bi-modal operating spectrum and an irregular beam profile. While efficient operation has been observed in both operating modes, the transitions are shown to be accompanied by variations in both ionization efficiency and ion energy distribution. The emitted plume was observed to be conical in shape, with a hollow interior and concentrated ion flux diverging at roughly $32°$.

In addition to the DCF thruster, a small lanthanum hexaboride (LaB_6) hollow cathode has been developed for use with plasma thrusters within the MIT Space Propulsion Laboratory. Lanthanum hexaboride was selected due to its insensitivity to impurity poisoning and resultant suitability for experiments which require frequent exposure to atmospheric conditions. The cathode was designed based on larger LaB_6 cathodes developed at NASA JPL. Significant alterations to the design included a threaded ceramic heater and the inclusion of a thin radiation shield between the cathode tube and keeper electrode. Total current levels between $0.75A$ and $2.5A$ were sustained with the external heater deactivated after an initial ignition procedure. Typically the insert had reached temperatures suitable for emission after roughly 30 minutes of external heating at up to $110W$ of heater power.

Thesis Supervisor: Manuel Martínez-Sánchez
Title: Professor

Acknowledgments

Contents

List of Figures

13

14

15

List of Tables

Chapter 1

Introduction

Current spacecraft propulsion methods can be divided into two broad categories, chemical and electric propulsion. Chemical thrusters rely on the release of energy occurring during chemical reactions. The resultant high temperature products are then expanded through a nozzle and expelled out of the engine. Examples of these thrusters include simple solid rocket boosters and more complex liquid bi-propellant engines. Such devices have been, and continue to be, the primary source of propulsion for launch vehicles. The reason is that, in general, chemical thrusters are capable of very high thrust at the expense of a low specific impulse. Specific impulse, I_{sp}, is defined as the ratio of thrust, T to mass flow, $\dot{m}$, divided by the acceleration due to gravity at surface of the earth. ($g = 9.81m/s^2$).

$$I_{sp} = \frac{T}{g\dot{m}} \tag{1.1}$$

It is clear from equation 1.1 that a high specific impulse is desirable as it implies relatively high thrust for the amount of fuel required. Typical chemical thrusters have a specific impulse less than $450s$. The advantages of high I_{sp} can be seen more readily by equation 1.2 which gives the propellant to initial mass ratio for a given ΔV and specific impulse.

$$\frac{M_p}{M_0} = 1 - e^{-\frac{\Delta V}{gI_{sp}}} \tag{1.2}$$

The mission ΔV is simply the change in velocity that the thruster is to impart on the spacecraft. From equation 1.2 it is clear that for high specific impulse, the propellant mass decreases.

Electric propulsion thrusters use electrical energy to accelerate the propellant and generate thrust. They include electrothermal thrusters where electric energy is used to simply heat the working gas and, more complex plasma thrusters which accelerate charged particles directly. In general they offer high specific impulse, but often low thrust. Specifically specific impulses ranging from chemical thruster levels to beyond $5000s$ can be realized with electric propulsion. Thus, in situations where low thrust is acceptable but large ΔV is required, electric propulsion has a clear advantage over chemical propulsion. Application examples include satellite station keeping, primary propulsion for deep space missions and earth orbit transfers. For a review of the various forms and applications of electric propulsion, consult Martínez-Sánchez $et.$ al[8].

1.1 Electrostatic Propulsion

Electrostatic thrusters accelerate charged (usually positively) particles through a potential drop to generate a high velocity beam of ions. The reaction to this acceleration provides thrust on the spacecraft. Examples include grided ion thrusters, Hall thrusters and colloid thrusters amongst others[8].

Grided ion thrusters create a discharge plasma then accelerate ions through grids designed to admit ions but repel electrons. The resulting thrusters produce a relatively monoenergetic, collimated ion beam and operate efficiently at high specific impulse[8]. However; a significant drawback of grided ion thrusters is that beam current quickly becomes space charge limited through the accelerating grid[9]. The effect being a reduction in the thrust density which can be achieved using the thrusters. Applications of grided ion thrsuters include the NSTAR thruster which propelled the NASA Deep Space One spacecraft from 1998 to 2001[10].

Magnetically confined electrostatic thrusters, like Hall thrusters, accelerate ions through an imposed potential difference but do so within a quasi neutral plasma. The result is that such devices do not suffer from space charge limitation and therefore can achieve higher thrust densities. Despite generally lower efficiencies than grided ion engines[8], Hall thrusters are well suited for satellite station keeping and orbit adjustments. Examples of recent applications include the Busek Company's BHT-200 thruster aboard the AFRL TacSat 2, launched in 2006[7]. This form of thruster will be the focus of this report.

An important component of both grided ion thrusters and Hall type thrusters is the cathode neutralizer. Cathodes provide electrons to both initiate ionization within the propellant gas and to neutralize the emitted ion beam. Without neutralization, emission of an ion beam would quickly charge the spacecraft to a degree where no net thrust is produced. A common form of cathode is the hollow cathode type. Hollow cathodes generate a plasma which couples to the thruster plume through which a net electron current may flow.

1.2 Research Overview

The goal of this project was to explore a new form of electrostatic thruster, the Diverging Cusped Field thruster (DCF). The thruster concept employs an amalgamation of existing technologies and new ideas in an effort to create an efficient, long life electrostatic thruster.

While primarily an experimental proof of concept study, some insight into the operating principles will be offered.

In an attempt to gain insight into the complete electrostatic propulsive unit, this report also details the design and characterization of a small Lanthanum Hexaboride (LaB_6) hollow cathode. The goal of this portion of the project was to develop a hollow cathode which could meet the needs of the MIT Space Propulsion Laboratory for testing various low power thrusters.

Although ultimately designed to operate in tandem, the DCF thruster and LaB_6 cathode will be reported in a decoupled sense. Hence, chapters 2 to 5 are focused exclusively to the DCF thruster while chapters 6 and 7 describe the LaB_6 hollow cathode.

Chapter 2

The MIT Diverging Cusped Field
Thruster Overview

2.1 Review of Traditional Hall Thrusters
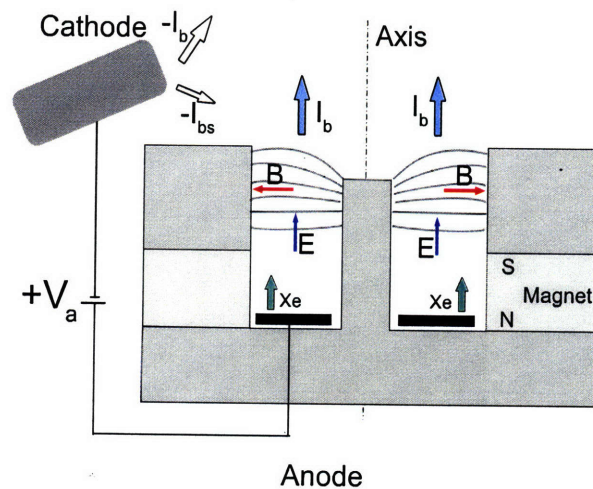
Figure 2-1: Schematic diagram of the DCF basic operating principles.

Traditional Hall thrusters employ a mostly radial magnetic field across an annular channel as shown in Figure 2-1. For detailed descriptions of Hall thruster physics consult the references[11, 12, 8]; however a brief overview of the basic Hall thruster operating principles will be presented in order to discuss the similarities, and differences between Hall thrusters

and the DCF thruster.

In a Hall thruster a high potential is applied between the anode and a single, externally mounted, cathode. Electrons, emitted from the cathode are accelerated by near axial electric fields towards the anode. When passing through the magnetic field they begin to drift in a direction perpendicular to the magnetic and electric fields, called $\vec{E} \times \vec{B}$ drift. The Hall thruster rotational symmetry implies that electrons may drift along closed azimuthal paths. The resulting net drift current is referred to as a Hall current, equation 2.1.

$$\vec{j}_{hall} = en_e \frac{\vec{E} \times \vec{B}}{B^2} \tag{2.1}$$

Neutral particles are injected into the channel near the anode to be ionized though electron-ion collisions as they flow axially downstream. The ions, whose Larmor radii generally exceed the thruster dimensions, are insensitive to the magnetic field and are accelerated axially by the electric field[11]. The electrons, moving at the $\vec{E} \times \vec{B}$ drift velocity do not feel the electric field in their frame of reference. Ion acceleration occurs through a quasi-neutral plasma. Finally, the ions are combined with an equal current of neutralizing electrons from the external cathode after being expelled from the discharge chamber. A high energy quasi-neutral plasma beam results. Thrust is conveyed to the thruster body via the Lorentz force between the magnets and the current loop created by the confined electrons. This arrangement has advantages over gridded ion thrusters in that is does not suffer from the space-charge limited emission problems of those designs[11, 13]. There are of course, many details involved in Hall thruster operation. An important aspect is the axial transport of electrons through the discharge channel. The mechanisms for electron transport can be largely explained through collisions with heavy atoms both within the discharge chamber, and along the thruster walls[11]. In addition, a departure from classical magnetic diffusion due to turbulent phenomena, sometimes referred to as anomalous or Bohm diffusion, is reported to have a significant effect on the electron transport towards the anode[14].

One draw back of the traditional Hall thruster is that the magnetic field lines intercept the channel walls. High electron mobility towards the walls can thus be expected as electron guiding centers tend to follow magnetic field lines. The flux of electrons induces ion attracting sheaths which generate losses both through ion recombination at the walls, and by altering the potential profile within the channel[11]. This last effect can alter the

potential to such a degree that ion acceleration deviates far from the desired axial path. Ions can then be accelerated into the walls or leave the discharge chamber along highly divergent paths[11].When high energy ions impinge on the thruster surfaces the walls may begin to erode. This is a major issue within Hall thruster development[15] as it ultimately limits the thruster lifetime[16].

2.1.1 Performance Metrics

This section introduces some of the observed quantities and performance metrics typically employed when characterizing Hall thrusters. Refer to Fig. 2-1 for some typical quantities of interest for a Hall thruster. The anode current I_a includes both the beam current I_b and the back streaming current I_{bs}. The back streaming electrons are also referred to as primary electrons as they can dominate ionization of neutral particles. The anode thrust efficiency, η_t given by equation 2.2, relates the beam power to the anode input power ($P_a = V_a I_a$). The average specific impulse, described in chapter 1, is calculated using the thrust and anode flow rate as in equation 2.3.In the equations below, T is the thrust produced and $\dot{m}_a$ is the flow rate through the anode region.

$$\eta_t = \frac{T^2}{2\dot{m}_a P_a} \tag{2.2}$$

$$I_{sp} = \frac{T}{\dot{m}_a g} \tag{2.3}$$

It can be shown[11] that the anode thrust efficiency can be subdivided into a product of efficiencies as in equation 2.4.

$$\eta_t = \eta_b \eta_u \eta_E \eta_c cos^2(\phi_b) \tag{2.4}$$

The beam efficiency η_b, is the ratio of beam current (I_b) to anode current (I_a) and is a measure of the flux of primary ionization electrons which flow from the cathode into the thruster channel. The utilization efficiency η_u, is the ratio of beam current to maximum current obtainable from the flow rate, assuming singly ionized ions. For singly charged ions, the maximum current is hence $I_n = \dot{m}_a e/m$ where m is the mass of a Xenon atom ($m \approx 2.18 \times 10^{-25} kg$). The divergence coefficient, $cos^2(\phi_b)$ is a measure of the beam divergence, taking into account that only axially directed ions provide thrust in an axisymetric, uniformly distributed plume. Ideally all ions would be accelerated equally through a po-

25

tential close to the anode potential. The non-uniformity factor, η_E accounts for the spread in ion energies. Finally, the charge efficiency η_c accounts for multiply charged ions. The functional forms of these factors are described in more detail in section 4.1 but have been introduced here to gain insight into the benefits of enhancing the various parameters within Hall thrusters.

When considering the overall thruster and cathode as a unit, both the efficiency and specific impulse are modified due to the power and flow consumed by the cathode. If P_c is the cathode power (generally to the keeper) and $\dot{m}_c$ is the cathode flow rate, the overall propulsive efficiency, η_o is given by equation 2.5.

$$\eta_o = \frac{T^2}{2\left(\dot{m}_a + \dot{m}_c\right)\left(P_a + P_c\right)} \qquad (2.5)$$

Similarly, the specific impulse in equation 2.6 is modified to include the cathode flow rate.

$$I^*_{sp} = \frac{T}{\left(\dot{m}_a + \dot{m}_c\right)g} \qquad (2.6)$$

As the particular cathode properties are not related to the thruster, only the anode efficiency (cathode power/flow are omitted) will be considered when discussing the DCF performance in the following chapters.

Some representative values of thrust, specific impulse and anode efficiency for commercial Hall thrusters, manufactured by the Busek Company[7], are presented in table 2.1 to provide context for the values to be reported in the following sections. Notice that anode efficiency tends to increase with power. The increase in efficiency at high power is typical. At low powers energy losses to the thruster walls become increasingly important as the volume to surface area decreases. In addition, low power thrusters require strong magnetic fields which may not be efficiently achievable using typical designs[12].

Thruster	Power, P_a	Thrust, T	Specific Impulse, I_{sp}	Anode Efficiency, η_t
BHT-200	200W	12.8mN	1390s	43.5%
BHT-600	600W	39.1mN	1530s	49.0%
BHT-1000	1000W	58.5mN	1750s	50.3%
BHT-1500	1500W	102mN	1820s	54.6%

Table 2.1: Summary of the nominal operating conditions for low to mid power Hall thrusters manufactured by Busek[7].

2.2 Diverging Cusped Field Thruster Concept

The DCF is schematically illustrated in Fig. 2-2. Three permanent magnets with alternating polarities are arranged in a divergent pattern resulting in two strong cusps within the channel and a significant axial magnetic gradient in approach to the anode. The magnetic field strengths within the channel are greatest near the base of the thruster, with decreasing field strengths downstream. The arrangement is intended to magnetically confine electrons streaming from an external cathode. Similar to traditional Hall thrusters a potential difference forms between the anode and the cathode located at the end of the channel. A potential gradient results and ions are accelerated in a quasi-neutral plasma, as in a Hall thruster. This section begins with a description of the DCF concept and its relations with traditional Hall thrusters. Later, the similarities between the DCF and other thrusters with cusped magnetic fields will be discussed. For details of the thruster design, including magnetic field simulations refer to the following sections in this chapter. The DCF thruster
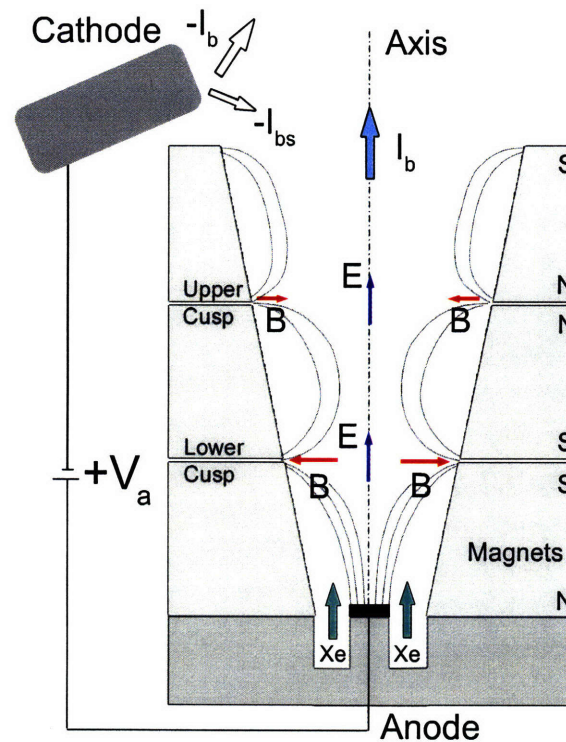
Figure 2-2: Schematic diagram of the DCF basic operating principles.

features strong magnetic cusps where radial magnetic fields are present in addition to a

presumably axial electric field between the anode and external cathode, as shown in Figure 2-2. The DCF is, in this respect, related to traditional Hall thrusters and azimuthal Hall currents are anticipated in these regions. However, the magnetic topology obtained using cusped magnetic fields provides several additional mechanisms which contribute to the thruster operation. Mechanisms which are quite distinct from traditional Hall thrusters.

When faced with a magnetic gradient, electron guiding centers feel a repulsive force in opposition to the gradient. The force, given by equation 2.7 is directly proportional the to magnetic gradient tangential to the field line.

$$F_{\parallel} = -\frac{m_e v_{\perp}^2}{2B} \nabla_{\parallel} B \tag{2.7}$$

Here $v_{\perp}^2$ is the electron velocity perpendicular to the field. This includes both the cyclotron motion of the electron about its guiding center and the perpendicular motion of the guiding center itself. It can be shown that the proportionality factor on the right hand side of equation 2.7 (the magnetic moment μ) is conserved along field lines[17]. Since total electron energy must also be conserved, the invariance of μ provides a mechanism for magnetic confinement of electrons when the electron energy parallel to a field line goes to zero. The concept is summarized by equating the magnetic moment at two locations along a field line, as equation in 2.8.

$$\frac{v_{\perp 2}^2}{v_{\perp 1}^2} = \frac{B_2}{B_1} = \frac{2E_K/m_e - v_{\parallel 2}^2}{v_{\perp 1}^2} \tag{2.8}$$

Here an electron, with total kinetic energy E_K is presumed to move through a magnetic gradient from a region of a given field strength B_1 to a region of higher field strength, B_2. The perpendicular energy hence increases at the expense of decreasing parallel energy until $1/2 m_e v_{\perp}^2 = E_K$. When fields are arranged to include multiple magnetic cusps a so called magnetic mirror arises where some electrons may be contained between the cusps by multiple reflections at each apex. The ratio of magnetic fields from the point of interest to the maximum field strength along a field line is sometimes referred to as the mirror ratio[18]. This configuration is also referred to as a magnetic bottle.

In the DCF, strong gradients, or magnetic bottles, are present both near the anode and at the magnet cusps. The result is a means for confining electrons both between the anode and first upstream cusp and between the first and second cusps within the channel. This arrangement provides additional electron confinement in tandem with the aforementioned

azimuthal drift currents at the radial field regions. This is in contrast to traditional Hall thrusters where primarily the closed Hall drift currents counter reactive electrostatic forces on electrons by moving them at a velocity where there is no electric field in the electrons reference frame. In addition, the magnetic gradients at the anode serve to inhibit electron flow directly from the external cathode down the center of the discharge channel by creating an axial magnetic trap. Without this feature, electron flow along the thruster axis, where the magnetic field is relatively low, would not be greatly inhibited compared with the regions closer to the channel walls.

Furthermore, the DCF arrangement is designed to reduce wall erosion and ion losses by containing the plasma away from the channel walls. Away from the cusps this is accomplished by magnetic lines which are mostly parallel to the wall. Electron transport across magnetic field lines is significantly reduced compared to mobility along the field lines[11]. This concept has been employed in ion engines for many years[13]. Therefore in the DCF, when combined with the magnetic gradients at the cusps, mechanisms to reduce electron flux to the walls are present throughout the discharge channel. By reducing electron flux, the sheath potentials required to maintain neutrality at the channel walls are also reduced. As a result a potential profile which avoids accelerating ions towards the walls could be achieved, in contrast to traditional Hall thrusters. Material surface sputter rates will decrease as both the ion flux and incident energy are reduced. Therefore the arrangement provides a means for reducing wall erosion within the channel. It should be clarified that in this description the ions are not assumed to be magnetized. Rather the potential profile, which is strongly influenced by the magnetically confined electrons affects the ion paths. In addition, such confinement represents an efficiency enhancement, avoiding energy lost when ions and electrons recombine/impact the walls. In summary, the DCF concept may both reduce energy losses to the thruster walls and increase thruster lifetime through reduced wall erosion.

Finally, the DCF features a divergent shape intended to further enhance performance. Most simply the divergent shape reduces losses of ions by increasing the range of trajectories that do not intercept the walls. However; the shape was motivated by several more subtle factors. As described above, the additional magnet creates a complete mirror between the two mid channel cusps. By further confining electrons in this region a secondary ionization region between the cusps could result. The third magnet continues to provide fields parallel

29

to the walls while the field strength gradually decreases due to the divergent shape. This feature was motivated through observations that similar cusped field thrusters tend to have a highly divergent dischare[19]. It was postulated that given the high field strengths expected within the thruster ions may become weakly magnetized as they pass through the discharge channel. Therefore the divergent shape was intended to gradually reduce the magnetic field strength exposed to axially accelerated ions as they progress from the first cusp towards the exit plane. A gradual reduction was selected to minimize the deflection of ions at the exit plane where the magnetic field curves sharply. Details of the magnetic circuit design and the expected magnetic field are provided in section 2.3

There are a few potential drawbacks of the DCF concept. First, the divergent channel will result in decreased neutral density along the channel. Therefore, if ionization is not completed in the low diameter upstream region, efficient ionization of the propellant may be difficult. On the same note, it is possible that if the magnetic confinement is too great and the plasma is confined a significant distance away from the channel walls, neutrals could stream between the walls and plasma without being ionized. Secondly, the localized electron confinement between the anode and first cusp, and at the second cusp could result in two stage behavior. The result would be a bi-modal distribution in ion energies, which by equation 2.4 is undesirable.

In summary, when compared to traditional Hall thrusters the DCF thruster concept enhances electron confinement beyond the $\vec{E} \times \vec{B}$ closed drifts through magnetic mirroring. Also, the DCF thruster is designed to reduce wall losses through constant magnetic protection of the thruster walls, either through parallel fields or strong magnetic mirrors near the cusps and anode.

2.2.1 Motivation and Comparison with Other Cusped Field Thrusters

The DCF design was primarily based on the experience gained from previous thrusters which employ cusped magnetic fields. The basic magnetic circuit stems from the highly successful, although not well understood, THALES High Efficiency Multi-stage Plasma(HEMP) thrusters[18, 20, 19]. In addition, the DCF also amalgamates features of the Princeton Cylindrical Hall Thruster (CHT) [21]. This section first describes the proposed operating principles of these thrusters than reviews similarities and unique aspects of the DCF thruster concept.

THALES High Efficiency Multistage Plasma Thrusters (HEMP)

The HEMP thrusters have been derived from Traveling Wave Tube (TWT) technolo-
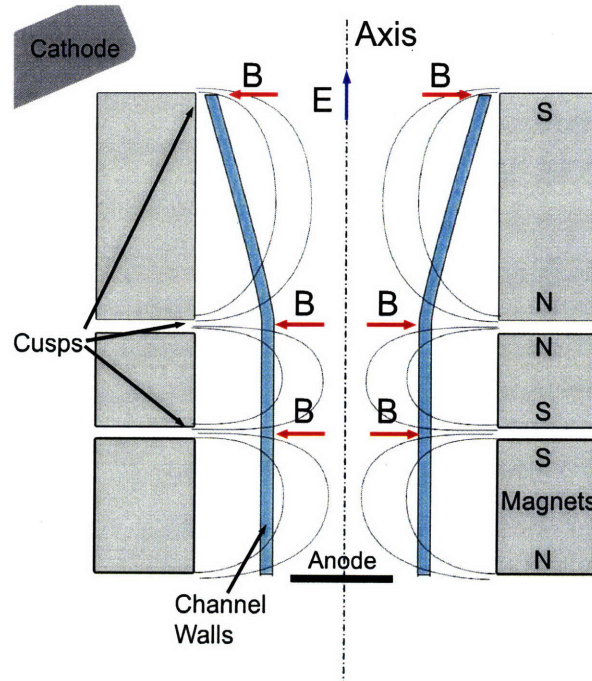
Figure 2-3: Sketch of the hollow HEMP type thruster layout reproduced from a number of sources[1, 2, 3]. Note that it is unclear in the references if the permanent magnets themselves have some variation in inner diameter along the channel.

gies used to amplify RF signals in communication satellite applications. Several iterations of the HEMP concept exist[2]. The DCF most resembles the HEMP-T 3050 class of thrusters which, according to recently presented results[1], have a nominal anode efficiency of $\eta_t = 46\%$, producing $50mN$ of thrust with an input power of $1500W$. HEMP thrusters use three permanent magnets arranged as in Figure 2-3. The periodic permanent magnet arrangement used in the DCF was inspired by the HEMP thrusters. The concept of using cusped fields to provide both radial field regions, to initiate Hall currents, and wall protection through near parallel fields away from the cusps was also initiated with the HEMP design[3, 22]The DCF adds to this an important feature, namely a central magnetic pole providing a magnetic mirror at the anode approach. Variation in the channel geometry and the exposed magnetic field strength appears to be obtained by some combination of varying the material thickness between the discharge chamber and the permanent magnets[1] and

31

varying the magnets themselves. However; the exact magnetic configuration is unknown. HEMP thrusters are designed to have a very strong magnetic cusp near the exit plane and two weaker cusps within the discharge channel[18]. The arrangement is claimed to isolate the thruster ionization region to the channel section upstream of the exit plane cusp[18]. Within this region, the combination of magnetic mirrors and field lines parallel to the wall are intended to dramatically reduce electron losses to the walls[19] yielding very high beam efficiencies (back streaming currents of a few percent of the anode current)[18]. The anode is not protected explicitly by the magnetic field lines, rather it is possible that the magnetic mirror between the two mid channel cusps inhibits electron flow to the anode. The apparent beam divergence of the plume emitted from HEMP thrusters varies between reports[23][18]. Visually a divergent cone can be seen, with some reports indicating that the discharge forms a hollow cone of high energy ions[18]. In the cited reference, cone divergence angles around 35% are reported. However; recent experimental data suggests a more diffuse high energy beam profile centered about the thruster axis has been achieved in the latest iteration of the design[23].

Princeton Cylindrical Hall Thruster (CHT)

The Princeton Cylindrical Hall Thrusters[21, 15, 24] employ both an annular region of highly radial magnetic flux lines and a cylindrical region which features a strong magnetic bottle and cusp towards the exit plane. In all reported iterations of the thruster to date, the magnetic field levels are below $1700G$, about 1/3 of the maximum field strengths in the DCF (see section 2.3). Hence the confinement region in the CHT is likely to be more diffuse than in the DCF. Sketches of the CHT thruster and magnetic field topology are shown in Figure 2-4. Here the magnetic fields are produced by electromagnets (allowing for optimization of the field[25]), and a ring shaped anode is located at the base of the coaxial region, unlike the central location chosen for the DCF. The CHT thruster has been designed to promote ionization in the coaxial region with ion acceleration confined to the cylindrical portion of the thruster. This isolation is stated to occur by designing the coaxial region to be approximately equal to the neutral mean free path for ionizing collisions [15]. The ion acceleration is then presumed to take place in the cylindrical region of the thruster. A localization of potential gradients in the cylindrical region has been confirmed experimentally using internal probe measurements[26].
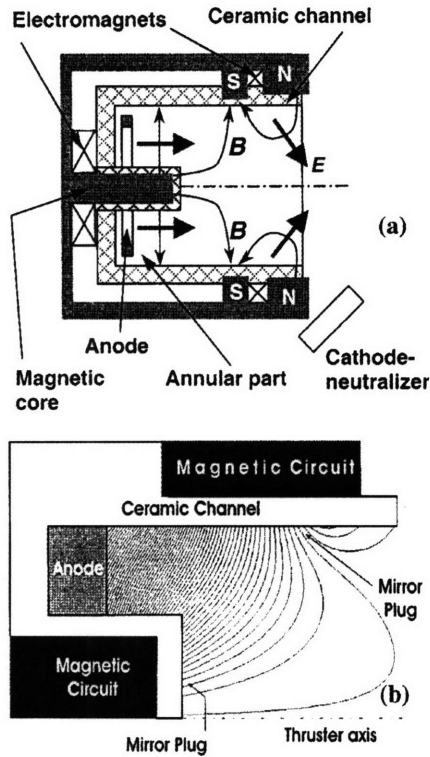
Figure 2-4: Schematic of the Princeton CHT thruster and a typical magnetic field profile (image source [4]).

The cusped structure and magnetic mirror in the cylindrical region are intended to trap electrons, and hence neutralize space charge, both through the typical Hall current traps and by the magnetic gradient forces[15]. This application of magnetic mirrors specifically to confine electrons in the expected acceleration regions distinguishes the CHT from traditional Hall thrusters. Unlike the HEMP thrusters described above, where magnetic cusps are found only along the thruster wall, the CHT central cusp produces an axial force on the electrons. Therefore, as in the DCF, the CHT magnetic field may counter the reactive force on electrons due to both the closed Hall currents and the axial magnetic gradient forces. In addition, the cylindrical region is intended to reduce ion losses by enhancing the volume to surface area ratio in the acceleration region[21].

The CHT thruster has been largely optimized for small low power applications where the large volume to surface area ratio and strong magnetic fields are highly desirable[15]. Specifically, the $3cm$ diameter iteration of the CHT operates consistently with anode efficiencies above 20% at anode powers as low as $100W$ while promising longer lifetime than

traditional Hall thrusters through reduced channel wall erosion[27]. The beam divergence of CHT thrusters can reach 80° in some circumstances, although the most recent optimizations of the field profile have reduced this angle significantly[15].

MIT Diverging Cusped Field Thruster (DCF)

Although the periodic permanent magnetic arrangement of the DCF thruster bears a strong similarity to the HEMP thrusters, the DCF also resembles the CHT thruster with the coaxial region removed. CHT type thrusters with no coaxial region have been developed[28], however; even in this circular cross section case, the anode is place in a region of predominantly radial magnetic field lines which intercept the thruster walls.

The anode position is one of the key distinguishing features of the DCF thruster compared to both the HEMP and CHT designs. In the DCF the anode is intentionally placed at the apex of the magnetic bottle to reduce electron flow and facilitates strong variations of this flow via the ability to make small adjustments of the anode's axial location. In the HEMP thrusters the electron flow is presumably inhibited by means of mirroring between the first and second magnetic cusps closest to the anode. The anode itself does not appear to be directly protected by a magnetic bottle. As described above the, in the CHT a ring shaped anode is placed in a region of predominantly radial fields very similar to traditional Hall thrusters.

Both the THALES and Princeton designs claim to separate ionization and acceleration regions within the discharge channel. However, in a 1D arrangement, it is known that the potential drop and hence ion acceleration starts in the ionization layer and becomes steep just beyond it[29]. In analogy to the Chapman-Jouguet detonation condition, the sonic condition ($v_i = (kT_e/m_i)^{1/2}$) occurs precisely at the exit from this ionization layer, the flow being supersonic downstream. In the DCF, the ionization region is likely to have a more complex 3D topology, defined by the dominant magnetic bottle; however the same physics should prevail and we expect strong ion acceleration at just the exit of this ionization region. This would seem to negate the possibility of a clean separation between ionization and acceleration regions, as suggested in both the HEMP and CHT thrusters. As a result, in the DCF we anticipate both ionization and acceleration of ions to be strongly localized in combined magnetic bottle and azimuthal drift current traps.

Specifically, the HEMP design employs a magnetic field which protects the walls both

through parallel fields and the magnetic cusps. However, this protection has been specifically optimized[18] to contain electrons within a presumed ionization region upstream of the exit plane. Again, this differs from the DCF where separation of ionization and acceleration regions was not assumed and acceleration is presumed to begin in the region between the anode magnetic bottle and first cusp.

Recent iterations of the THALES HEMP thrusters also feature a divergent pattern[1]. However; the detailed design is not divulged and the divergence may occur only between the second and third cusps and may be created via the channel wall shape only, not through use of continuously divergent magnets as in the DCF.

The DCF is thus a combination of both the CHT and HEMP concepts designed to employ favorable qualities of both, in addition to new features aimed at improving the overall thruster performance, in order to produce an efficient long-life thruster. It is important to recognize that while the two references cited here bear the greatest resemblance to the DCF thruster, and have been the primary motivation of the design, there have been several previous thrusters employing magnetic mirrors or cusp fields. For example the Kaufman End-Hall ion source[30], relies primarily on axial forces from magnetic gradients to prevent electron motion towards an anode positioned at the base of the mirror. The anode location of the DCF is thus similar to this design.

2.3 DCF Magnetic Circuit Design

This section reviews the magnetic circuit designed to meet the conceptual requirements of the DCF thruster which were outlined in the previous section.

2.3.1 Basic Design and Approach

The DCF magnetic field topology was developed using Ansoft Maxwell SV[31] software to simulate the fields produced by various magnetic configurations. Numerous simulations were performed in an effort to produce a magnetic circuit which captured all the of the conceptual benefits of the DCF concept which were outlined in section 2.2. These include (i)strong magnetic mirrors, (ii)protection of the thruster walls and (iii) a gradually decreasing magnetic field within a divergent channel. It is important to stress that the exploratory nature of this prototype design did not allow for highly quantitative development of the field, rather a more intuitive approach was taken at this time. Figure 2-5 shows the basic
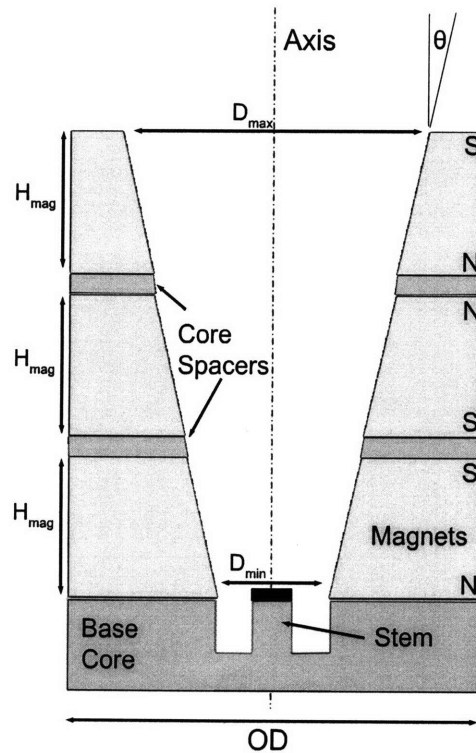
Figure 2-5: Basic magnetic circuit and design variables considered in developing the final DCF magnetic circuit.

magnetic circuit and geometrical factors which were varied in developing the design. The three permanent magnets are complemented by soft steel (1018 grade *Carbon Steel*) spacers and a large core at the base of the structure. The spacers help focus and modify the cusp field geometry. The base core was designed to channel magnetic flux into the core stem shown in the figure. The basic scaling dimensions of the thruster are on the same order as Hall thrusters with similar expected power consumption and operating performance. For example the Busek[7] BHT-200 Hall thruster[16] which has an annular channel roughly 20mm in length with ID 20mm, OD 30mm. In the DCF, the magnet diameter at the base of the discharge channel, D_{min} was fixed at 20mm. The channel length from the anode to the first cusp was set by the first magnet thickness, H_{mag} to be 12.5mm. For simplicity the magnet thicknesses and outer diameters were held constant. The outer diameter of all magnets, OD in the figure is 64mm. Given that the quantitative effects of the divergent shape were not known during the design phase, the wall angle, θ, was set to 22.5°. This angle was selected for the prototype design to provide significant reductions in the field strength along the channel while maintaining a relatively small area, and hence high neutral density, near the thruster base where the majority of ionization is expected to occur. The size of the magnets thus decreases moving axially from the anode, resulting in reduced field strengths in the channel, as desired.

Further design variations focused on the core structures, both at the base and the spacers between the magnets. Magnetic flux was focused through the thruster axis by incorporating an annular channel in the base core structure, resulting in the core stem indicated in the figure. The annulus thickness and depth were varied in order to maximize flux through the stem while avoiding saturation of the steel and maintaining mostly parallel field lines along the magnet walls. The core spacer thicknesses were adjusted to ensure regions of mostly radial field which were several mm in thickness (comparable to the confinement region of traditional Hall thrusters[12]), while also ensuring strong magnetic bottling at the cusps.

2.3.2 Magnetic Source Selection

In order to create the desired magnetic topology, permanent magnets were selected over electromagnets. This decision was made given the high field strengths desired, the required complexity of the field topology, and the electrical power savings inherent in using permanent magnets. For a basic review of permanent magnet properties and design criteria

the reader should consult one of the references[32, 33]. In this application we required a magnetic material which could maintain a strong field both at elevated temperatures and in the presence of other magnets with inverted polarities (at the cusps).

Rare earth Neodymium Iron Boron ($NdFeB$) and Samarium Cobalt ($SmCo$) magnets were considered given their high field strengths[32]. $SmCo$ was ultimately selected given its good thermal properties and resistance to demagnetization. Specifically, type 3212 $SmCo$ supplied by Dexter Magnetics[32] was used. The B versus H hysteresis curve supplied by the manufacturer is available in appendix C. The quoted residual induction of this material (in effect the expected surface field strength when isolated from demagnetizing forces) is $11.5kG$, or $1.15T$. Samarium Cobalt has a high intrinsic coercivity of $12kOe$ at $20°C$, meaning it maintains a high intrinsic field in the presence of demagnetizing fields. The listed maximum operating temperature is $300°C$, above which permanent reductions in the field can be expected. The specific impact on intrinsic coercivity due to elevated temperatures can be found in the appendix. The Curie temperature, where the material losses its ferromagnetic properties, is $825°C$. The thermal behavior is a concern given that typical SPT type Hall thrusters can have wall temperatures around $400°C$[16]. As a result some field degradation could occur; however, if the magnetic confinement desired in the DCF is effective, the wall temperature may be much lower.

Figure 2-6: One of the $SmCo$ magnets used in the DCF prototype, see appendix A for exact dimensions.

The decision to use the maximum available strength of $SmCo$ magnets can be justified

through considering the conceptual description in the previous section. In traditional Hall thrusters an excessive magnetic field can effectively choke electron flow to the anode, hence restricting operation of the thruster. However, in the DCF concept an excessively high magnetic field will simply serve to contain the plasma further from the chamber walls within the magnetic mirror where the field strength is lower. Since the field goes to zero between the cusps on the thruster axis it is presumable that the operation would be only weakly affected by the specific field strength at the chamber surfaces. Severe magnetic bottling at the anode, which could prevent electron flow as in traditional thrusters, can be overcome by varying the anode position within the field geometry. Such a feature has been employed in the prototype design and will be discussed shortly, in section 2.4.1.

2.3.3 Simulated DCF Magnetic Field

The simulated magnetic flux lines and magnetic field strengths of the DCF thruster, in a vacuum, are shown in Figures 2-7 and 2-8 respectively. The flux pattern shows that both regions of radial magnetic field and strong magnetic bottles were achieved at each cusp along the channel. In addition a strong bottle is achieved at the anode. The non magnetic components shown in Fig. 2-7 will be reviewed in the following sections. Referring to Fig. 2-8, the magnetic field strength in the channel ranges from zero, along the thruster axis at the cusp positions, to roughly $0.5T$ near the channel walls. This peak strength is approximately three times the maximum($\sim 1.7kG$) found within the Princeton CHT thrusters[15]. The magnetic field is seen to decrease moving axially along the discharge channel as desired. Given these fields, some quantification to the claims in section 2.2 that ions could be weakly magnetized can be made. The Larmor radius, given by equation 2.9, for a Xenon ion ($m_i = 2.18 \times 10^{-25}kg$), accelerated through a $300V$ potential (perpendicular to the field) in a $0.5T$ magnetic field is approximately $60mm$.

$$r_L = \frac{v_\perp}{\omega_c} \approx \frac{\sqrt{2eV_a/m_i}}{eB} \tag{2.9}$$

The Larmor radius is thus on the order of the thruster dimensions so some weak interactions could occur[17]. However; given that the maximum field has been used in this calculation, the effects on most ions may not be as significant as first expected.

Confirmation of the magnetic mirror structure desired between the first cusp and the
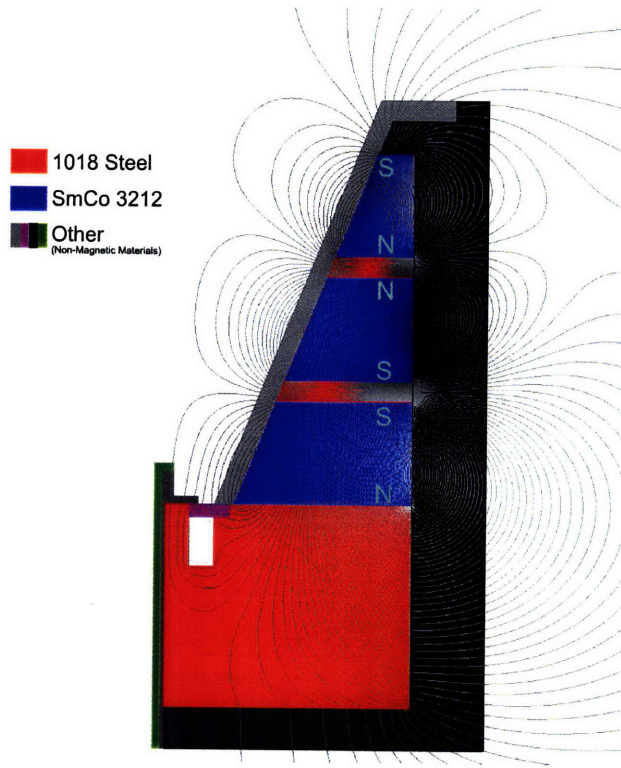
Figure 2-7: Magnetic field topology represented by magnetic flux lines within the DCF thruster, in vacuum.

anode is given by Figure 2-9. In the figure, the tangential magnetic field strength is shown following a field line which intercepts the anode. In this example, the tangential field gradients are approximately $30T/m$ and $60T/m$ in approach to the anode and cusp respectively. Along this field line the ratio of maximum to minimum field, the maximum mirror ratio, is approximately 3.8. Such ratios are difficult to compare given that the minimum field varies radially. However; ratios of similar magnitude are reported in the strongest cusp (at the exit plane) of the THALES HEMP thrusters[18]. Furthermore, both Figs. 2-8 and Figure 2-10 show that an axial magnetic trap has been achieved in approach to the anode. As described in section 2.2, this feature was desired in order to prevent electron flow from the cathode to the anode directly along the thruster axis.

2.3.4 Measured Magnetic Field Profile

Experimental confirmation of the magnetic field was carried out with an AlphaLab DC Magnetometer[34] accurate to within $\pm 2\%$. The probe dimensions were generally larger
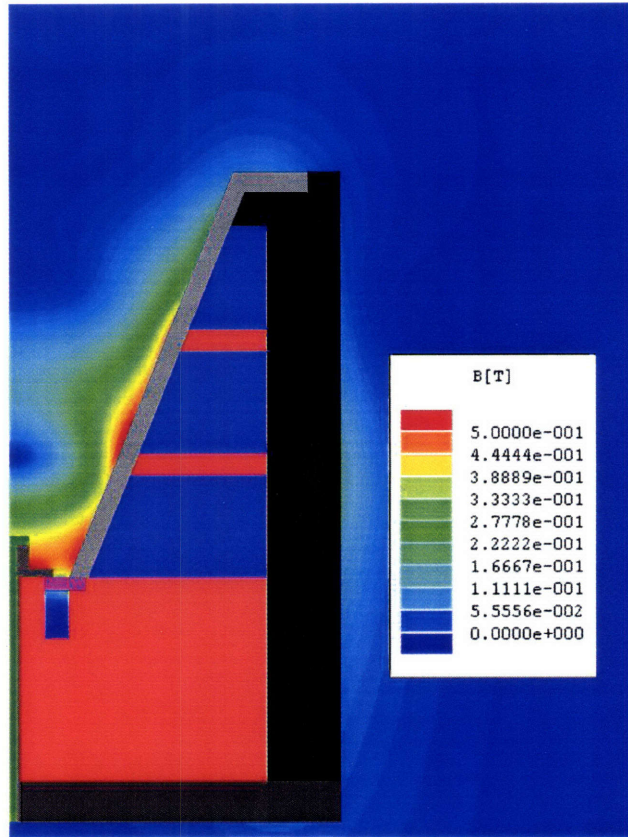
Figure 2-8: Simulated magnetic field strength within the DCF thruster, in vacuum.

than the length scales of variation within the thruster field, as a result only the field along
the thruster axis could be measured accurately. Comparisons between the measured and
predicted fields are shown in Fig. 2-10. Good agreement was achieved. Some uncertainty
in axial position existed due to the enclosed nature of the probe. The two experimental
curves were measured approximately one year apart, during which time all thruster data to
be presented in this report were collected. The results show that minimal degradation of
the field has occurred throughout the test campaign.
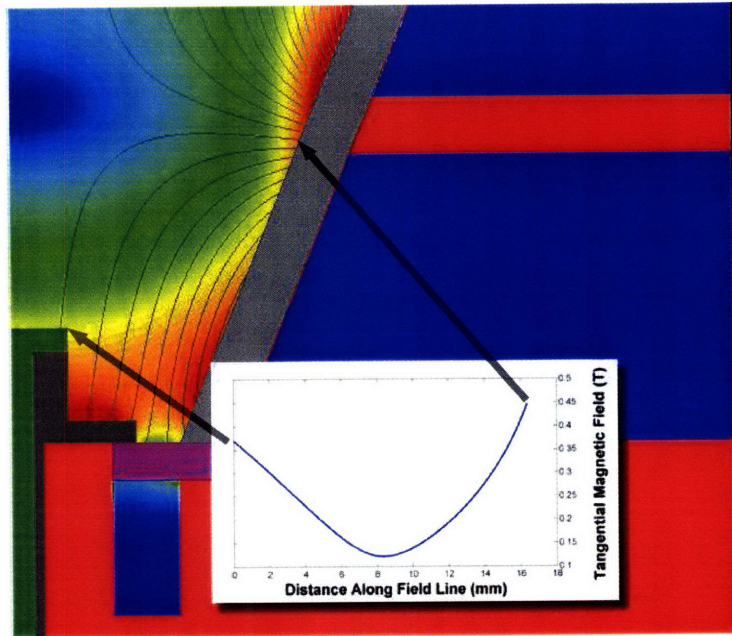
Figure 2-9: Magnetic bottling achieved along field lines with the DCF thruster.
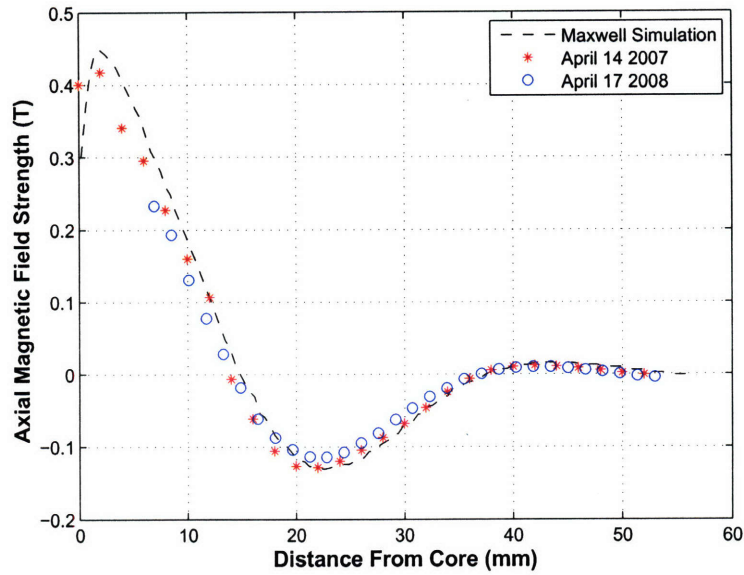
Figure 2-10: Measured and simulated axial magnetic field strengths along the DCF thruster axis. The figure also confirms the presence of a desired axial magnetic trap in approach to the anode.

42

2.4 DCF Thruster Design

1. Aluminum Cap
2. Anode
3. Anode Insulation
4. BN Disc
5. BN Insulator Cone
6. BN Riser
7. Fuel Line
8. Mounting Plate
9. Porous Diffuser Disc
10. Outer Casing
11. SmCo Magnets
12. 1018 Steel Core
13. 1018 Steel Spacers
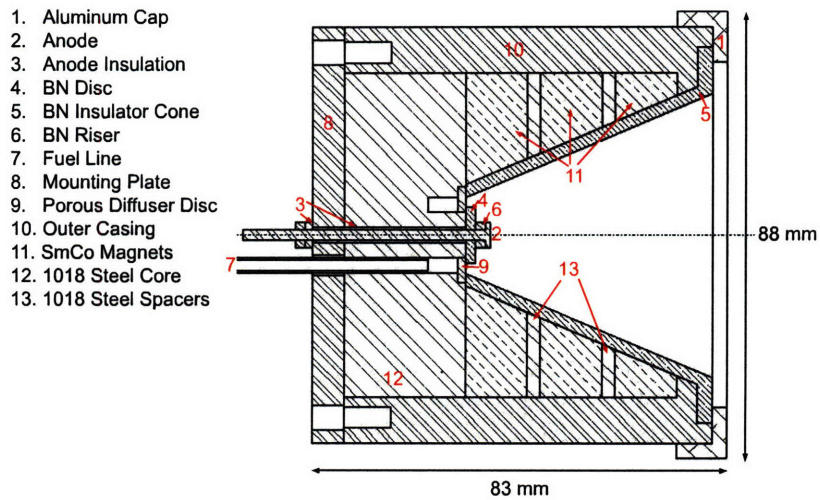
Figure 2-11: Cross-section view of the DCF components.

Details of the MIT DCF prototype design are presented in this section. Figure 2-11 shows the various components, to scale. All materials used throughout this section are non magnetic, and hence do not affect the field topology presented in the previous section. Unless otherwise stated, all components discussed in this section were manufactured on site by the author. The detailed drawings are provided in appendix A.

2.4.1 Anode Design and Position

Figure 2-12: Partially assembled stainless steel anode and ceramic spacers.

The propellant feed and anode are physically disconnected in the DCF design, see Figure 2-11. This allows for flexibility when optimizing performance by allowing the anode position to be varied independent of the propellant inlet. The original anode was made from a single

piece of type 316 stainless steel. The anode consisted of a long conducting rod, $2mm$ in diameter, terminated by a $5mm$ diameter tip, $1mm$ thick at one end. The last $14.5mm$ of the post are threaded so that the anode may be secured using a nut, see Figs. 2-13 and 2-12. In addition, a graphite anode, of identical dimensions, was used in the later stages of testing. Details of the graphite anode, and the reasons for abandoning the stainless steel anode are discussed in section 3.3.3. Only the anode tip is exposed to the channel. As
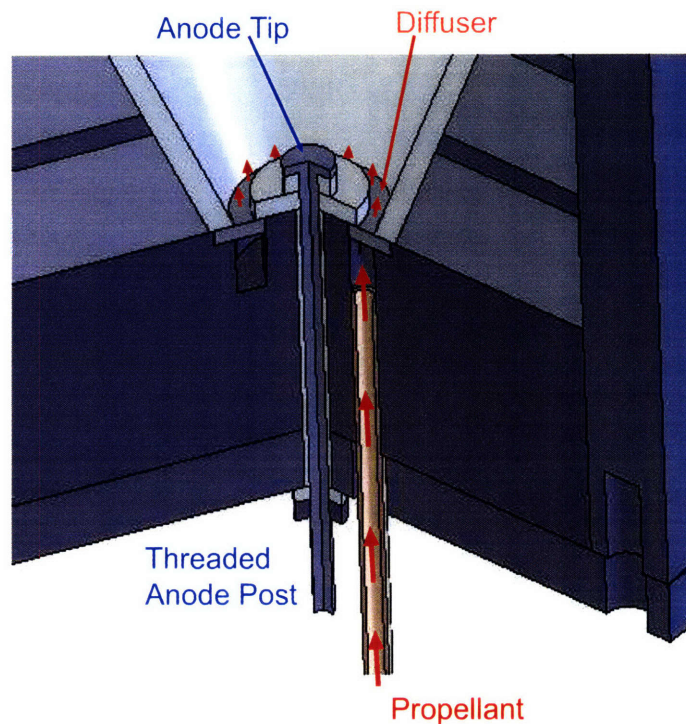
Figure 2-13: Scale cross section of the anode and fuel assemblies in the DCF thruster. Propellant is fed through the feed line into an annular channel before diffusing through a porous disc into the channel.

shown in Fig. 2-13, the anode post was electrically isolated from the main body by use of ceramic insulators (HP grade boron nitride[5]). Additional spacers are positioned below the anode tip between the core material and the anode surface. The anode can be repositioned by altering the thickness of the ceramic spacers. The magnetic field strength along the thruster axis in the anode region was depicted in figure 2-10. In the figure, the steel core is at $x = 0$. During all successful trials reported in this paper, the anode tip was placed $5mm$

from the core stem, where the field is roughly $0.35T$. The anode electrical connection was made at the rear of the thruster by attaching a wire to the exposed anode post.

The original stainless steel anode, ceramic sheath and spacers were manufactured by Eric Rose of Natick Massachusetts[35].

2.4.2   Propellant Inlet

Propellant is fed into the discharge channel through a ring of porous stainless steel inserted at the downstream edge of the annular channel in the base core material, see Fig. 2-13. The porous stainless steel is intended to effectively stagnate the flow in the annular channel before allowing propellant to diffuse uniformly through the disc and into the discharge channel. Ensuring this condition required selecting the diffuser material such that the pressure in the annular plenum would not approach the choking condition at the fuel line inlet to the plenum. However; given the high costs of custom made porous components that would have complemented a rigorous design, the first iteration used a $10\mu m$ pore size disc from Small Parts[36], at a low cost. No information regarding the permeability (or flow rate related to pressure) of these discs was available. Specifically, $1/16''$ thick discs of porous type 316 stainless steel were used. A $9mm$ diameter hole was made in the disc to create a porous diffuser ring which was then placed over the annulus.

The complete propellant feed assembly is summarized in Fig. 2-13. In this prototype design, flexibility was desirable at the expense of perfect seals in the feed system. As a result, the diffuser ring was simply set into an indentation in the base core material and held in place by oversized ceramic washers below the anode, as can be seen in the figure. This arrangement allowed for changes and modifications to the diffuser without major disassembly of the thruster. Propellant is supplied through a $1/8''OD$, $0.055''ID$ type 316 stainless steel tube from the rear of the thruster. In the prototype design, the tube and base core were threaded so that the tube could be easily removed. The thruster body was kept floating electrically by including an *Insulator Seal*[37] *Cryogenic Break*, model 9611003 between the external flow connection and the thruster. The break uses a section of ceramic to allow propellant flow but inhibit electrical current.

Figure 2-14: The HP grade boron nitride cone used to insulate and protect the DCF channel walls. The cone was manufactured by Saint-Gobain Ceramics[5].

2.4.3 Dielectric Channel Walls

The dielectric wall of the channel consists of single piece of HP grade boron nitride, turned into a flanged cone by Saint-Gobain Ceramics[5]. The radial thickness of the cone was $2.5mm$ throughout the length of the channel. Considering the $22.5°$ angle, the wall thickness was thus $2.7mm$. The channel diameter at the base of the thruster was thus $15mm$, expanding to $56mm$ at the exit plane. Boron nitride was selected because it can sustain high temperatures without becoming conductive and has good thermal conductivity to avoid thermal stress. In addition, it can be easily machined into complex shapes and is frequently used in SPT type Hall thrusters[16]. The existing heritage allows for more direct comparisons between the erosion characteristics of the DCF and those of traditional Hall thrusters. Due to the inability to accurately predict the temperature of the channel walls, the expected thermal expansions could not be calculated to a high degree of tolerance. Therefore stresses due to the relative thermal expansions of the dielectric and the magnets/outer casing were a concern. To counter this, the cone was held in place using an aluminum cap loosely fixed at the exit plane of the thruster, allowing for some axial expansion if needed.
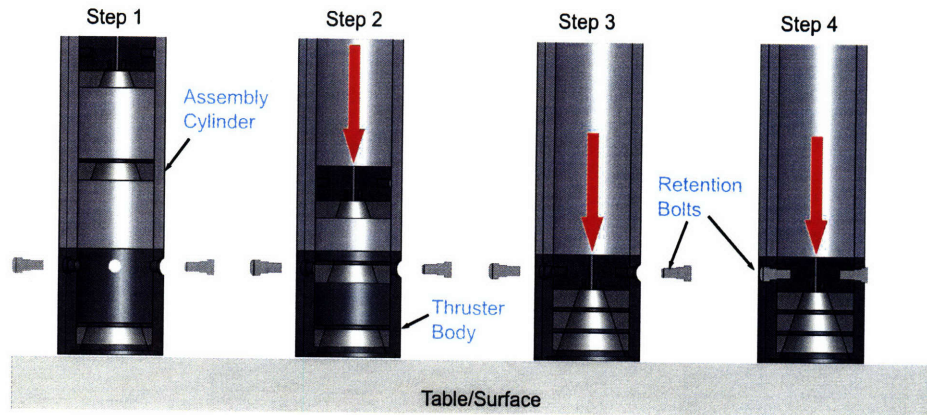
Figure 2-15: Assembly processes used to compact the DCF permanent magnets.

2.4.4 Casing and Assembly

A consequence of using permanent magnets in a cusped arrangement is the difficulty in assembling the thruster due to forces between the magnets. Specifically in their final arrangement, the repulsive force between the two largest magnets was approximately $350N$ (determined using the Maxwell SV Field Calculator[31]). A robust method of containing the magnets was therefore required. The final design, illustrated in Fig. 2-11, incorporates a type 316 stainless steel cylindrical casing with an upper flange, designed to match the channel angle when assembled. The base core piece was then modified to accommodate several large bolts inserted through the casing and into the core. With this arrangement the magnets and spacers could be pressed into position and locked in place using bolts through the steel casing and into the base core. The process is depicted in Figure 2-15. Figure 2-16(a) shows the assembled thruster, with the ceramic cone removed to allow views of the magnets. In addition, a cross section of the complete CAD assembly is shown in Figure 2-16(b). Finally, the completed thruster with hollow cathode neutralizer and ceramic wall insulation is shown in Figure 2-17.
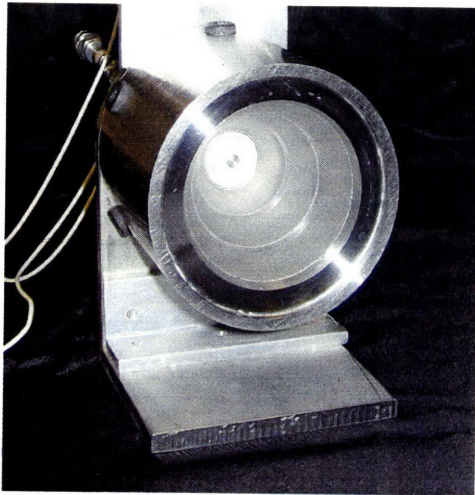
(a) Assembled DCF thruster with the channel insulation cone removed.
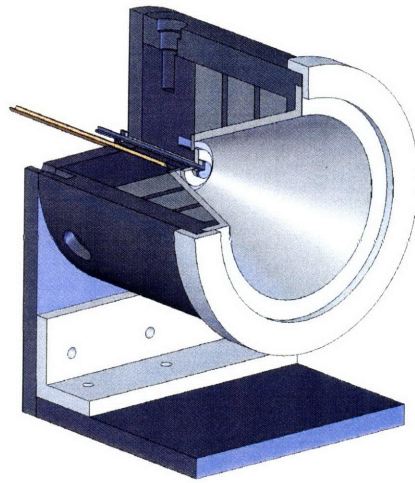
(b) CAD model of the complete DCF thruster assembly.

Figure 2-16: Completed DCF thruster.
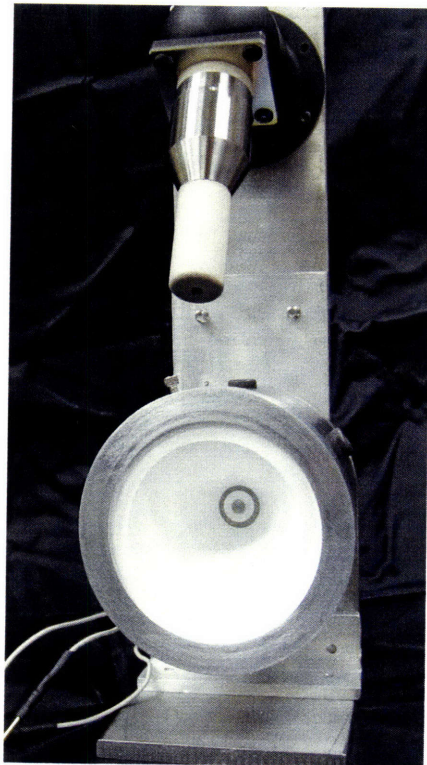
Figure 2-17: Assembled DCF and Busek hollow cathode prior to initial testing.

Chapter 3

DCF Preliminary Results and Performance

3.1 Experimental Setup and Facilities

The DCF has been tested at two facilities, the MIT Space Propulsion Laboratory (SPL) and the Busek Company in Natick, MA[7]. Voltage and current measurements along with visual observations were conducted at the MIT SPL. Further trials, including thrust measurements were performed at Busek. The basic configuration used for all tests is shown in Figure 3-1. The thruster body was left at floating potential by means of a dielectric slab placed under the thruster base and by a ceramic break inserted in the propellant line. The cathode emitter potential was fixed to the facility ground through the power supply ground connections. The anode, cathode keeper and cathode heater potentials were applied with respect to this reference ground. For all trials 99.999% purity xenon gas was used as the propellant. The flow rates will be given in standard cubic centimeters per minute, $sccm$. For Xe, $1sccm$ is equal to $0.09830mg/s$.

3.1.1 Hollow Cathode Neutralizer

During all tests the thruster was equipped with a Busek[7] built hollow cathode shown in Fig.2-17. The cathode is an impregnated tungsten (with barium oxide, $BaO - W$, forming impregnates) type hollow cathode, discussed in detail in chapter 6. In order to prevent damage to the cathode due to impurity contamination it was slowly heated over a roughly

49
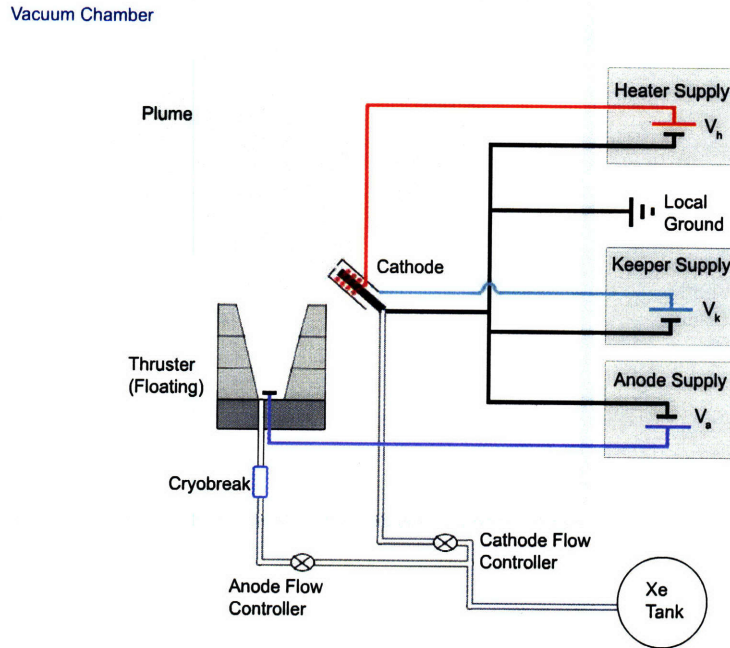
Figure 3-1: Sketch of the basic experimental configuration used both at SPL and Busek. The thruster body was kept floating by insulation between the base and vacuum chamber potential (local ground) and a cryobreak in the propellant line.

four hour period after each exposure to atmosphere. During the heating process the cathode heater current was increased by $0.5A$, beginning at $2.0A$, every half an hour until it reached $7.5A$. In nominal running conditions the cathode operates with $1sccm$ of Xe flow and $0.5A$ through roughly $20V$ to the keeper ($P_k \sim 10W$) and the heater circuit deactivated. In all DCF trials the cathode was current regulated to operate at $0.25A$ to the keeper while the required keeper potential was allowed to vary. The current was held lower than the nominal conditions to reduce the total power even with occasionally high keeper potentials. A simple cathode mounting system allowed for the position of the cathode to be varied easily. As will be discussed shortly, the cathode position had a significant impact on the thruster operating characteristics. Referring to Fig. 3-2, three cathode locations labeled A, B and C were used. Although the magnetic field strength at the cathode location is far less than that within the discharge channel, it is not insignificant (around $100G$ at position B) and may have a strong influence on cathode coupling to the plume. The specific locations of the cathode keeper orifice point, with reference to the edge of the ceramic retention cap in axial (z) and radial (r) coordinates are listed in table 3.1.

50
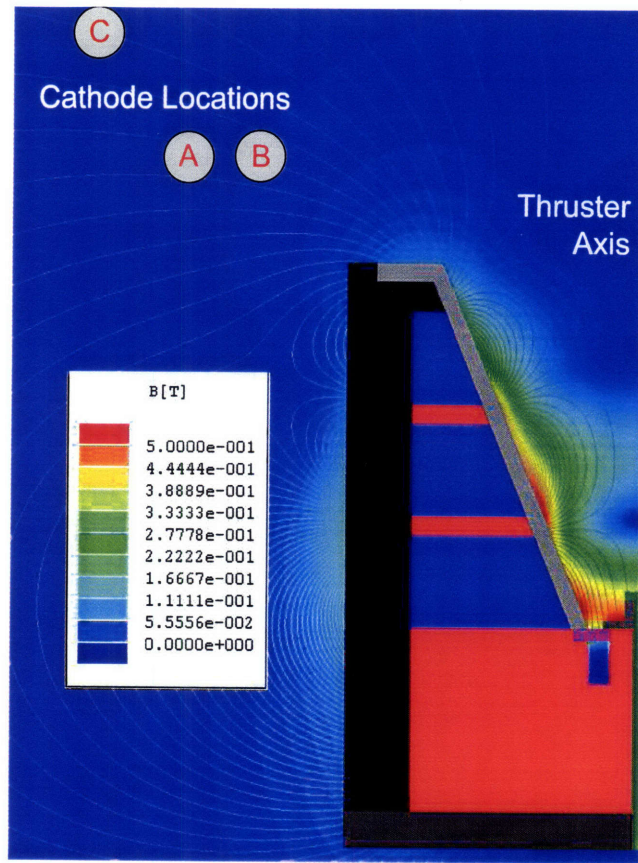
Figure 3-2: The DCF simulated magnetic field showing the approximate locations of the hollow cathode keeper orifice with reference to magnetic flux lines.

Position	Axial Distance, z(mm)	Radial Distance, r(mm)
A	11.5 ± 1	19.3 ± 1
B	11.5 ± 1	9.3 ± 1
C	27.5 ± 1	31.8 ± 1

Table 3.1: Locations of the Busek hollow cathode during trials.

3.1.2 MIT Space Propulsion Laboratory Facilities
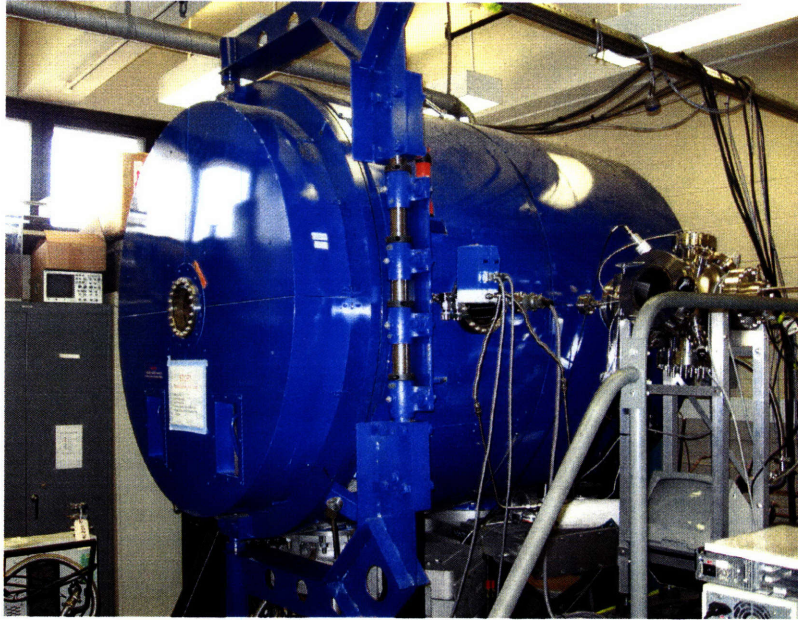
Figure 3-3: The MIT Space Propulsion ASTROVAC facility used in these experiments. The chamber is pumped by two cryopumps and one mechanical roughing pump.

The MIT SPL vacuum facility (ASTROVAC) consists of a 1.5m by 1.6m chamber equipped with a mechanical roughing pump and two cryopumps, shown in Figure 3-3. Specifically, a CTI-Cryogenics $CT10$ cryopump and a larger $OB400$ (also CTI) cryopump, together capable of pumping out roughly $7500L/s$ of Xenon were used. The pressure was monitored with a cold cathode gauge calibrated for Xenon. The pressure did not exceed $4.2 \times 10^{-5} Torr$ while operating at a maximum flow rate of $10.0sccm$. Two $1.0kW$ *Sorensen* DC power supplies were used to meet the anode and cathode power requirements. A $300V$ maximum model *DCS 300-3.5E* was used for the cathode keeper (V_k) while a $600V$ maximum model *DCS 600-1.7E* was used for the thruster anode (V_a). The cathode was heated using a $HPJA1460PS$ DC power supply. The cathode and anode flows were regulated using two *Omega FMA-A2400*[38] flow controllers calibrated for Xenon flow. The maximum flow from each regulator was $10sccm$ of Xenon. The DCF thruster mounted within ASTROVAC is shown in Figure 3-5(a).
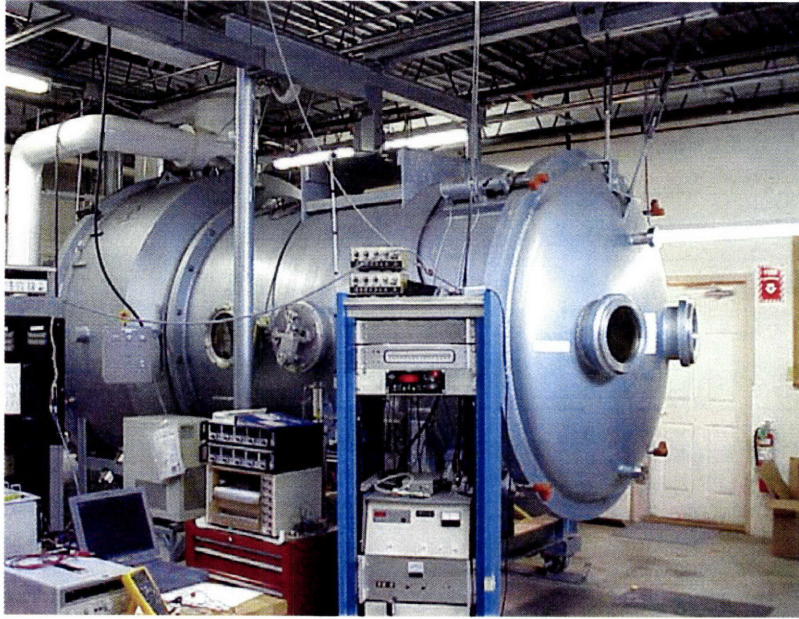
Figure 3-4: The Busek company tank T6 which was equipped with a thrust stand. The tank is pumped by a mechanical pump, a diffusion pump and a cryopump.

3.1.3 Busek Facilities

At Busek, the thruster was tested in tank T6 (measuring 6' in diameter), shown in Figure 3-4. This tank was equipped with a mechanical pump, a diffusion pump and a cyropump with a total pumping capacity of $90,000L/s$[12]. Pressure did not exceed $4.4 \times 10^{-6}Torr$ while again operating at a maximum flow rate of $10.0sccm$. Here a thrust balance, accurate to within $\pm 1.6mN$, was available. The recorded uncertainties, dominated by statistical fluctuations, are presented along with the measured quantities in the following section. The addition of thrust measurements allowed for basic performance evaluations to be made when combined with readings of anode current and potential. The DCF thruster is shown, mounted on the Busek thrust stand, in Figure 3-5(b).
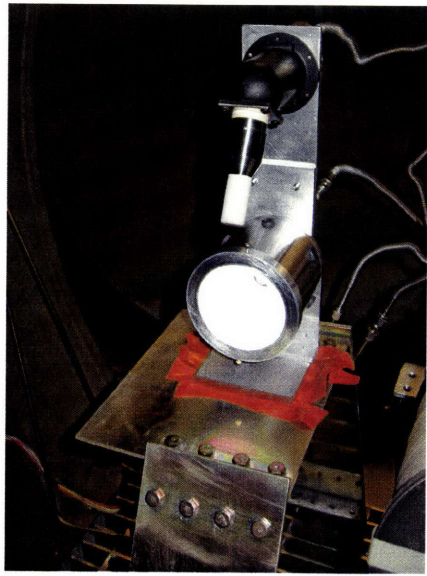
(a) DCF thruster prior to testing within the SPL ASTROVAC facility. The dielectric tape below the base served to keep the thruster floating with respect to the chamber.
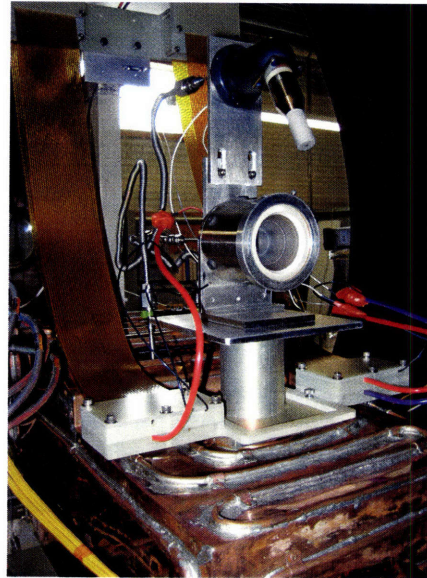
(b) DCF thruster mounted on the Busek thrust stand within Busek's tank T6.

Figure 3-5: Photographs of the thruster in firing configuration at both SPL(a) and Busek(b).

3.2 Experimental Characterization of the DCF Thruster

Numerous tests at both SPL and Busek have yielded preliminary performance data. These include several anode potential/current scans and thrust measurements.

3.2.1 First DCF Discharge

An initial attempt, with the cathode located in position A in Fig. 3-2 and with the anode tip positioned $3mm$ above the core stem, did not produce a discharge with anode potentials up to $600V$. The cathode was moved to position B and the anode was pushed forward to $5mm$ from the core stem. A discharge was produced with $250V$ to the anode at a flow rate of $8.5sccm$, see Figure 3-6. A voltage scan was then performed, the anode current measurements are presented in Figure 3-7. The discharge was highly unstable and anode current varied greatly between repeated observations at the same anode voltage, as seen in the figure.
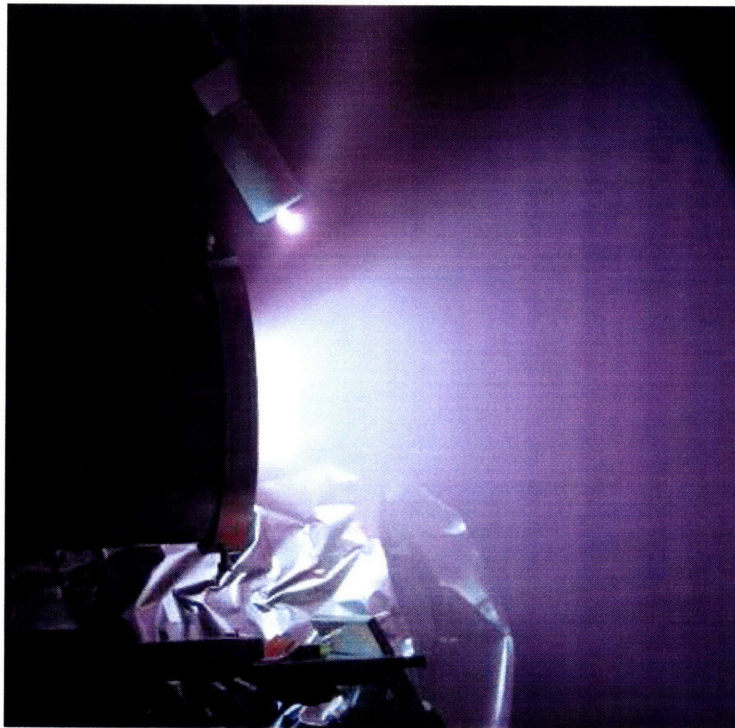
Figure 3-6: Visible discharge of the first successful DCHT test.

The cathode keeper potential was alarmingly high during the first successful test run,
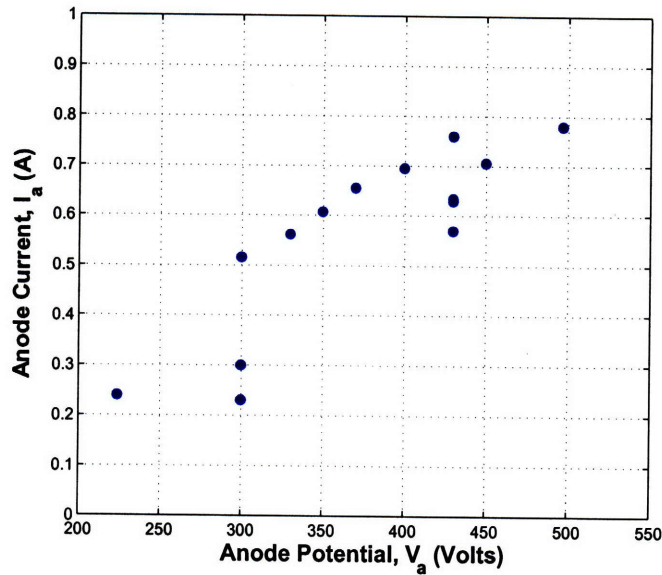
Figure 3-7: Measured anode current with increasing anode potential at a constant flow rate of 8.5*sccm*.

between 70 and 110V. Far greater than the nominal values, around $20V3.1.1$),when the same cathode is operated with commercial Hall thrusters. Given the impact of moving the cathode from positions A to B, the cathode was moved to position C before further testing. At this position, the field strength was about half that at position B ($\sim 50Gauss$). In addition the cathode tip was closer to flux lines which intercept the body a points closer to the thruster exit plane, as can be see in Fig. 3-2.

3.2.2 Further Testing at SPL

With the cathode in position C a more stable discharge was produced. Several anode potential scans were performed at SPL with a fixed thruster configuration. During all tests the flow rate was held constant while the applied anode potential was varied. The resultant current measurements are presented in Figure 3-8. During these scans the maximum anode power was $538W$, occurring at a flow rate of $10.0sccm$ with $600V$ applied to the anode. The mean chamber pressures were $2.6 \times 10^{-5}Torr$, $3.6 \times 10^{-5}Torr$ and $4.1 \times 10^{-5}Torr$ at flow rates of $7sccm$, $8sccm$ and $10sccm$ respectively. The thruster run time was less than 35 minutes during each of the scans reported here. The thruster was shut down for roughly

10 minutes to cool between scans.
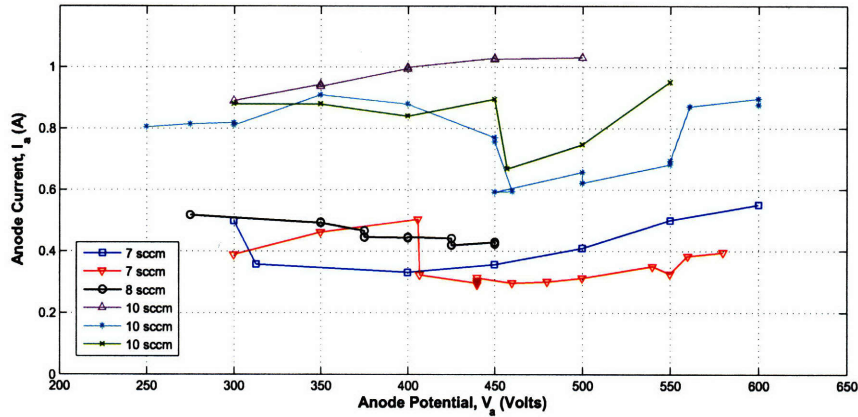
Figure 3-8: Anode current with varying anode potential at the flows indicated.

The scans revealed two modes of operation with a transition manifested by a sharp drop in both anode current and cathode keeper potential as the anode potential was increased. Visually, the discharge before the transition had a diffuse yet intense appearance while after the transition a bright, compact plume was visible near the thruster exit plane and a clear conical shell could be seen. Figure 3-9 shows photographs of the thruster operating in the two modes. Figure 3-10 is a zoomed photograph of the typical plume near the exit plane when operating in the low current mode. The conical visible plume diverges at roughly $33°$, or $11.5°$ greater than the discharge channel divergence. To reproduce the transition between modes, the potential scans were repeated several times at 7.0 and $10.0 sccm$ with sufficient time allocated between trials for the thruster to cool down. As shown in the figure the transition point was recreated at approximately $450V$ to the anode during two independent scans at $10.0 sccm$, however; a third scan did not recreate the transition. In this case the anode current continued to rise with increasing anode potential. Similarly at $7.0 sccm$, the transition point shifted from approximately 300 to 410V between scans. At $8.0 sccm$ no transition occurred and visual observations confirmed that the thruster operated in the lower anode current state throughout the scan. A connection between cathode keeper potential and mode transition was also observed during the voltage sweeps. As shown in Figure 3-11 for selected scans at 7.0 and $10.0 sccm$. Here both the anode current and keeper potential are seen to drop at the same applied anode potential. Although the keeper voltage and anode current drops are consistent, as anode potential was increased further the keeper

(a) Visible discharge operating in the high anode current mode. Operating with 10 sccm of anode flow and 400 Volts applied to the anode.
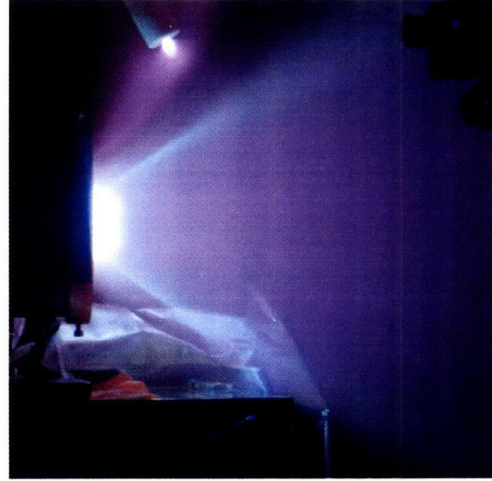
(b) Visible discharge operating in the low anode current mode. Operating with 10 sccm of anode flow and 450 Volts applied to the anode.

Figure 3-9: Photographs of the two characteristic modes of operation of the DCF thruster.

potential began to increase during the $7.0sccm$ scan but remained low at $10.0sccm$.

3.2.3 Thrust Measurements at Busek

As described in section 3.1.3 the thruster was moved to the Busek facility for thrust measurements to be made. During these trials the cathode and anode positions were not changed from those during trials at SPL. Three scans at flow rates of 7.0, 8.5 and $10.0sccm$ were performed.

The anode currents with varying potential during these trials are shown in Figure 3-12. In reference to Fig. 3-8, the thruster operated in the lower current mode during the entire trial at $7.0sccm$. This was confirmed through visual observation as the plume appeared similar to Fig. 3-9(b). At $8.5sccm$ a characteristic drop in anode current was observed at approximately $450V$. At $10.0sccm$ the thruster operated in the high current mode, visually similar to Fig. 3-9(a). During this final scan, the thruster was shut down at $V_a = 400V$ due to arcs observed between the thruster and cathode. The mean chamber pressures were $3.2 \times 10^{-6}Torr$, $3.7 \times 10^{-6}Torr$ and $4.3 \times 10^{-6}Torr$ at flow rates of $7.0sccm$, $8.5sccm$ and $10.0sccm$ respectively. The thruster run times were roughly 45 minutes for each completed scan. Similar to the scans performed at SPL, the thruster was shut down to cool for several minutes between scans.

58
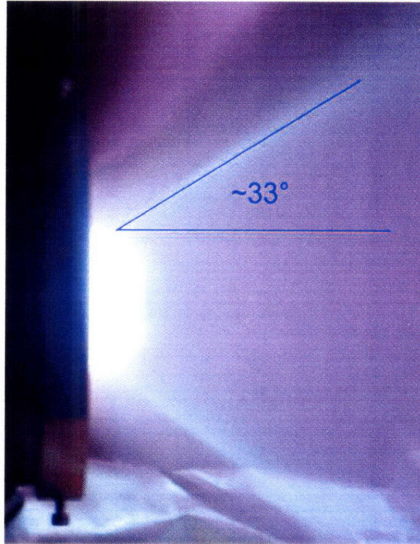
Figure 3-10: Divergence angle of the visible plume when operating in the low current mode. When the more diffuse plume is present it appears to be bounded by a cone with a similar angle.

The cathode was again current regulated to $0.25A$ during the experiments at Busek. The cathode keeper potential did not reach the high levels observed at SPL in either mode of operation, as seen in Figure 3-13. However, the keeper potential rose slightly from $20V$ to $24V$ after the transition with $8.5sccm$ of flow. The anode power levels during the three scans are presented in Figure 3-14. The power levels ranged from $102W$ to $376W$. Thrust measurements taken at Busek are presented in Figure 3-15. Measured thrusts ranged from 6.0 to $16.0mN$ over all trials. The uncertainties, indicated on each curve, were estimated from the standard deviation of the recorded data and were less than 20% throughout the experiments. During the apparent mode transition at $V_a = 450V$, while at $8.5sccm$ of anode flow, the thrust decreased. Otherwise, the thrust was seen to increase with applied anode voltage.

Thrust measurements along with the current data in Fig. 3-12 allowed for the anode thrust efficiency and specific impulse to be calculated using equations 2.2 and 2.3. The anode thrust efficiency is plotted in Fig. 3-16. The uncertainties shown in the figure were derived from the statistical fluctuations in thrust, shown in Fig. 3-15, only. The efficiency was greatest during the $8.5sccm$ scan where the mean was over 40% at all times and had a maximum of 44.5% occurring with $550V$ applied to the anode. Here, a thrust of $13.4mN$ was measured while the DCF consumed $242W$ of anode power.
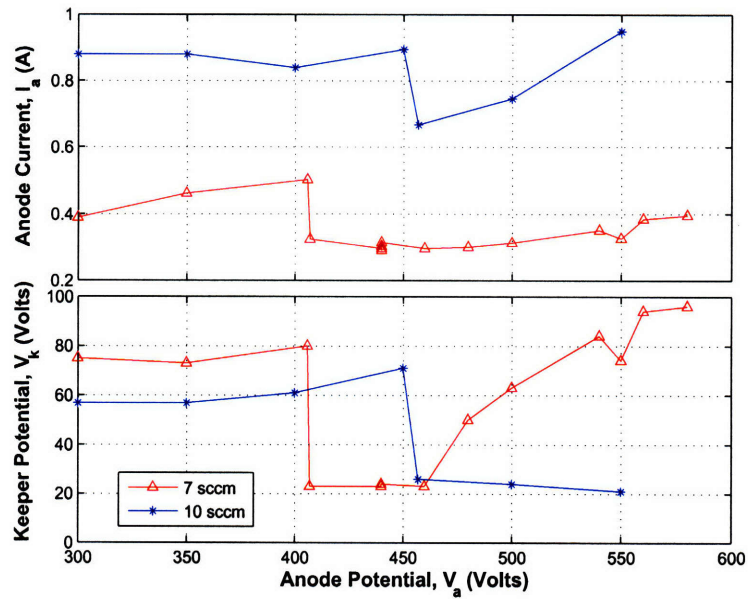
Figure 3-11: Simultaneous drop in both anode current and cathode keeper potential during mode transition.

The specific impulse is plotted in Fig. 3-17. Again, the uncertainties shown were derived from the fluctuation in thrust only. With the exception of the mode transition at $8.5 sccm$ the I_{sp} increased at a rate compatible with the expected square root dependence on anode voltage, see Figure 3-18.
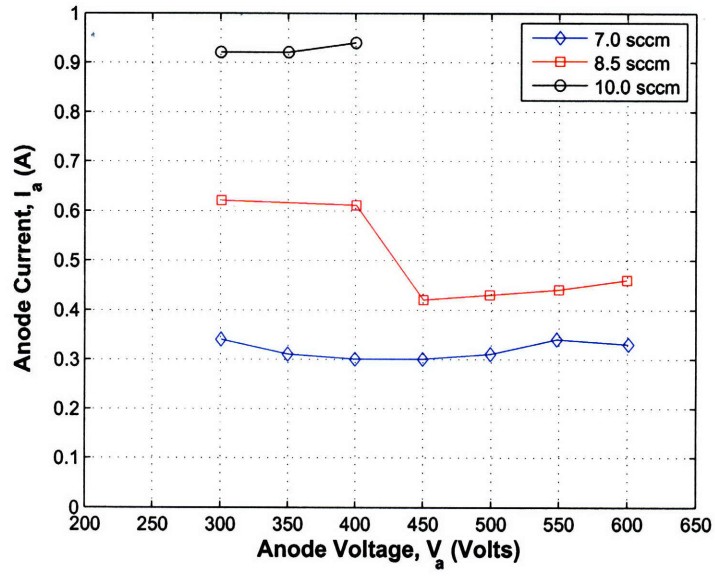
Figure 3-12: Anode current taken at the Busek Company.
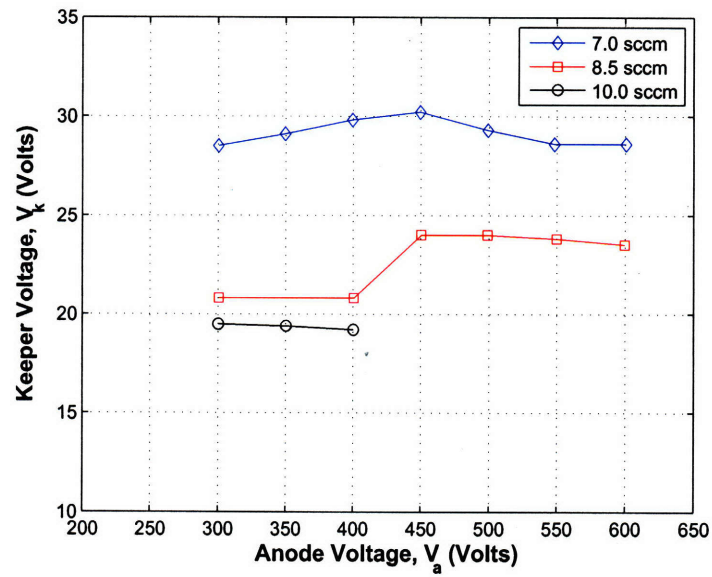
Figure 3-13: Keeper potential during scans at the Busek Company.
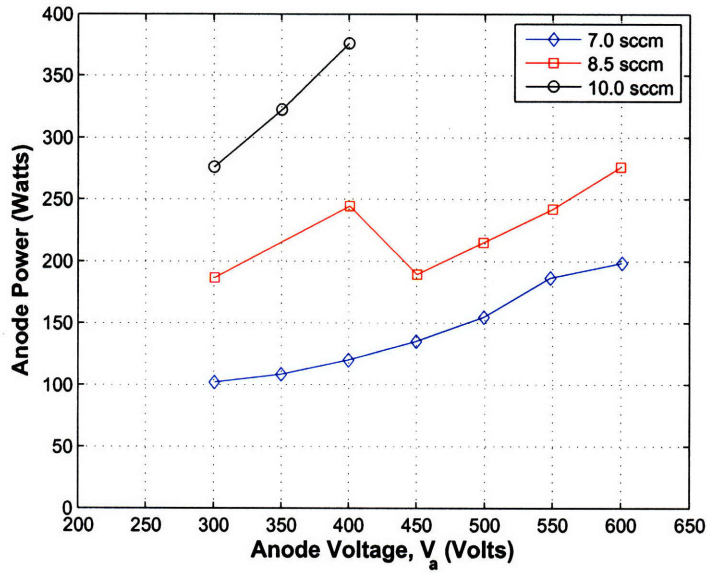
Figure 3-14: Anode power anode power levels, the power consumption at the peak efficiency point ($8.5sccm$,$550V$) was $242W$.
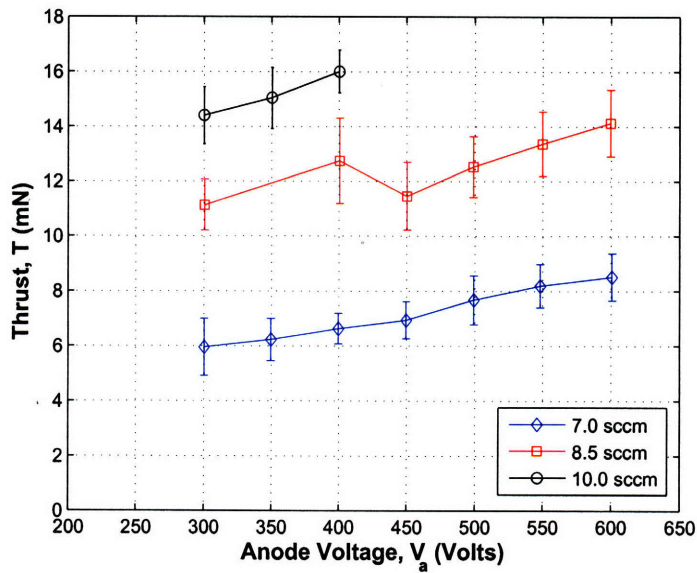
Figure 3-15: Thrust measurements taken at the Busek Company, the indicated uncertainties represent the standard deviation of the recorded data for each anode potential.
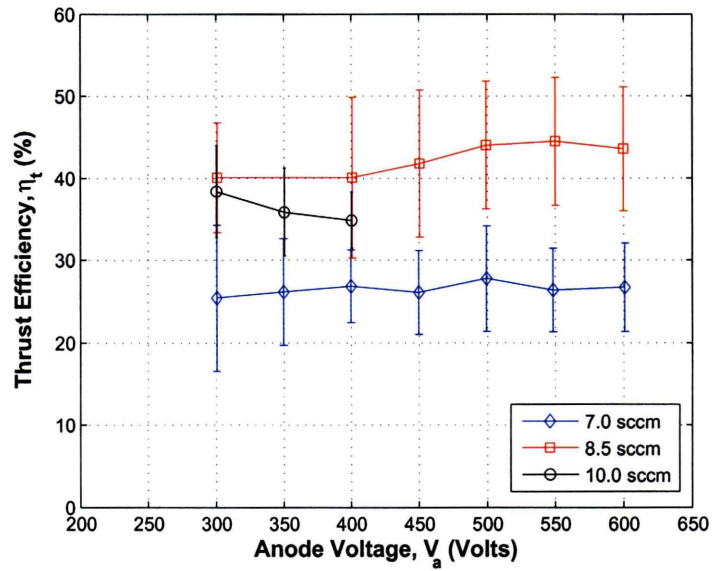
Figure 3-16: Anode thrust efficiency taken at the Busek Company.
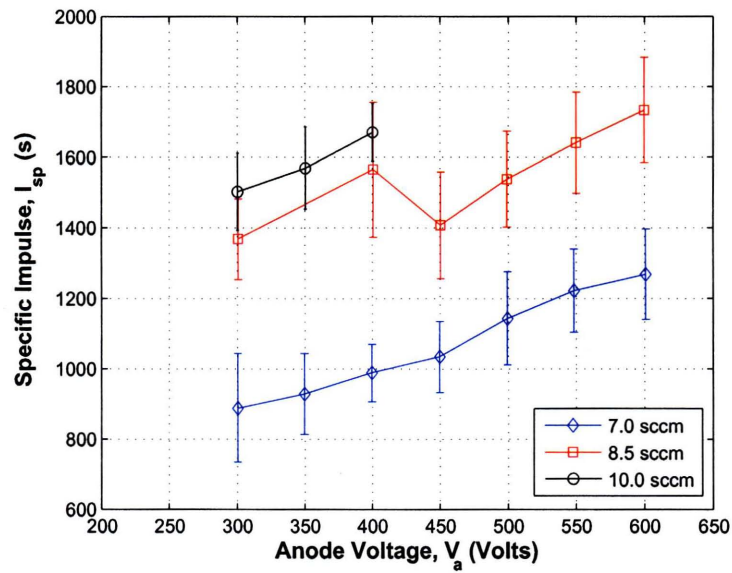
Figure 3-17: Anode specific impulse measurements taken at the Busek Company.
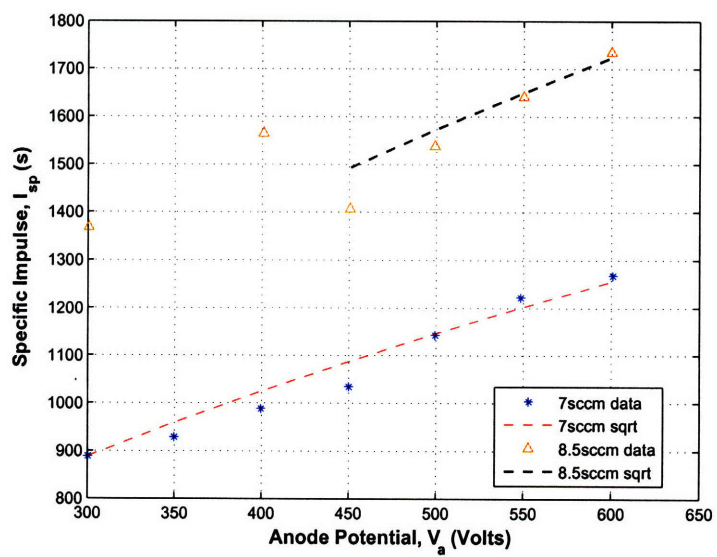
Figure 3-18: Square root dependence of specific impulse on anode potential.

3.3 Preliminary Results Summary

Details of operating modes observed during the initial characterization are briefly summarized in this section. In addition, observations of the magnetic fields impact on cathode behavior and basic design modifications made after the results presented in this chapter are discussed.

3.3.1 Observed Bi-Modal Operation

During both the SPL and Busek trials the DCF demonstrated two apparently distinct modes of operation. As shown in Figs. 3-8 and 3-12, the mode transitions were characterized by a drop in current. In addition a change in the visual appearance of the discharge occurred after transition. During the high current mode a more diffuse beam was present, although a divergent conical shape continues to be visible. Images of thruster operating in both modes were show in in Fig. 3-9. While testing at SPL, the cathode keeper voltage decreased suddenly during the transitions(Fig. 3-11); however, a slight increase in keeper voltage was seen while testing at Busek (Fig. 3-13).

Referring to the data taken at Busek, a mode transition was observed at a flow rate of 8.5$sccm$ but was not observed at 7.0$sccm$ or 10.0$sccm$. This phenomenon therefore appears to depend both on anode potential and and flow rate. Comparing the behavior of the thrust and anode thrust efficiency at 8.5$sccm$ in Figs. 3-15 and 3-16 we observed that, despite a drop in thrust after the mode transition, the efficiency increased slightly. Therefore the second mode may be, overall, a more efficient state.

These transitions are a central theme of the diagnostic measurements presented in the following chapter and an explanation of the behavior is postulated in section 5.1.Throughout the remainder of this report, the high and low current operating modes will be referred to as **Mode 1** and **Mode 2** respectively.

3.3.2 Cathode Coupling

Figure 3-19 shows the simulated magnetic field overlaid onto the plasma discharge with the cathode at position C of Fig. 3-2. It is apparent from the figure that electrons emitted from the cathode may follow magnetic field lines. This suggests that the abnormal keeper behavior may have been caused by interactions with the magnetic field. The connection
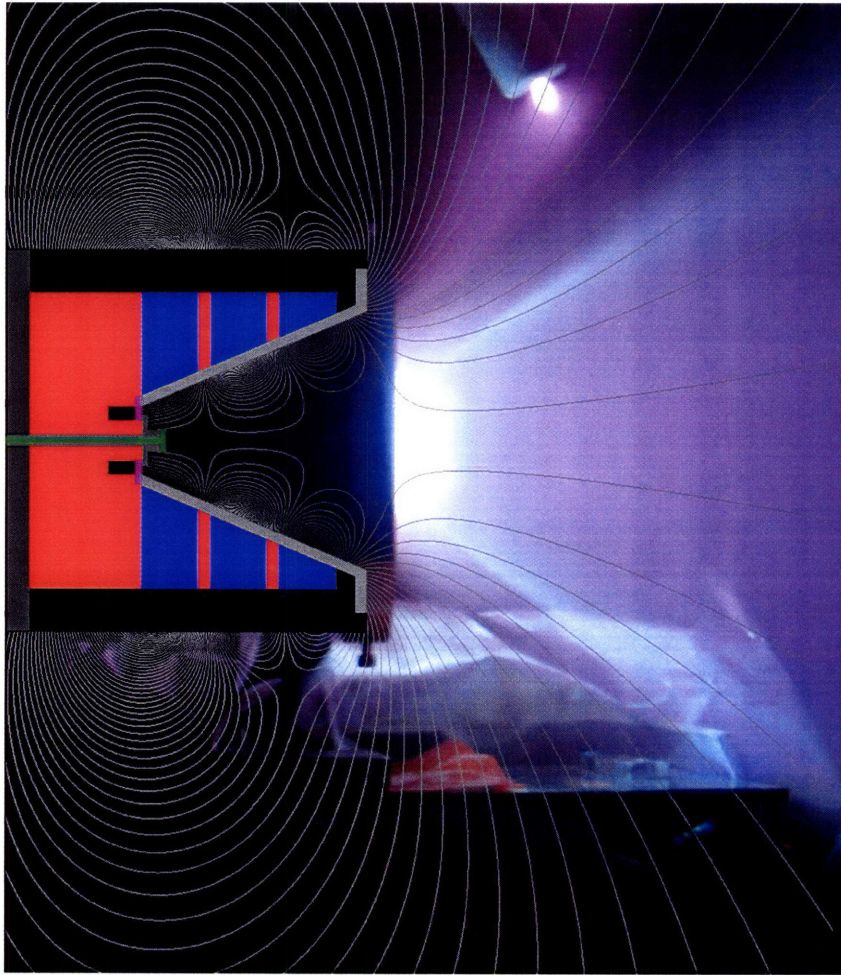
Figure 3-19: Simulated magnetic field overlaid onto the visible plume.

between cathode position and thruster operation was solidified after the first successful trial, Fig. 3-6, when moving the cathode to position C resulted in stable behavior during the remaining trials both at SPL and Busek. Given these observations the cathode position likely played a role in allowing for a discharge after the cathode was moved from positions A to B, however the anode was also reconfigured so the effects cannot be clearly distinguished.

3.3.3 Anode and Diffuser Modifications

Testing at Busek was halted at $10.0 sccm$ of flow and an anode potential of $400V$ when arcing was observed by the operator. Upon retrieving the thruster from Busek a thick
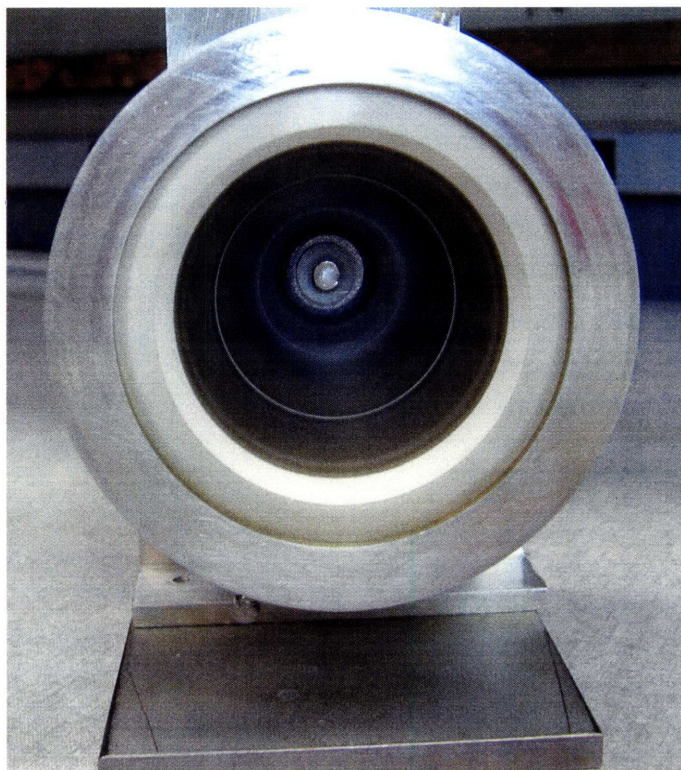
Figure 3-20: The DCF thruster after firing at the Busek company. The material deposited on the walls was electrically conduction. Also note the damage to the anode tip at the center of the channel.

deposition layer and damage to the anode were observed, see Figure 3-20. After inspection of the anode damage, shown in the figure, it was apparent that sputtering of the stainless steel surface had occurred, this was reinforced as the deposited material on the channel walls was electrically conducting. Although this was deemed undesirable, the tendency for significant deposition to occur in well defined rings, as seen in the figure, forms the basis for the discussion of erosion observations in section 5.2.2.

The arcing observed may not have been directly caused by deposition, rather an arc path was found between the anode post and the diffuser ring. Referring to Fig. 2-13, the insulating washers in the anode region also serve to restrain the diffuser ring in this prototype design. As a result, a slight bulge in the diffuser surface could have produced a path for propellant gas between the diffuser, at floating potential, and the high potential anode post. Based on the observed damage, this was presumed to be the cause of the arcing. In order to correct both the deposition and arcing problems two minor design
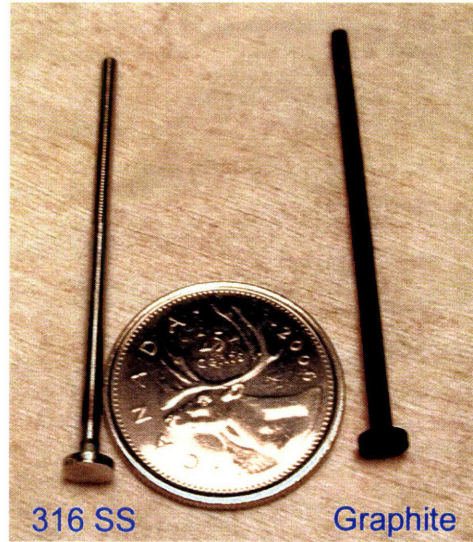
Figure 3-21: The original stainless steel anode and the new graphite anode. The anode dimensions were identical.

modifications were made. The stainless steel anode was replaced with a graphite anode made from a single piece of type AXF-5Q *Poco* graphite, shown in Figure 3-21. Graphite was selected due to its low sputter yield[39] compared to stainless steel and good electrical behavior[40]. The anode dimensions were identical to the previous stainless steel anode (with a few percent error due to precision levels obtainable while machining). The anode tip position was maintained $5mm$ from the core stem as in all trials after section 3.2.1. One complication of this configuration was the difficulty inherent in making a robust electrical connection to the fragile graphite rod. A well insulated spring loaded clip was used but was not very robust. Finally, to reduce arcs to the anode post a new diffuser was constructed with manufacturing efforts focused on ensuring no bulge was present.

Chapter 4

DCF Exploratory Diagnostics

4.1 Review of Diagnostic Probe Theory

The favorable performance and bi-modal operating modes described in the previous chapter support further studies of the DCF thruster. As a precursor to an in depth study beyond the scope of this project, some preliminary diagnostics using both a Faraday probe and Retarding Potential Analyzer (RPA) have been performed. Before presenting the results, this section briefly describes the operational principles of both probes and the information they provide. Both probes used were designed by Yassir Azziz[6]. For more rigorous descriptions of their development please consult the cited source.

4.1.1 Faraday Probes
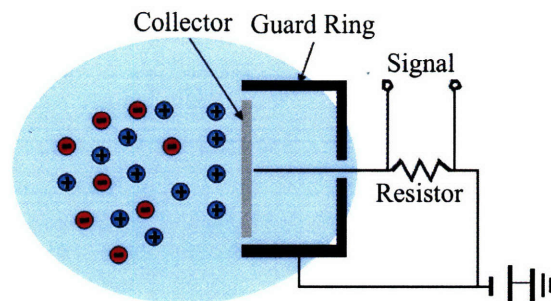
Figure 4-1: Basic construction and operating principles of the type of Faraday probe used in this study (image source[6]).

Faraday probes measure ion current density by collecting ions incident on a charged plate. A schematic overview of a typical Faraday probe is shown in Figure 4-1. A negative potential, approximately $30V$ below the plasma floating potential, is applied to the plate while the current is observed. The bias is assumed to be sufficient to repel electrons, while ions are collected. In the case of a thruster plume, where the majority of ions are streaming away from roughly a point source, the collected ion current is assumed to be, primarily the beam current. The guard ring shown in Fig. 4-1, is included to both repel ions not traveling on axis and reduce the impact of non planar electric fields that would otherwise form on the probe edges. The probes plates are typically constructed from tungsten given its low secondary electron yield[6]. A correction factor accounting for this yield is sometimes used[41], however given the low ion energies expected and the exploratory nature of this study no such correction will be considered here. The current density, at the location of the probe is approximately,

$$j = I_p/A_p, \tag{4.1}$$

where j is the current density(A/m^2), I_p is the collected current$(Amps)$ and A_p is the probe collector area(m^2). The probe used in this study had a collector diameter of $4.45mm$, with a $6.35mm$ guard ring[6]. As an example of Faraday probe applications, Figure 4-2 shows normalized ion currents collected from a Busek BHT-200 Hall thruster plume at varying angular positions a fixed radius from the exit plane. In the figure the same probes and experimental setup which were used in diagnosing the DCF thruster plume were used. The peaked structure is typical of traditional Hall thrusters. If the current density is known the total beam current can be estimated by integration assuming a symmetric plume. That is,

$$I_b = 2\pi R^2 \int_0^{\frac{\pi}{2}} j(\phi) \sin(\phi) d\phi, \tag{4.2}$$

where ϕ is the azimuthal angle and R is the fixed radial distance from the thruster exit plane. The beam divergence, ϕ_b is often then taken to be the angle that encloses a given percentage of the total beam current[18].

4.1.2 Retarding Potential Analyzer (RPA)

The RPA is designed to measure the distribution of ion energies at the probe location. A schematic of a typical RPA probe is shown in Figure 4-3. The basic principle of the RPA

70
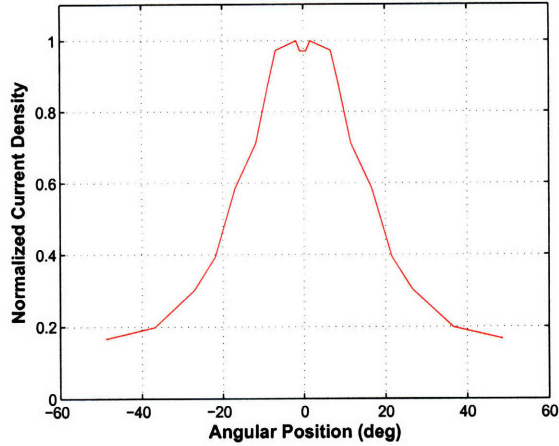
Figure 4-2: Sample data of a typical Hall thruster angular current density scan using a Faraday probe. The current has been normalized in this example.

is to collect only ions above a set threshold energy. This is accomplished by varying the potential of a retarding grid and measuring the current, presumably from ions, that reaches a collector. Referring to the figure, the actual configuration is more complicated. The first grid is floating to reduce the impact of the probe on the surrounding plasma, the second grid is biased further below the floating potential so as to repel the electron flux, the third grid repels ions and finally the ion current is measured at a collector. Some RPA probes use a fourth grid to suppress any secondary electron emission from the ion retarding grid[17], this is not employed in this probe. The probe used in this study had constant grid diameters of $6.35mm$ housed inside a $12.7mm$ diameter casing. It can be shown that the ion acceleration distribution function is ideally related to the collected current by equation 4.3.

$$\frac{dI}{dV} = -qAn_i \left(\frac{2eV}{m_i}\right)^{1/2} \frac{1}{V_a} f(\xi) \tag{4.3}$$

In equation4.3, $\xi = V/V_a$ and $f(\xi)$ is the ionization distribution function[9], such that the number of beam ions created between V and dV is proportional to $f(\xi)dV$.

4.1.3   Interpretation of Results

Recall from equation 2.2 of section 2.1.1, that the anode efficiency relates the total beam power to input power. Also in section 2.1.1, the anode efficiency was broken up into a

71
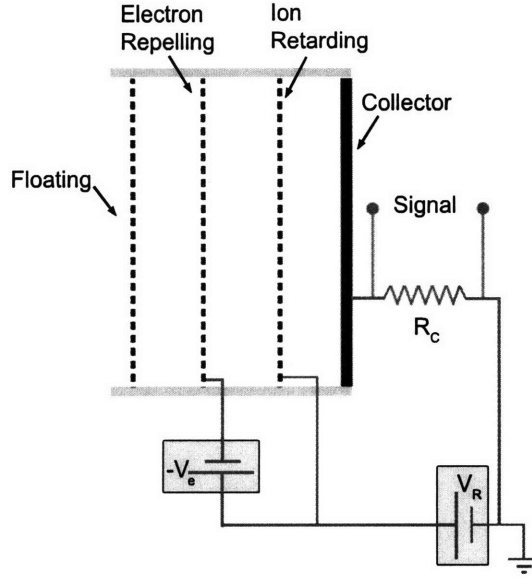
Figure 4-3: Basic construction and measured signals of the RPA probe used in this study, see Azziz[6] for details. The electron repelling grid is biased below the floating potential at $-V_e$, while the retarding potential is positively biased at V_R.

product of efficiencies and coefficients. With Faraday and RPA data, those values may be estimated in order to gain insight into the DCF thruster characteristics. Specifically, given the total beam current and an estimate of the beam divergence from the Faraday profile we may estimate the beam efficiency, η_b with equation 4.4, the utilization efficiency η_u with equation 4.5 and the divergence coefficient $cos^2(\phi_b)$.

$$\eta_b = \frac{I_b}{I_a} \tag{4.4}$$

$$\eta_u = \frac{I_b}{I_n} \tag{4.5}$$

Using the estimated ionization distribution function from the RPA measurements, the acceleration efficiency or non-uniformity factor η_E can be found using equation 4.6[9].

$$\eta_E = \left(\int_0^1 \xi^{1/2} f(\xi) d\xi \right)^2 \tag{4.6}$$

In order to evaluate equation 4.6, equation 4.3 can be rearranged to provide a relationship between ion distribution and measured current, as in equation 4.7.

$$f(\xi) = -\frac{V_a}{\kappa} \frac{1}{V^{1/2}} \frac{dI}{dV}. \tag{4.7}$$

In equation 4.7, κ is approximately constant and can be solved through normalization of the distribution function $f(\xi)$. The final relation, in terms of only measured quantities is given in equation 4.8.

$$\eta_E = \left(\frac{\frac{1}{V_a^{1/2}} \int_0^{V_a} \frac{dI}{dV} dV}{\int_0^{V_a} \frac{1}{V^{1/2}} \frac{dI}{dV} dV} \right)^2 \tag{4.8}$$

If it is assumed that all ions are singly charged (charge efficiency, $\eta_c \approx 1$), the Faraday cup and RPA data thus produce both an estimate of the overall efficiency, using equation 2.4, and provide some understanding of what aspects of the thruster are, or are not, performing efficiently. It should be noted that the assumption of singly charged ions may be poor given reports of multiply charged ions with other cusp field thrusters[18].

4.2   Set Up of Diagnostics Equipment

The experimental configuration used when diagnosing the DCF thruster plume using both a Faraday probe and an RPA are discussed here. Both probes were mounted radially, $30cm$ from the thruster exit plane on a rotating arm, as shown in Figure 4-4. The probe operating principles were described in section 4.1. The swinging arm was controlled externally using a simple $C++$ interface and basic switching circuit to control a *TMG-5609*, 0.9 degree per step stepper motor. The step motor was not vacuum rated and hence did not perform well in vacuum. As a result, accurate positioning of the motor was not possible and the position was determined visually using reference lines in the tank shown schematically in Fig. 4-4 and photographed in Figure 4-5. The Faraday cup and guard ring were biased to $-20V$ using
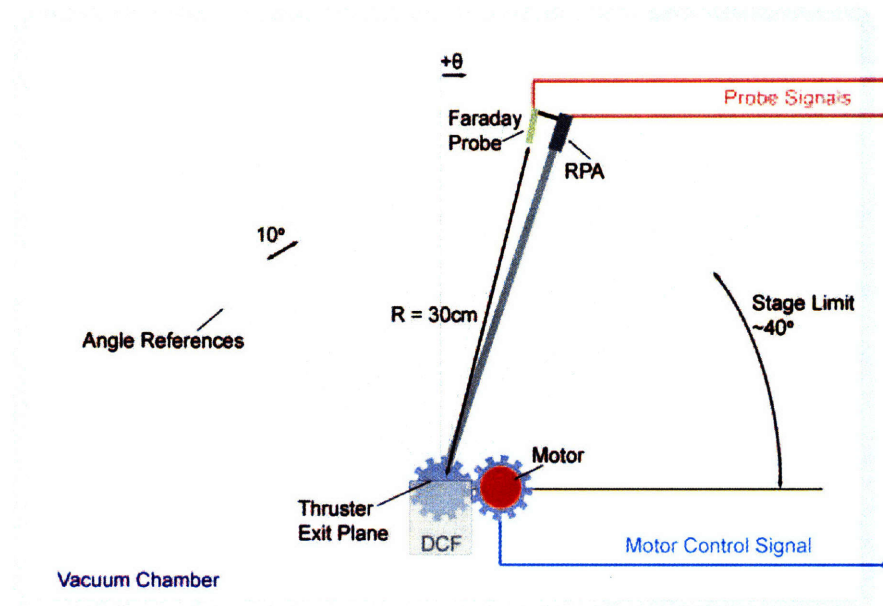
Figure 4-4: Schematic overview of the configuration used when taking diagnostic data of the DCF plume. Both the RPA and Faraday probe were $30cm$ from the thruster exit plane.

a *TENMA 72-6615* DC dual power supply. Collected current was recorded by measuring the voltage across a 129.1Ω shunt resistor, as shown in Fig. 4-1. The signal voltage was measured with a hand held voltmeter. The RPA ion retarding grid was controlled using a *Matsusada AMS-5B6* high voltage power supply. The electron repelling grid was biased to $-30V$ using the *TENMA* power supply. Current was recorded by measuring the voltage,

with a hand held multi meter, across a $99.5k\Omega$ shunt resistor, labelled R_c in Fig. 4-3. All probe potentials were referenced to a common local power supply ground.
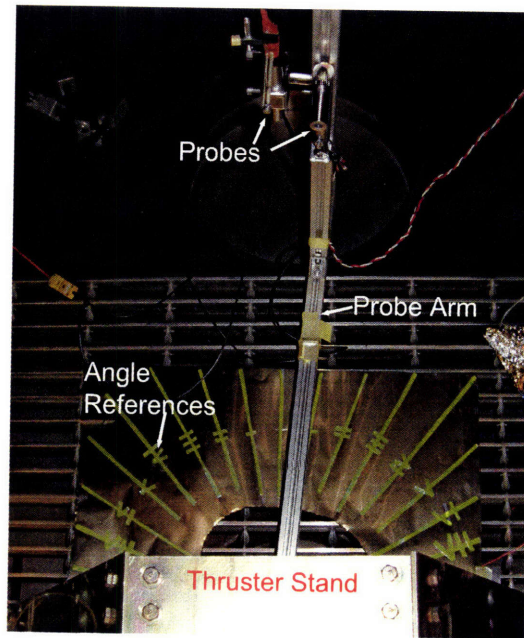
(a) Photograph of diagnostic set up with the thruster removed. Angles were measured visually using the indicated references.
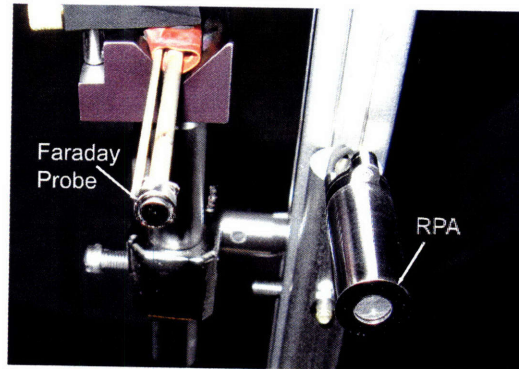
(b) The Faraday probe and RPA used during these measurements.

Figure 4-5: Diagnostic probes and experimental setup.

4.3 RPA and Faraday Probe Results

Results from both the Faraday and RPA probe measurements are presented in this section. Prior to presenting those results, the thruster configuration and general behavior observed during the tests is discussed.

4.3.1 Thruster Behavior

The cathode configuration remained at position C of Fig. 3-2. It was not moved during the time between the Busek trials and the results presented here. The graphite anode, discussed in section 3.3.3, was used in all trials presented here. Recall that the surface area and location of the anode were identical to the stainless steel anode used while testing at Busek. A current sweep was performed prior to the testing presented here in order to gauge the consistency between the following trials and those at Busek. As seen in Figure 4-6, the scans, performed at $8.5sccm$ did not agree well those at Busek. In addition, while running for durations beyond those performed either during preliminary SPL trials (section 3.2.2) or at Busek, the current was observed to slowly increase over time. These discrepancies are discussed further in section 6.4.5. Due to these concerns, for all trials presented here, the total test durations were limited to maintain anode currents within a few percent.

4.3.2 Faraday Probe Analysis

Probe sweeps were performed at $300V$ and $450V$ to the anode. At $300V$ in the high current mode 1, the total anode current was approximately $0.71 \pm .1A$ throughout the scan. The results are presented in Figure 4-7. At an anode potential of $450V$, the thruster operated in the second, lower current, operating mode. Here the anode current was approximately $0.52 \pm .1A$. Compared with the sample data presented in section 4.1.1, the differences between the DCF discharge and a typical Hall thruster are clear. Specifically an annular discharge was observed with peaks at roughly $34°$ and $32°$ during the first and second modes respectively. However; these angles are highly approximate given the results were not perfectly symmetric, suggesting either a misalignment of the apparatus or unsymmetrical discharge. The probe radial arm could not reach angles beyond $\pm45°$. The ability to probe the unique plume profile was hence extremely limited. Nevertheless, by extrapolation of smoothed spline fits of the curves in Figs. 4-7 and 4-8, cut off at $\pm50°$, rough approximations

Busek and Recent Current Sweeps
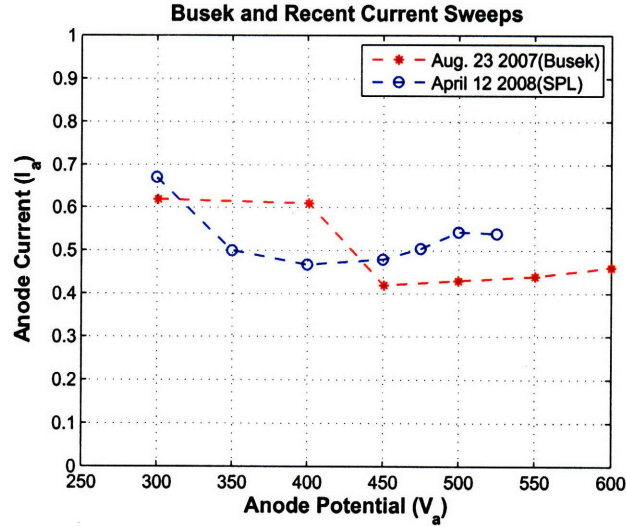
Figure 4-6: Anode current collected prior to collecting the data shown below (April 12, 2008) and current collected while testing at Busek (August 23,2008). In both cases the flow rate was $8.5sccm$.

to the beam current were possible.

The integrated approximate total beam currents were found to be $I_b = 0.53A$ and $I_b = 0.38A$, for the $300V$ and $450V$ scans respectively. At this flow rate, $8.5sccm$, the neutral flow "current" was $I_n = \dot{m}e/m_i = 0.71A$. At $300V$, using equation 4.4 the beam efficiency was hence $\eta_b = 77\%$ and, using equation 4.5, the ionization efficiency was $\eta_u = 89\%$. Similarly at $450V$, the beam and utilization efficiencies at were approximately $\eta_b = 83\%$ and $\eta_u = 69\%$ respectively.

4.3.3 RPA Probe Results and Analysis

Due limitations in the available propellant supply, the RPA measurements were limited to scans near the peak and thruster axis only. Specifically, scans at $28°$ and $-5°$ were performed at both $V_a = 300V$ and $V_a = 450V$. The recorded data were generally noisy. The noise can primarily be attributed to both the recording method (hand held voltmeter and shunt resistor) and the inability to allow proper settling of the recorded current as the retarding potential was varied. The later was a result of the tendency for the total anode current to drift when the thruster is operated for long durations, as discussed above.

Both the measured current and derivatives when the thruster operated in the high
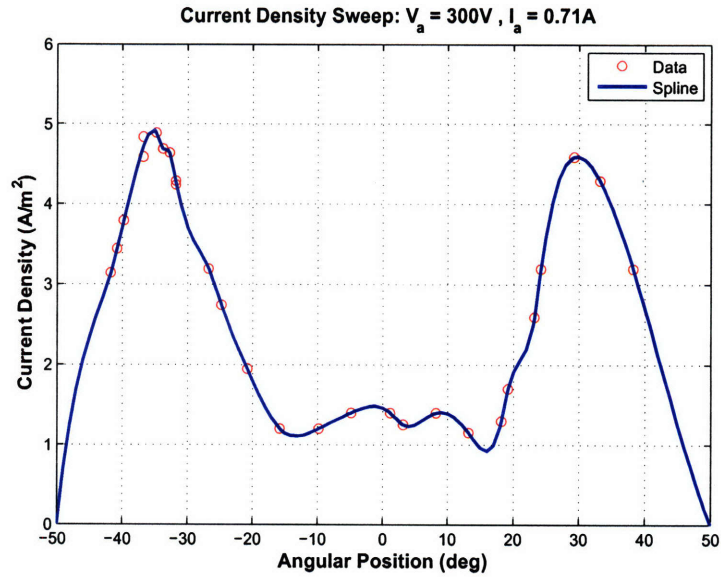
Figure 4-7: Current density data recorded with the anode potential at $300V$, the thruster appeared to operate in the first, high current, mode during this scan. Angles beyond $\pm45°$ could not be reached. The spline fit has been cut-off at $\pm50°$.
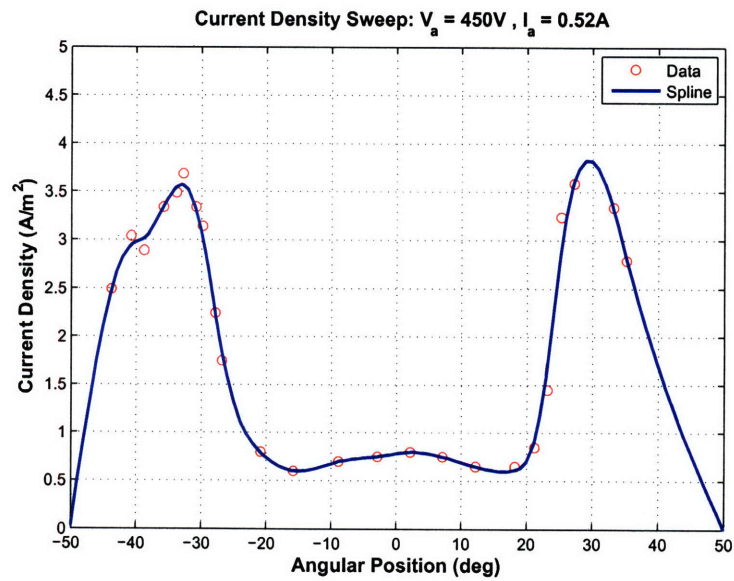
Figure 4-8: Current density data recorded with the anode potential at $450V$, the thruster appeared to operate in the second, low current, mode during this scan. Angles beyond $\pm45°$ could not be reached. The spline fit has been cut-off at $\pm50°$.
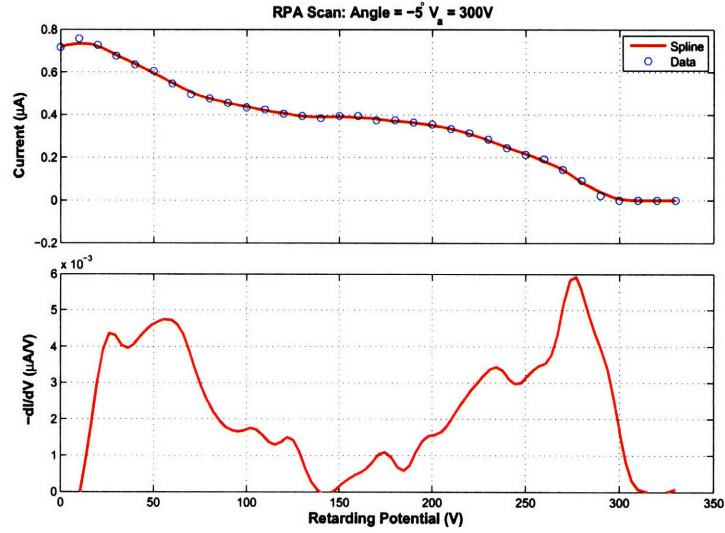
Figure 4-9: Recorded RPA measurements at $V_a = 300V$ with the anode current at $0.69 \pm 0.1A$ and the RPA positioned at $-5°$ from the center line.

current mode at $V_a = 300V$ are shown in Figures 4-9 and 4-10 for the $1°$ and $35°$ cases respectively. During these scans the anode current, I_a, was $0.69 \pm 0.1A$.

The scans were repeated in the low current mode with $V_a = 450V$, however the current levels at $-5°$ were below the minimum threshold which could be recorded using the scheme employed. As a result, only the data at $28°$ are presented in Figure 4-11. Here the anode current was somewhat unstable with a mean of $0.53 \pm 0.2A$ throughout the scan. In all figures, a spline fit was used to estimate the derivative. A clear variation can be seen between the operation in high and low current modes. During the high current mode the distribution appears to be spread out and, based primarily on Fig. 4-9, the ion energies appear to be spread between two peaks. Given that the $28°$ measurements were closer to the peaks observed in section 4.3.2, the results at this angle were used in equation 4.8 to estimate the non-uniformity factor. During the second, low current, mode shown in Fig.4-11, a thinner distribution focused closer to the anode potential ($450V$ was observed). The required integrations in equation 4.8 were performed using the spline fit data. At $V_a = 300V$ the estimated non-uniformity factor was 57% while at $V_a = 450V$ it was 84%.

79
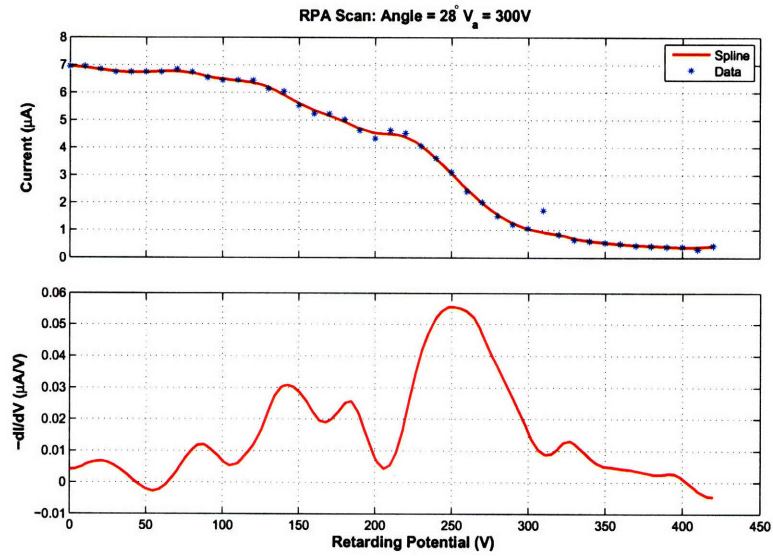
Figure 4-10: Recorded RPA measurements at $V_a = 300V$ with anode current of $0.69 \pm 0.1A$ and the RPA positioned at 28° from the center line.
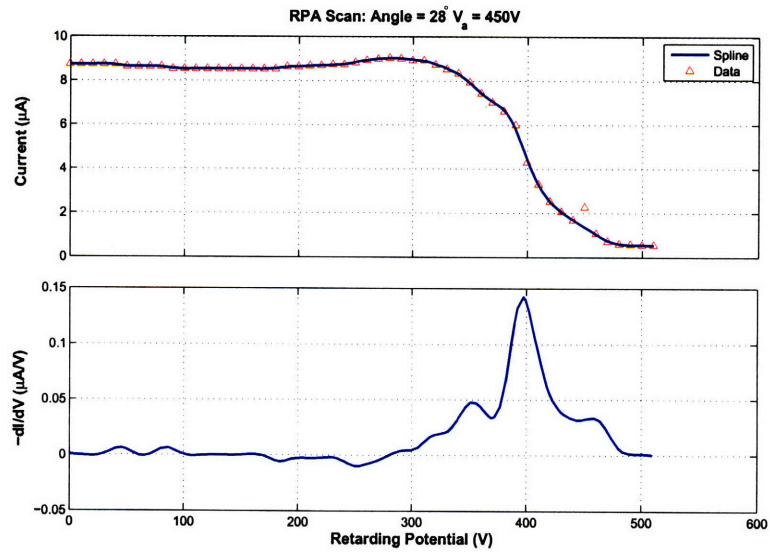
Figure 4-11: Recorded RPA measurements at $V_a = 450V$ with anode current of $0.53 \pm 0.2A$ and the RPA positioned at 28° from the center line.

4.4 Summary and Interpretation of Plume Diagnostics

The results of the RPA and Faraday measurements in terms of equations 4.4 to 4.8 and equation 2.4 are presented in Table 4.1 for the two potentials considered. In addition, given the anode power and voltage, the thrust was estimated using the first part of equation 2.4. Due to the peaked nature of the Faraday probe scans (Figs. 4-7 and 4-8) the non-uniformity factors calculated at 28° were used. The divergence angle has been taken as simply the peak location in the approximately hollow cone which was observed during both scans. This approximation was deemed suitable given that the limited angular range of the probes prevented more detailed estimates of the divergence.

Metric	Mode 1($V_a = 300V$)	Mode 2($V_a = 450V$)
Anode Current, I_a	$0.71A$	$0.52A$
Beam Current, I_b	$0.55A$	$0.43A$
Divergence Angle, ϕ_b	$34°$	$32°$
Utilization Efficiency, η_u	89%	69%
Beam Efficiency, η_b	77%	83%
Non-uniformity Factor, η_E	57%	84%
Anode Efficiency, η_t	27%	34%

Table 4.1: Summary of the diagnostic data presented in section 4.3.

Referring to the measurements taken at Busek, see section 3.2, the overall efficiencies were not consistent. This can likely be attributed to both the increased anode current and the highly approximate nature of the exploratory study presented in this chapter. What is perhaps more useful is that these results correctly reflected the trends between modes observed in section 3.2. That is, that while the mode transition was accompanied by a decrease in current, the overall efficiency only changed by a few percent.

The observed ratio of beam current to anode current (the beam efficiency) did not change greatly between modes (from 77% to 83%). However; both the utilization efficiency and the non-uniformity factors changed significantly. These measurements were made independently (using the Faraday and RPA probes respectively). As seen in table 4.1, the variations in these efficiencies were effectively interchanged thus reducing the impact on total efficiency. Given that this result is congruent with that from the Busek data, it could provide insight into the phenomenon causing mode transitions.

Chapter 5

DCF Further Observations and Conclusions

5.1 Operating Modes of the DCF

Throughout the results presented in the preceding chapters, the DCF demonstrated two modes of operation. This section reviews the characteristics of the mode transitions and a simple explanation for the phenomenon is discussed.

5.1.1 Review of Observed Modes

Two modes of operation have been observed throughout experimentation with the DCF thruster. Before offering a possible explanation for the cause, it may be of use to review and summarize the properties observed when a transition occurs:

- *Anode Current:* Sudden decreases in anode current are the primary diagnostic of the mode transitions. See Figs. 3-8, 3-12 and 5-2 for examples.

- *Visual Plume:* Before transition the plume near the exit plane appears diffuse, after transition a bright bulb is visible within a hollow cone shaped plume. In both cases the boundary of the plume appears conical, diverging at roughly 33°. Refer to Fig. 3-9.

- *Dependance on Flow Rate:* Figures 3-8 and 3-12 both indicated that the mode transitions were impacted by the flow rate.

- *Keeper Potential:* While testing at SPL, the keeper potential decreased dramatically after transition to mode 2, see Fig. 3-11. However, a slight increase was seen at Busek (Fig. 3-13) and no significant variation has been observed since.

- *Plume Profile:* In both operating modes the current densities were focused in a conical pattern, see Figs. 4-7 and 4-8. In mode 1 operation, relatively more current was collected along the thruster axis.

- *Beam Efficiency:* The ratio of approximate beam current to anode current did not vary significantly between modes, see table 4.1.

- *Utilization Efficiency:* The degree of propellant ionization was significantly higher in mode 1 operation than in mode 2, see table 4.1.

- *Ion Energy Distribution:* In mode 1 operation the ion energies were spread over a wide range of energies, even suggesting two distinct peaks, see Figs. 4-9 and 4-10. In mode 2 operation the ion energy was well focused at energies close to the anode potential, resulting in a high non-uniformity factor, see Fig. 4-11 and table 4.1.

5.1.2 Proposed Explanation of Mode Transitions

A possible explanation for the bi-modal behavior could be a shift in the localization of back streaming electrons, and hence the plasma, from the cusp between the second and third magnets (call this C2), to the lower cusp/anode bottle region(call this C1). Throughout the remainder of this section this, rather simple, explanation is shown to be consistent with the list of observations detailed above. However, no theory explaining the physical processes which trigger the transition is presented at this time.

The most obvious trait which can be explained by this proposal is the variation in ion energies. If plasma were contained at both cusps C1 and C2, then ions created at those locations would be accelerated through different potential drops. In mode 1 operation a more diffuse distribution, with two peaks would be expected due to ions being created in both the C1 and C2 regions. In mode 2 operation ions would primarily be created at C1 and receive the bulk of the applied potential drop, as observed. The visual change in the observed plume is also explained simply by this explanation as the bulk of the ionizing plasma would be physically moved upstream within the thruster where it is no longer visible.

84
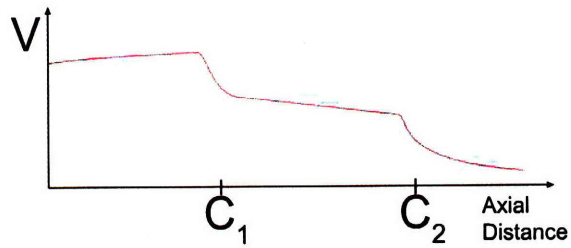
(a) Postulated potential profile while operating in mode one.
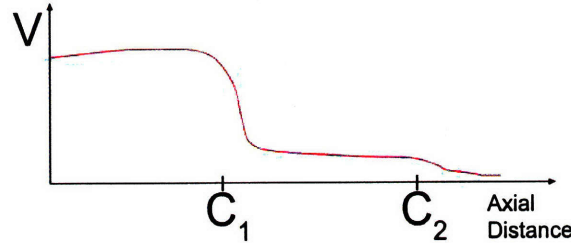
(b) Postulated potential profile while operating in mode two.

Figure 5-1: Possible potential profile moving axially along the DCF discharge channel when operating in the two observed modes.

The number of excited ions reaching the exit plane would hence decrease.

The observations of reduced overall anode current, and reduced ionization efficiency can be justified given this transition theory in conjunction with the observation that beam efficiencies did not vary greatly between modes. Axial magnetic confinement at C1 through both Hall currents and magnetic gradients near the anode would likely exceed that at C2 where there is no strong axial magnetic bottle and the mean magnetic field across the discharge channel is significantly less than at C1. Refer to Fig. 2-8 for the field strengths within the thruster. Thus better confinement resulting in reduced back streaming would be consistent with the plasma moving upstream. However; even if the electrons were ideally confined in the C1 region, the degree of ionization is influenced by the ability for neutral atoms to collide with electrons. Specifically, it was previously mentioned in section 2.2 that a potential drawback of the DCF arrangement could be that plasma is confined away from the walls to such a degree that neutrals are able to stream between the plasma and channel wall. In the first mode, with plasma confined both at C1 and C2, neutrals which circumvent the strong confinement region at C1 may be ionized when passing through the C2 region. However, in the second mode where the plasma is strongly confined only at C1, the flux of

neutrals which avoid ionization both by flowing around the confined plasma or by traveling through it without being ionized, would be lost to the plume. Thus, the high confinement at C1 may be responsible for low utilization efficiencies in the second mode.

Finally, the decreased total anode current can be shown to be directly linked to a decrease in back streaming current considering (1)the beam efficiencies were similar between modes, and (2)the utilization efficiency decreased. As a simple demonstration, assume the beam efficiencies were constant, thus assume that,

$$\frac{I_b}{I_a} = \frac{\eta_u I_n}{I_{bs} + \eta_u I_n} = \eta_b,$$ (5.1)

where η_b is constant. Solving for I_{bs},

$$I_{bs} = \eta_u I_n \left[\frac{1}{\eta_b} - 1\right]$$ (5.2)

where both the neutral current I_n and beam efficiency I_b are assumed constant here, so $I_{bs} \propto \eta_u$. In terms of anode current the result is,

$$I_a = \eta_u \frac{I_n}{\eta_b}.$$ (5.3)

So in the case of constant beam efficiency, $I_a, I_{bs} \propto \eta_u$. Hence decreased back streaming current through increased confinement at position C1 is consistent with decreased anode current and utilization efficiency so long as beam efficiency is approximately constant.

Despite offering reasonable explanations for the observed behavior, the actual phenomenon is likely far more complicated and may not be consistent with this simple explanation. For example, no attempt has been made to justify the near constant beam efficiencies observed. In addition, neither the impact of flow rate or the variations in keeper potential observed during some trials have been explained.

5.2 Additional Observations

Several observations concerning wall erosion and thermal behavior are presented in this section. These observations are largely qualitative and has a result, only speculative reasoning for the behavior is presented.

5.2.1 Performance Repeatability and Thermal Concerns

The DCF thruster performance has been found to vary over time. Particularly, the anode current of the prototype thruster begins to noticeably increase after roughly 30 to 40 minutes of operation at around $250W$ of anode power. Refer to Figure 5-2 where three sets of current measurements taken at $8.5sccm$ are shown. Both the Busek trial, and the first SPL trial were initiated with the thruster cool. The agreement between the curves was generally poor, with the most significant deviations apparent in the second SPL curve, taken after roughly 2 hours of continuous thruster operation. However; the mode transition point and general trend of the Busek curve was re-created in the second, high current curve taken at SPL. A
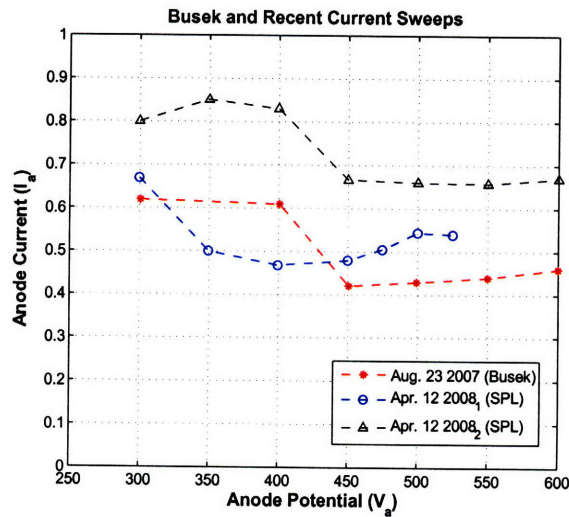
Figure 5-2: Selected anode current versus voltage measurements made throughout the test campaign, both at SPL and Busek.

simple explanation for this behavior could be that the magnetic structure is becoming hot and the field is degrading. If the field strengths decreased, particularly in approach to the anode, the back streaming current may have increased as magnetic confinement degraded.

A further note, not clearly represented by the data, is the settling time required when operating in mode 2 (low anode current). When testing for long periods of time, sharp transitions to low currents were constantly observed, however the anode current quickly rose by up to 25% before settling. Only the steady values have been reported in the data. If the mode transition theory suggested in the previous section is valid, it may also explain this behavior. With the plasma spread out along the channel, in mode 1 operation, the wall temperature would also be reasonably well distributed. When transition occurs and the plasma focused upstream, the wall temperature near the lower magnets could increase, leading to a localized hot spot which would reduce the magnetic field in that region.

5.2.2 Preliminary Erosion and Plasma Confinement Observations
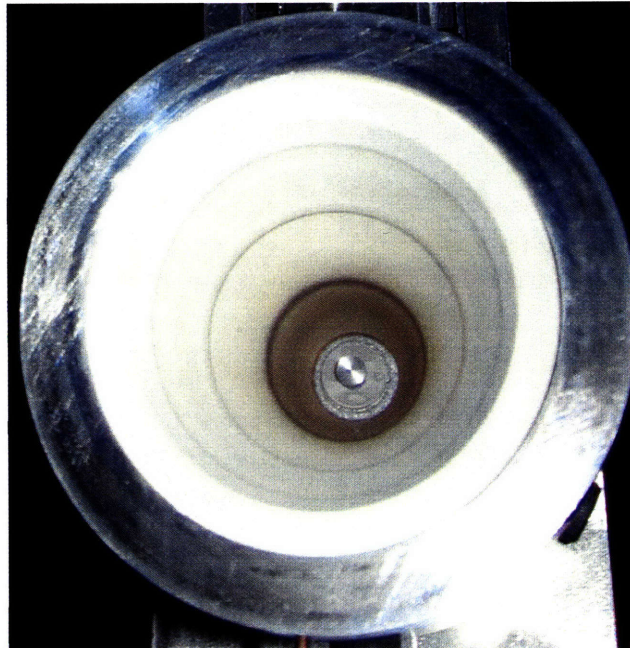
Figure 5-3: Boron Nitride cone after approximately 2 cumulative hours of firing. The three darkest rings coincide with the magnet boundaries.

Figure 5-3 is a photograph of the DCF conical discharge channel after approximately 2 hours of total firing time (comprised of several short trials lasting no more than 30 minutes each at SPL). The photograph is similar to Fig. 3-20 but is more typical of the profiles observed; in the Busek case the anode had been sputtered significantly. Distinct dark

bands are visible at each cusp. It is presumed that the dark bands represent sputtered material deposition while light bands represent regions where ion impacts are eroding the walls through sputtering. The amount of deposition transitions sharply at the cusps, with the most deposition closest to the anode. Figure 5-4, shows the approximate regions of deposition with respect to the magnetic field profile along the channel wall. The source of deposited material is unknown. It could include sputtered material from the fuel diffuser, the channel walls themselves, the anode or material from within the experimental facility. The general gradient in deposition downstream of the inlet could largely be attributed to the divergent channel area, and hence decreasing neutral particle density. Clear deposition patterns were observed near the two inner cusps, and at the exit plane.

Although the DCF configuration was intended to repel electrons through magnetic bottling(refer to section 2.2), it can be expected that electrons which do reach the walls will follow field lines (rather than diffuse across the fields). A negative sheath may form near the apex of the cusps where field lines intercept the channel walls, resulting in sputtering by ions accelerated through the sheath potential. However; at the cusps themselves, where magnetic gradients are strongest, electrons may be repelled sufficiently to prevent a negative sheath developing. This may begin to explain the localization of deposition and sputtering rings near the cusps. Light coloration, indicating significant sputtering, at the exit plane was observed where relatively weak field lines intercept the channel walls. The sputtering observed at this location in particular does offer further insight into the thruster operation in that it localizes a region of high energy ion impacts. Suppose ions are created in the anode-cusp region at the thruster base but, by the calculation in section 2.3, have sufficiently large Larmor radii to be considered non-magnetic. The ring of erosion at the exit plane would then suggest that the observed beam profile is limited by the channel walls. However; this upper ring of erosion appears to terminate at an axial point approximately equal to the final magnet edge. This suggests protection of the walls through either electron confinement of a plasma or deflection of magnetized ions. If the former is true, then the theory of localized plasma near the thruster base may not be valid.

Figure 5-5 is a photograph of the DCF plume taken at an angle just off the thruster symmetry axis. The brightest region of the thruster plasma is localized away from the ceramic walls. This further suggests that the cusped fields are protecting the surface, as desired.
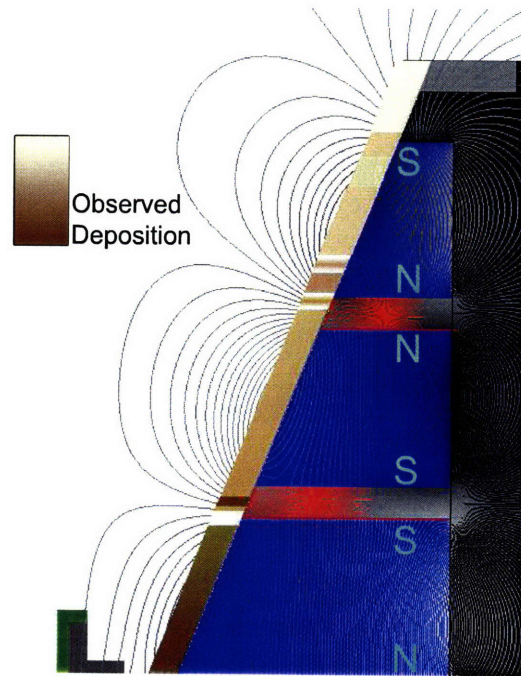
Figure 5-4: Sketch of the typical erosion patterns observed after firing the DCF thruster. Darker coloration along the channel walls indicates more deposition.

The effectiveness of the magnetic bottle near the anode in localizing the plasma away from the anode tip is inconclusive at this stage. As described in section 3.3.3, the original stainless steel anode was replaced with graphite to avoid damage to the anode and sputtering material influencing the thruster performance. Although the observed deposition did decrease significantly after the change, this modification did not address the fact that high energy ions were impacting the anode. It is typical for the local plasma potential near Hall thrusters to be greater than the anode itself[9], resulting in ions lost to the anode. However; lost ions represent a loss and are undesirable.

These observations are far from conclusive but do offer some additional insight into the thruster operating characteristics. Most importantly, the deposited material and visual appearance of the discharge plume on axis appear to support the goal of producing a thruster with reduced wall erosion through magnetic confinement of the plasma. Despite occasional rings of exposed boron nitride, it appears that material may deposit throughout the majority of the discharge channel without being removed through erosion. If the source of deposited material could be established and suppressed, the increased lifetime goals of
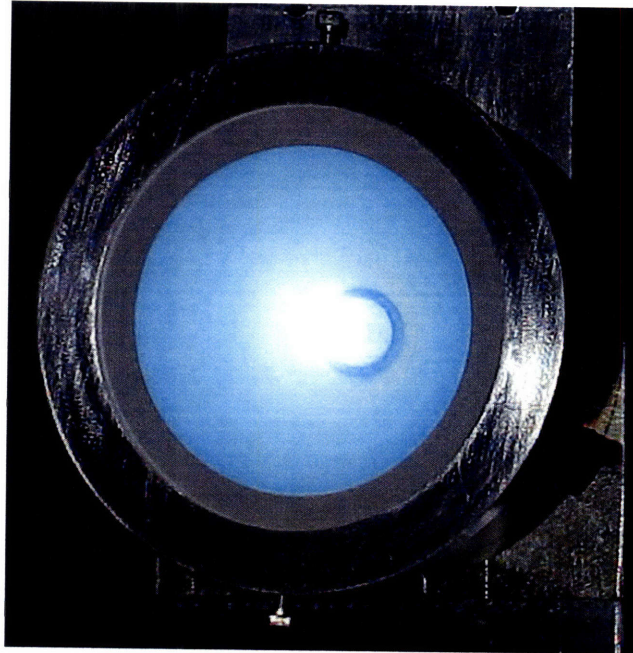
Figure 5-5: Photograph of discharge showing brightest regions of plasma separated from channel walls.

the thruster could be achieved simply be reinforcing the small focused erosion rings.

5.3 Relative Performance of the DCF Thruster

Comparisons between the MIT DCF thruster and traditional Hall thrusters are discussed, followed by a discussion of the performance relative to other cusped field thrusters. The nominal performance levels of a similar THALES HEMP thruster, the Busek BHT-200 Hall thruster and the MIT DCF are summarized in table 5.1.

Metric	THALES HEMP-T 3050[1]	Busek BHT-200[7]	MIT DCF
Anode Power, P_a	$1650W$	$200W$	$242W$
Xe Mass Flow, $\dot{m}_a$	$1.7mg/s$	$0.94mg/s$	$0.84mg/s$
Thrust, T	$50mN$	$12.8mN$	$13.4mN$
Specific Impulse, Isp	$3000s$	$1390s$	$1640s$
Anode Efficiency, η_t	45%	43.5%	44.5%

Table 5.1: Performance at nominal operating points of the THALES HEMP-T 3050 cusped field thruster, the Busek BHT-200 traditional Hall thruster and the MIT DCF thruster.

Comparison with Traditional Hall Thrusters

The peak anode efficiency of the MIT DCF prototype was $44.5 \pm 8\%$, while consuming $242W$ of anode power at $8.5sccm$ of Xenon flow and providing $13.4 \pm 1.2mN$ of thrust. The specific impulse at this nominal operating point was $1640 \pm 150s$. Referring to table 5.1, the nominal performance is comparable to that of the Busek, BHT-200 thruster. The MIT DCF also operated relatively well at lower power levels, with mean anode efficiencies above 25% at power levels as low as $100W$ and specific impulse above $880s$. Compared to existing low power Hall thrusters[12], this performance range suggests the DCF could be well suited for miniature thruster applications. It should be noted that although the current DCF prototype compares well with the BHT-200 and lower power thrusters, the present physical design make it significantly larger in physical size than those devices[12].

The beam profile of the BHT-200, a sample of which was shown in Fig. 4-2, is typical of traditional Hall thrusters. This differed greatly from the DCF profiles shown in section 4.3.2. The DCF conical shape is of concern given the relatively large angle of the ion peak current density, around 33°. However; further diagnostics of the plume are required before the beam divergence angles can be compared more rigourously, for example by comparing the angles which contain 95% of the plume. Although focused on the thruster axis, the

BHT-200 plume is wide and the measured divergence, as defined above, can be roughly 50° to 60°[6]. Thus, although the DCF pattern is currently a concern, the behavior at larger angles would be required in order to determine how well the beam is constrained to the conical shape. If the beam is focused and the angle could be reduced, the result could become a positive feature by creating a highly localized beam.

The relative erosion, and hence lifetime, characteristics require further study of the DCF. Although preliminary observations discussed in the previous section suggest the DCF thruster does confine the discharge away from the walls, a more rigorous study of the erosion rates and deposition sources should be conducted before drawing any further conclusions.

Comparison with other Cusped Field Thrusters

The most recent iterations of the THALES HEMP thrusters[1], introduced in section 2.2.1, have been optimized for higher power and specific impulse operation than the DCF prototype. Specifically, the HEMP-T 3050 nominal operating conditions are $50mN$ of thrust, requiring $1500W$ of anode power at an efficiency of 46%[1]. However, during initial phases of testing the performance of the THALES DM7 thruster (a prototype version of the 3050 model) was evaluated over a large range of flow rates and anode potentials[19]. The referenced thruster had a channel diameter of $22mm$, the dimensions were thus on the same order as the DCF thruster (with diameter increasing from $15mm$ at the base to $56mm$ at the exit plane).During those tests the anode efficiency rose sharply from roughly 15% at $V_a = 200V$ to 36% at $V_a = 600V$, with flow rates as low as $10sccm$. Therefore compared to the DCF, favorable performance at low powers was observed (refer to Fig. 3-16). Some reports of the THALES thruster plume indicate strong similarities with the conical discharge from the DCF[18, 19]. However the most recent iteration of the thruster has reportedly been modified to create a plume more typical of traditional Hall thruster[23] with 95% of the beam contained within an angle of roughly 55°.

The Princeton CHT thrusters, also introduced in section 2.2.1, have been primarily directed towards low power operation[15]. Several iterations have been developed with discharge channels between $20mm$ and $40mm$ in diameter[27]. These thrusters typically operate between $100W$ and $200W$ of anode power. Anode efficiencies between 20% and 30% have been reported, with lower efficiencies at lower powers. The DCF thus performs at or beyond the CHT in this respect, as efficiencies between 25% and 40% were observed over

the same input power ranges. CHT thrusters also suffered from significant beam divergence but recent improvements have reduced 95% of the beam to within 55°[27].

Both the CHT[27] and HEMP[18] thrusters are reported to have extended lifetimes over conventional Hall thrusters due to reduced wall erosion. To the authors knowledge, long life measurements of the wall erosion profiles (or rate) have not been performed by either group. However; erosion with iterations of the HEMP thrusters has been observed both visually and using spectroscopic analysis of the impurities levels in the plume. Both methods supported claims of minimal erosion[19]. The HEMP visual observations relied on observed deposition profiles similar to preliminary observations of the DCF erosion presented in the previous section. Again, no conclusive statements can be made regarding the DCF erosion properties compared with these thrusters.

5.4 Recommended Studies

The study presented here has been highly exploratory in nature and despite good performance, the physical processes within DCF thruster is far from understood. Clearly further testing and theoretical investigations are required.

5.4.1 Numerical Simulation

The complex magnetic structure within the DCF thruster lends itself to numerical simulation rather than analytic models. It was suggested in section 2.2 that the projected benefits towards wall erosion may be associated with modifications to the sheath structures within the cusps, a code which does resolve the sheaths would therefore be desirable. A hybrid PIC-Vlasov simulation code developed by Fox[42] at MIT thus appears ideal. Efforts are currently underway to apply this code to the DCF arrangement[43].

Simulation could provide some verification of the proposed plasma confinement properties and, hopefully provide insight into the divergent, but potentially well focused discharge observed in this study. Furthermore, simulation may provide further insight into the observed operating modes. Ideally simulations could be used as a means of optimizing the magnetic field structure, which is challenging and expensive experimentally when using permanent magnets. Similarly, the impact of the thruster divergence angle cannot practically be explored experimentally. Simulation may allow for optimization of the discharge channel divergence.

5.4.2 Physical Modifications

An interesting, yet simple alteration to the design would be to remove the third (downstream) magnet. Given the postulated explanation for mode transitions, the necessity for the upper magnet is not clear. If the plasma is confined near the anode and the first cusp, then a strong upper cusp (between the second and third magnet) may not be necessary. Hence if a non magnetic shunt is put in place of the final magnet with little impact on performance, the thruster dimensions could be reduced significantly. Regardless of the ability of the magnetic fields to reduce electron transport to the walls, removing unnecessary walls would always be preferred. Erosion observations already suggest that the plasma is impacting the walls at the downstream exit plane, so if the discharge channel could be short-

ened it may reduce losses and enhance lifetime. Also, one motivation for the downstream field structure, magnetization of ions, may not be as significant as initially thought which further reduces the need for a downstream magnet. However, such a modification could reduce performance in the first, high current, operating mode. Here, as described in section 5.1, some of the plasma could be confined within the downstream region of the thruster (referred to as C2 in that discussion) where the field structure is strongly influenced by the third magnet.

In addition, some more practical modifications should be made. The thruster mass may be reduced significantly through eliminating the thick casing walls and reducing the base core size. The graphite anode was effective but is fragile. A graphite tipped structure would allow for both reduced sputtering at the tip and a robust structure. The porous diffuser size should be minimized and welded to the base core to further reduce arcing problems like those seen at Busek (section 3.2.3). A second prototype of the thruster with identical magnetic structure has been developed by students at MIT with these concepts in mind[44]. The base core was modified to reduce overall mass while minimizing any effect to the internal magnetic structure. In addition the thruster includes a new, larger anode. Preliminary testing of this second DCF had just begun at the time of writing this report. Although no thrust or plume measurements have been made, the thruster has operated stably at power levels as low as $50W$.

5.4.3 Experimental Studies

Thrust measurements and diagnostics of the plume should be completed more rigorously over a range of operating parameters. A larger test matrix of flow rates and input powers would be useful to ensure that nominal operating conditions have been found and the general performance trends are understood. Such a study should include reviews of the mode transition points and repeatability.

More in-depth diagnostics of the internal plume would be extremely useful, both to validate simulation and understand the internal structure. Particularly, measurements of the potential profile within the thruster would be extremely useful.

The cathode location clearly had an impact on the thruster performance in section 3.2. However; once the cathode was moved to position C and the discharge stabilized it was not moved again. A parametric study of the impact of cathode location on thruster performance

would be useful to to both optimize the performance and understand the phenomenon.

Similarly, the location of the anode has not been optimized. No direct verification of its impact has been observed to date. As mentioned previously, although replacing the stainless steel anode with graphite reduced erosion, the high energy ion impacts are not desirable. Again, a parametric study of the relationship between anode location, performance and, ideally, anode sputtering should be performed. The ideal location would be one which demonstrates both good performance and long life.

Optical studies of the thruster plume could provide a wealth of information. For example, measurements of the Doppler shifted ion emission lines could provide information about the ion velocities at various positions within the plume. Furthermore, previous studies of cusped field thrusters have reported significant populations of doubly charged ions[19]. This could be investigated by looking for emission lines from doubly charged xenon in the plume.

Finally, the anode current drifts which were presumed to be caused by thermal issues with the magnets (see section 5.2.1) should be explored. This could be accomplished through both long duration studies to determine steady state operating characteristics and by attempting to measure magnet temperatures at each operating point. If it can be confirmed that the drifting current is a thermal effect, then efforts to improve the thermal design should be made.

5.5 Conclusion

The prototype MIT DCF thruster presented in this study has performed at levels comparable with both traditional Hall thrusters and other cusped field plasma thrusters. The thruster has therefore demonstrated that a cusped magnetic field configuration is a legitimate competitor to the more traditional Hall thruster arrangement. Preliminary signs of reduced wall erosion have been observed which could suggest longer lifetime operation than comparable Hall thrusters. The thruster operated at a peak efficiency of 44.5%, producing $13.4mN$ of thruster with a specific impulse of $1640s$ requiring $242W$ of input power.

Several interesting phenomena have been observed. In section 3.2.1, the cathode plume was observed to couple to magnetic flux lines outside the thruster discharge, a visible path to the thruster discharge chamber was observed. The thruster behavior was observed to depend significantly on the location of the cathode in section 3.2.2. Two modes of operation characterized by a significant drop in anode current and a visual transition in the plume were observed throughout the test campaign. Despite the variations, the anode efficiency did not appear to vary greatly, see sections 3.2.3 and 4.4. In section 4.4 preliminary results were shown which suggest that this transition is accompanied by a shift to low utilization efficiency but more uniform ion acceleration through near anode potentials. A simple explanation for the transition was proposed in section 5.1 but no indisputable conclusion could be made to explain the bi-modal operation. Finally, the thruster plume was observed to be conical with a hollow core in section 4.3.2. This shape differs greatly from the plume profiles observed from traditional Hall thrusters.

Chapter 6

LaB_6 Hollow Cathode Development

6.1 Introduction

Electrostatic propulsive units, including Hall thrusters and ion engines, require cathodes for two reasons. First, electrons are required to provide ionizing electrons within the thruster. Second, the emitted beam of positively charged ions represents a net current flow from the spacecraft. The subsequent charging of the spacecraft would quickly nullify any propulsive thrust by neutralizing the ion accelerating potential. As a result, an electron current, equal in magnitude to the beam current is required to maintain a quasi-neutral beam.

Cathodes are therefore a inescapable requirement in electrostatic propulsion and their operating characteristics can have major impacts on the overall efficiency of a propulsive unit. Their impact becomes increasingly pronounced when applied to low power Hall thrusters. For example, consider a $200W$ Hall thruster, capable of producing $10mN$ with $8sccm$ of anode flow. Ignoring the cathode requirements, the resultant anode efficiency given by equation 2.2, is 31.2%. However, a typical hollow cathode, for example the Busek hollow cathode used with the DCF, may require an additional $1sccm$ of flow and often, at such low powers, a continuous supply of around $10W$ to the keeper circuit. When the cathode flow and power are considered in equation 2.5, the overall efficiency is reduced to 26.4%. It is clear from this simply example that measures to reduce cathode flow and power requirements must be considered when developing a complete system.

6.2 Hollow Cathode Review

The most frequently employed cathode neutralizers for electrostatic thrusters are the hollow cathode type. The section offers a brief overview of the basic principles, and operating regimes of hollow cathodes.

6.2.1 Thermionic Emission

An understanding of hollow cathodes follows from considering the evolution from a simple hot wire cathode to the complete assembly. When a material is sufficiently heated it will emit a current density, j given by the well known relation for thermionic emission,

$$j = A^* T_w^2 e^{-\frac{e\phi}{kT_w}}. \tag{6.1}$$

Here $A^* = 120 A cm^{-2} K^{-2}$ is the Richardson constant constant[45], T_w is the surface temperature in $^\circ K$, ϕ is the work function in eV and k is Boltzman's constant. We can therefore hypothesize a simple cathode as in Figure 6-1. In the figure, current is pumped through a wire with a relatively low work function. If sufficient current is pumped through the wire, its temperature will rise through Ohmic heating and, once sufficiently heated, an additional current given by equation 6.1 could be extracted.

Hollow cathodes rely on the same principles as the example above but with some significant enhancements. Consider a surface in a plasma, as in Figure 6-2. In order to balance electron and ion currents to the surface, a sheath region develops. The result is a potential distribution as shown in the figure. Note the reversal of potential curvature approaching the wall. This behavior is frequently referred to as a double sheath[46], and is characteristic of the potential near hollow cathode insert walls. The double sheath forms due to the presence of thermally emitted electrons near the wall, causing a build up of negative charge. At low plasma densities the current emitted by the insert may become space charge limited as the electric field near the insert approaches zero[47]. Naturally this condition must be avoided when designing hollow cathodes.

Notice that a non zero electric field, E_w will develop at the wall[48], this field can enhance electron emission as represented by the Schottky equation,

$$j = \alpha T_w^2 e^{-\frac{e(\phi - \phi_{sh})}{kT_w}}. \tag{6.2}$$
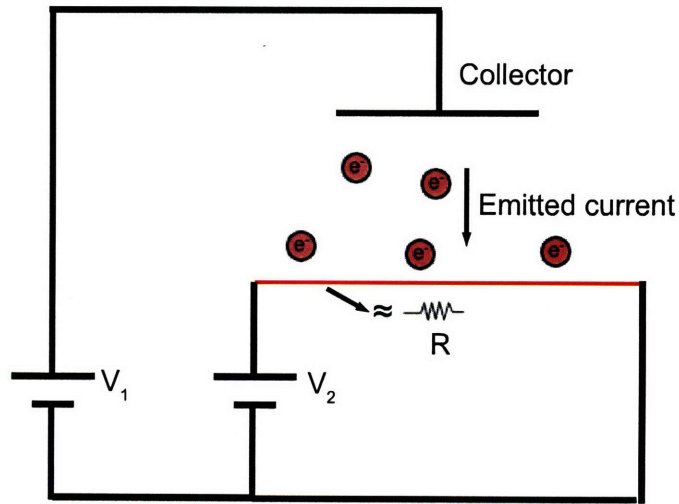
Figure 6-1: A basic hot wire cathode and collector.

Where ϕ_{sh} is related to the field strength at the surface by,

$$\phi_{sh} = \sqrt{\frac{eE_w}{4\pi\epsilon_0}}.$$ (6.3)

However, for the estimates made during this project the Schottky effects have been ignored (the estimated current is therefore more conservative).

The benefits of this arrangement become clear when one considers the case where the plasma density (ϕ_0 in Fig. 6-2) approaches, ϕ_i, the ionization energy for the working gas. In this case, electrons extracted through the sheath, may ionize neutral particles and serve to maintain a quasi-neutral plasma even as electrons are lost elsewhere in the plasma. Hollow cathodes maintain a plasma density sufficient to create such sheaths while extracting excess electrons. These extracted electrons then form the discharge current to be used for ionization and neutralization in thrusters as described previously.

The most common manifestation of this concept is through a cylindrical arrangement, as in Figure 6-3. Here neutrals are ionized while passing through a cylindrical emitting surface
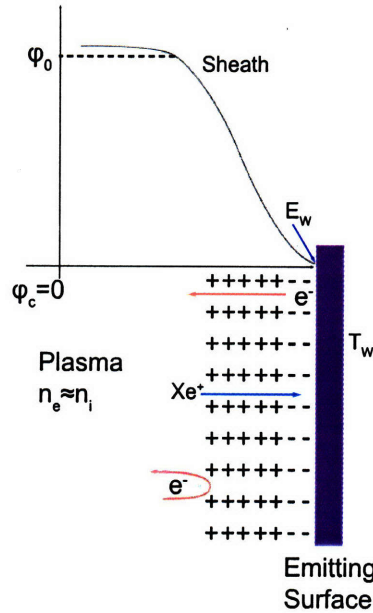
Figure 6-2: An emitting surface in a plasma.

and the resultant plasma plume flows through an orifice downstream. In order to maintain the plasma within the tube, the emitting surface must be maintained at a temperature sufficient for thermionic emission. The presence of a sheath becomes increasingly beneficial when considering this requirement. As electrons are accelerated from the emitting surface into the plasma, ions will be accelerated towards the emitter walls. Although this represents a significant source of erosion, some of the ion energy is transferred to the surface in the form of heat. Thus providing a mechanism for self sustained heating of the device.

Consider a fixed current being extracted from the arrangement. If the electron flux from the plasma out of the cathode tube is less than that being emitted from the surface, the internal electron density will begin to increase. In response, the sheath potential will decrease in order to balance the thermal electron flux towards the sheath with the emitted current from the surface. This decreases the energy of ions accelerating towards the surface, thereby decreasing its temperature and hence thermionic emission. Thus, equilibrium between thermionic emission and internal electron flux can be established. Conversely if the flux emitted from the cathode is too high, the plasma potential would rise extract more electrons from the emitting surface and maintain equilibrium.

In addition to wall heating by collisions, another potentially advantageous result of the

hollow cathode arrangement is that the majority of radiated energy will be absorbed by the insert walls in the form of heat.

6.2.2 Complete Hollow Cathode Arrangement

In order to sustain emission from a hollow cathode, a positive electrode, known as the keeper, is frequently arranged as in Fig. 6-3. When a positive potential, greater than the internal plasma potential, is applied with respect to the cathode tube, electrons which exit the cathode orifice will be accelerated towards the keeper. The purpose of the keeper is to facilitate the extraction of a quasi-neutral plasma through which a net electron current may flow. When, for example, operated with a Hall thruster the cathode plasma plume couples to the thruster beam downstream. The result is a path for electrons to enter the thruster plasma for both beam neutralization and ionization within the thruster discharge channel.
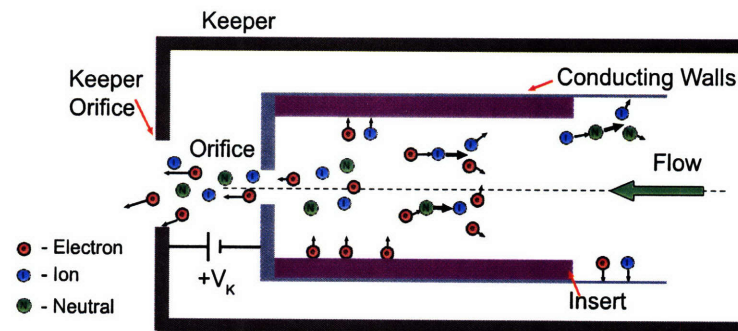
Figure 6-3: Basic hollow cathode arrangement with keeper. A net electron current is extracted through the emitted plasma plume downstream of the emitter surface.

Ideally, the keeper should only be used when starting the cathode, and when the thruster (or other surface) is not active. When starting cathodes, no plasma exists and the emitting surface must be externally heated to create thermionic emission. The keeper is then used to create a potential drop within the insert region through which emitted electrons may be accelerated to energies sufficient for propellant ionization. For xenon, this requires ~ 10 to $15eV$ when one considers ionization by multiple collisions[49, 50]. Once a plasma begins to form, the thermionic electron emission will increase through the mechanisms described above thus sustaining the plasma. The keeper then serves extract a net current,
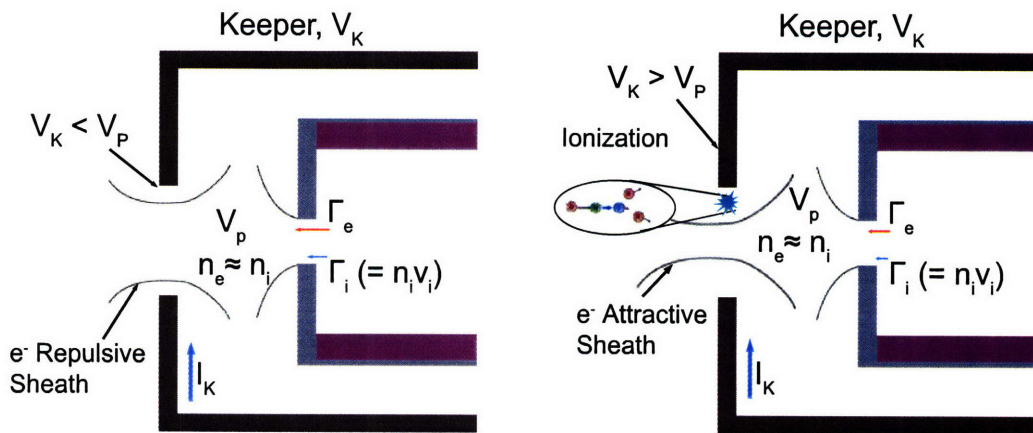
(a) Spot mode operation, here passive collection of the current is obtained.

(b) Plume mode operation shown electron attracting sheaths. The sheaths are drawn larger than in the spot mode diagram above due to the decreased density in plume mode.

Figure 6-4: Sketches of spot and plume modes in the case where only the keeper is used to collect electron current.

thus keeping the plasma potential sufficiently above the insert potential for self heating to occur. However, with a thruster operating nearby the required potential to maintain current emission can be provided by the difference between the beam and cathode potentials directly. This voltage, referred to as the cathode discharge potential, ideally eliminates the need for the keeper while operating a thruster. With the keeper circuit opened, the keeper will collect some electrons and float near (but below) the local plasma potential. Most of the plasma electrons will then flow to the external anode, be it an engine's ion beam or a biased plate. However, in some cases the keeper may be run continuously in order to promote the discharge and ensure that the total emission current, and hence power deposited in the cathode, is sufficient to maintain the temperatures required for emission.

6.2.3 Plume and Spot Mode Operation

The connection between keeper, or external anode, conditions and the cathode processes are not as simple as may have been inferred from the description to this point. Of great importance in characterizing and operating hollow cathodes is the transition between the so called "spot" and "plume" modes.

During spot mode operation the plasma emitted from the orifice has charged particle

densities sufficient for the desired amount of current to be collected at the keeper or anode relatively passively. This situation is depicted in figure 6-4(a). Spot mode occurs at high flow rates or high currents where the plasma flux from the orifice is sufficient to maintain a quasi-neutral plasma throughout the cathode plume with small sheaths developing near the anode or keeper surfaces. Here the passive plasma currents collected by the keeper and anode are sufficient, or in excess of, the net current to be extracted. When the passive current exceeds the desired current, electron repelling sheaths can be expected. As flow rates increase further, little variation in the anode and keeper potentials are observed while maintaining a fixed current[49].

Alternatively at low currents or low flow rates, the passive flux to the anode and keeper are no longer sufficient to collect the desired current. As a result, electron attracting sheaths develop to enhance the collected current at the keeper and anode surfaces. Simultaneously, the sheath thickness increases, which diverts more electrons to the keeper and blocks the passage of ions towards the outside collector. From an operational point of view, where a specified current is desired, the required anode and keeper voltages begin to increase. As the plasma density continues to decrease, at lower flow rates, the keeper and anode potentials increase further. In this state, the cathode is said to be in plume mode as the electron attracting sheaths can result in high energy electrons which cause ionization of neutrals. The result being a bright visual plume emitted from the cathode. This condition is characterized by large anode and keeper potentials and also by large oscillations in the voltage required to maintain desired currents [51]. In addition, the low densities during plume mode have been shown to support increased electron temperatures through reducing collisions within the plume[52]. Beyond the obvious drawback of plume mode, high potentials, it has been noted that ions repelled by the keeper or anode may be accelerated back towards the cathode surfaces and could cause significant damage through sputtering[49].

6.2.4 Hollow Cathode Plasmas

A brief review of experimentally observed plasma conditions within hollow cathodes may be useful in understanding the overall device. For details and in depth results the reader should consult the references[48, 53]. Typical forms of the axial plasma potential and densities within typical hollow cathodes are sketched in Figure 6-5. The potential rises sharply at the cathode and keeper orifices. The plasma density profile will vary with the

105
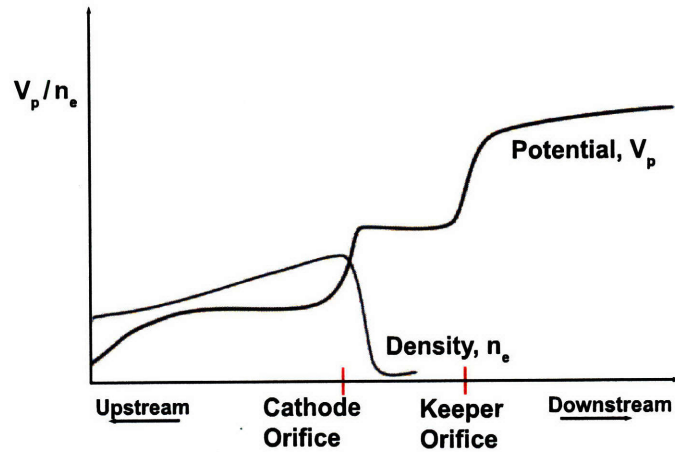
Figure 6-5: Sketch of typical axial potential and plasma density variations moving through a hollow cathode.

cathode design. Sharp density peaks near the orifice are desirable for cathodes which rely on orifice plate heating, see section 6.4.2. Otherwise, a more uniform density distribution (as in the figure) is desirable. As found experimentally[53] and theoretically[48] , plasma densities can often be on the order of $10^{20} m^{-3}$. The internal neutral pressures are typically on the order of a few $Torr$ and electron temperatures, measured along the central axis can be a few eV.

6.3 LaB_6 as a Hollow Cathode Emitting Surface

Many electrostatic thrusters use barium oxide (BaO) impregnated tungsten (W) hollow cathodes for both in space and laboratory use. However; lanthanum hexaboride (LaB_6) has a number of advantages, particularly when used in laboratory settings. This section reviews the tradeoffs between LaB_6 and more common insert materials, and reviews the benefits of using LaB_6 when fulfilling the cathode requirements of MIT Space Propulsion Laboratory.

6.3.1 Insert Material Comparison

The most common forms of hollow cathodes use some variety of tungsten with a supply of barium and oxygen. Pure tungsten has a work function of approximately $4.55eV$[54]. However, if a barium oxide substrate is developed on the emitting surface, as in Figure 6-6, the work function is reduced to approximately $1.7eV$[51]. Such a low work function makes this type of material extremely attractive for use in hollow cathodes.

Methods of forming the BaO layer include impregnating a porous tungsten bulk with barium rich compounds and catalysts, as in the figure, or by creating a "reservoir" supply of barium and oxygen external to a porous tungsten insert[55]. Specifically, a common arrangement uses porous tungsten with barium oxide, aluminum oxide (Al_2O_3) and calcium oxide (CaO) impregnates in a $4 : 1 : 1$ molar ratio[49]. Cathodes using barium oxide layers to reduce the work function will henceforth be referred to as $BaO - W$ type cathodes. Several drawbacks are inherent in the $BaO - W$ type arrangement. The BaO layer is extremely sensitive to impurity poisoning at high temperatures[55]. As a result, extreme care must be taken when operating the cathodes, including using ultra high purity xenon (or other propellants). In addition, the requirement for a BaO layer to continuously form at the emitting surface, while also being lost through evaporation into the insert region, restricts the cathode lifetime by limiting the supply of impregnates.

Lanthanum hexaboride (LaB_6) has a bulk work function of approximately $2.7eV$[51]. Since the bulk material is emitting, no chemical processes are required, as depicted in Figure 6-7. Predicted emitted current densities, as given by equation 6.1 of section 6.2, for pure tungsten, $BaO - W$ and LaB_6 are plotted in Figure 6-8. As detailed by Goebel[51], LaB_6 has significant advantages over $BaO - W$ both in terms of evaporation rates and impurity
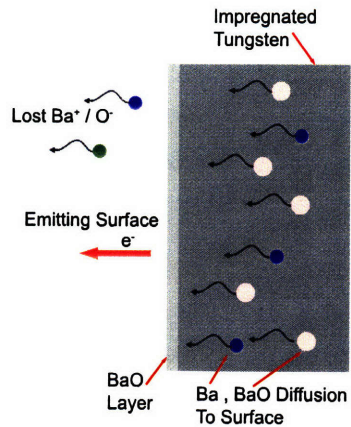
Figure 6-6: Simplified representation of the processes within BaO-W type emitting surfaces.

poisoning. Specifically, LaB_6 inserts are only weakly affected by oxygen as partial pressures exceed $10^{-4}Torr$ and virtually insensitive to water vapor. Meanwhile, $BaO - W$ emission decays rapidly above oxygen and water partial pressures of approximately $5 \times 10^{-7}Torr$ and $5 \times 10^{-6}Torr$ respectively. In addition, at current densities up to approximately $10A/cm^2$, LaB_6 erodes at a rate substantially lower than some $Ba0 - W$ cathodes, see [51] for details.
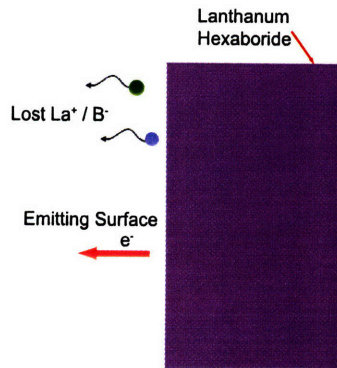
Figure 6-7: Simplified representation of the processes within LaB_6 type emitting surfaces.

Practically, a significant advantage of LaB_6 cathodes over $BaO - W$ lies in the time required to begin emission. When using $BaO - W$ cathodes, a lengthy conditioning time, on the order of a few hours, is required to slowly heat up the cathode at such a rate

108

where unwanted impurities can escape while the BaO layer forms, thus preventing cathode poisoning. In a laboratory setting, this conditioning time is a major concern and frequent source of delay when performing and scheduling experiments. Using a LaB_6 emitter, the only concerns when pre-heating the cathode lie in ensuring heating is performed at a rate slow enough to reduce thermal shock and to ensure uniform temperatures at the emitting surface during ignition.

In summary, some key advantages of LaB_6 cathodes compared with $BaO-W$ type cathodes are that they can be conditioned very quickly, can be exposed to some gas impurities with limited effect on performance[51] and do not require a supply of diffusing substances to continue operating efficiently.

However, the high work function of LaB_6 is a major drawback. As shown in Fig. 6-8, the temperature required to emit a given current density is significantly higher for LaB_6 than $Ba0-W$. Due to the high temperatures required, developing a heater to reach ignition temperatures and efficiently reducing heat losses during operation are significant challenges for LaB_6 cathodes. See section 6.4.4 for details of the design used here. In addition, LaB_6 is prone to react with many refractory metals (eg. Tungsten, Tantalum...) at high temperatures[51]. Material compatibility is therefore a concern when developing a design.
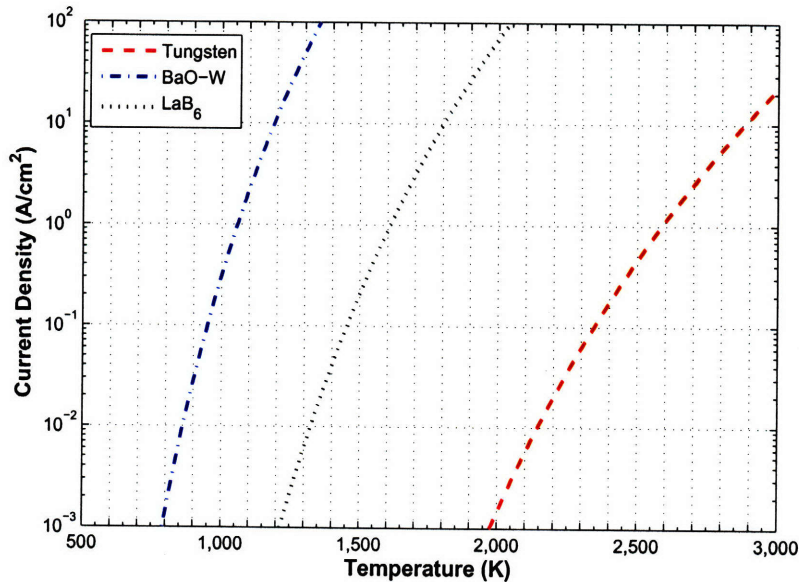
Figure 6-8: Emission currents as predicted by equation 6-8.

6.3.2 Cathode Requirements of the MIT Space Propulsion Laboratory

The MIT Space Propulsion Laboratory, at the time of this project, primarily required hollow cathodes for low power plasma thrusters. These include the DCF thruster, the BHT-200[7] Hall thruster and others. The cathode must therefore provide discharge currents between roughly $0.3A$ and $2.0A$. In order to maximize overall propulsive efficiency (ie, efficiency accounting for cathode power and flow consumption, refer to section 2.1.1), a cathode capable of operating with minimal external heating, coupling voltages and flow rates within the desired current range was the goal of this project.

As a point of comparison, the Busek $BaO - W$ hollow cathode, which was used when collecting the data presented in chapters 3 and 4, nominally requires an active keeper circuit collecting $0.5A$ through roughly $20V$ between the cathode tube and keeper at a flow rate of $1sccm$. At identical currents higher voltages are expected when using LaB_6 due to the larger work function. Nevertheless, the performance levels of the Busek cathode establish a design target, and benchmark for comparison with the LaB_6 cathode developed here.

6.3.3 Available LaB_6 Insert

At the beginning of this project two identical LaB_6 inserts were available measuring $7.11mm$ in length, with inner and outer diameters of $1.31mm$ and $3.0mm$ respectively. The resulting, initial emitting area was therefore approximately $0.29cm^2$. In order to meet the current requirements discussed above a maximum emitting current density of approximately $7A/cm^2$ would be required. Referring to Fig. 6-8, the emitter temperature would be approximately $1500°C$ at such a current density. As will be discussed in following section, this high temperature presented significant challenges when determining design materials and in ensuring an efficient hollow cathode design.

Figure 6-9: One of the LaB_6 inserts used in developing the hollow cathode presented here.

6.4 LaB_6 Hollow Cathode Design
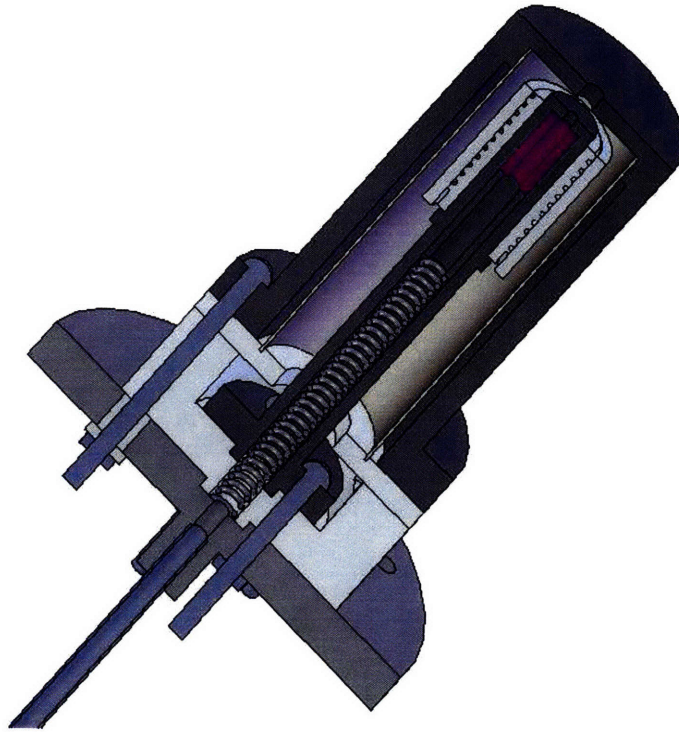
Figure 6-10: CAD drawing of the assembled cathode. Detailed drawings of each component, and the complete assembly are presented in appendix B

The cathode designed for this project was based on the LaB_6 cathodes developed at NASA JPL[51], largely for high current applications. The details presented here are an overview of the attempts to modify the design for efficient, low current applications.

The basic design, as developed by JPL and including some application specific modifications, is summarized by Figures 6-10 and 6-11. The figures are to scale and includes all components except for the heater circuit wires and a thermocouple used during some stages of the characterization. For detailed engineering drawings and notes from the machining processes refer to appendix B.

As shown in the figure, the emitting insert is housed within a graphite tube while the heater, keeper and base structures make up the complete assembly. The steps and rational behind the design of each of these components, along with features aimed at reducing thermal losses are discussed in the following sections.

Interior Parts:

LaB$_6$ Insert

Threaded Heater

Heater Sheath

Cathode Tube

Graphite shunt

Retention Spring

Exterior Parts:

Keeper tube

Tantalum heat shield

Alumina spacer/cap

Alumina Insulator

Base

40 mm
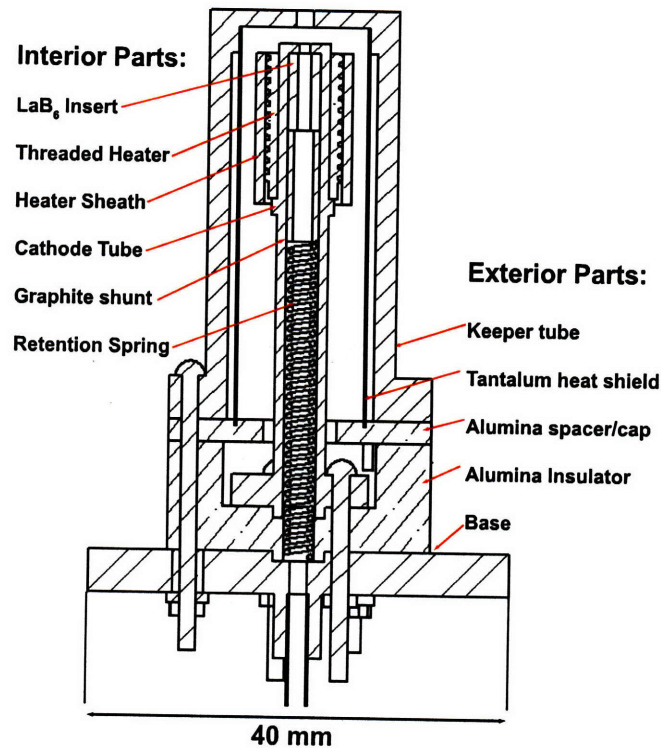
Figure 6-11: Schematic overview of the assembled LaB_6 cathode. Primary components are indicated and are described in detail during this section.

A common set of materials were used throughout the design and, as a summary, their basic properties and grades (if applicable) are presented in table 6.1. The specific qualities considered when selecting each material will be discussed in the relevant sections.

6.4.1   Primary Cathode Tube

The primary cathode tube was machined from a single piece of iso-molded Poco graphite (see table 6.1). In order to reduce conductive heat losses, a long, thin tube was desired. In this respect, the design was restricted by available machining equipment. The final tube length was $44mm$ long with a $1mm$ wall thickness and an ID of $3.0mm$ equal to the LaB_6 insert OD. The tube flange diameter and thickness were both kept to a minimum while allowing space for assembly screws. See appendix B for complete dimensions and engineering drawings.

113

Material	Thermal Expansion Coefficient ($\mu m/mK$)	Thermal Conductivity (W/mK)	Emissivity	Grade/Supplier
Graphite	7.9	95	0.7	AXF-5Q/Poco Graphite[40]
Boron Nitride (BN)	$\parallel$2.95 ($\perp$0.87)[†]	$\parallel$27.0 ($\perp$29.0)[†]	0.9	HP/Saint-Gobain[5]
Alumina (Al_2O_3)	7.74	4.6	0.9	960/Cotronics Corp.[56]
Tantalum	6.5	54.4	0.2	Alfa Aesar[57]
Tungsten	4.6	167	0.3	Alfa Aesar[57]

Table 6.1: Summary of materials used throughout cathode design process. [†] The boron nitride used had properties parallel ($\parallel$) and perpendicular ($\perp$) to the pressing direction as indicated.

Due to variations in expected thermal expansion between components, and a desire to keep the LaB_6 insert firmly held against the tip of the cathode tube, a spring was required inside the assembly. Tungsten was deemed suitable due to its high melting temperature; however, as discussed in section 6.4.1, LaB_6 is not compatible with tungsten at high temperatures. In order to prevent direct contact, a small graphite shunt $10.4mm$ in length was used as a buffer between the emitting insert and the spring. The shunt, spring and cathode tube are shown in Figure 6-12.

Necessary electrical connections were maintained to the cathode tube though three mounting screws and the tungsten retaining spring, all of which were in physical contact with the base structure (local ground).

6.4.2 Orifice Design

The hollow cathode orifice design can have a significant impact on overall performance and has been the subject of numerous studies [58, 59]. The orifice represents a means of controlling the plasma within the primary tube through internal pressure and temperature. As a result, the ideal orifice allows for spot mode operation with minimal flow and power consumption. The frequently referenced Kaufman scaling criterion[58] is appealing as it predicts a simple relationship between the orifice diameter, the propellant gas atomic weight and the flow rate. However, the criterion does not prove effective at establishing a minimum flow rate in practice[50]. Instead of using such a relation, the approach taken during this project was to consider variations to the orifice geometry, as summarized in Figure 6-13, more generally and apply known experimental results to complete the design.
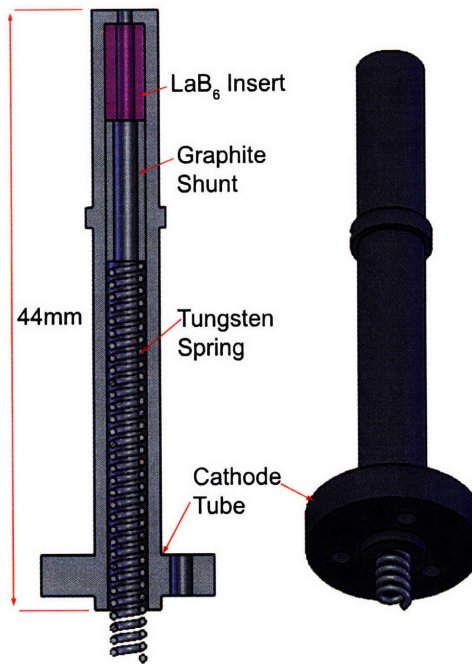
Figure 6-12: Cathode tube assembly showing retention spring, graphite shunt and LaB_6 insert.

If the orifice becomes too large, the plasma density within the emitter region may not be sufficient to prevent space charge limited emission from the insert, as described in section 6.2.1. With a small orifice, a high density, high temperature plasma can be present facilitating significant ion losses to the walls, and decreased conductance through collisions[60]. In some cases, heating and collisions within the orifice region have been suggested as a primary method of maintaining proper surface temperatures for emission from the insert[60]. However, this can result in a plasma density distribution that produces disproportional heating of the region near the orifice, and hence uneven emission along the insert which could lead to reduced lifetime[53]. As a result, a trade off between scaling of the orifice to maintain optimal neutral density within the tube while also generating a minimal power loss within the orifice plasma must be made.

Internal Pressure

The neutral flow pressure within the insert region will directly impact the plasma density. Referring to experimental measurements of internal pressures within well developed

115
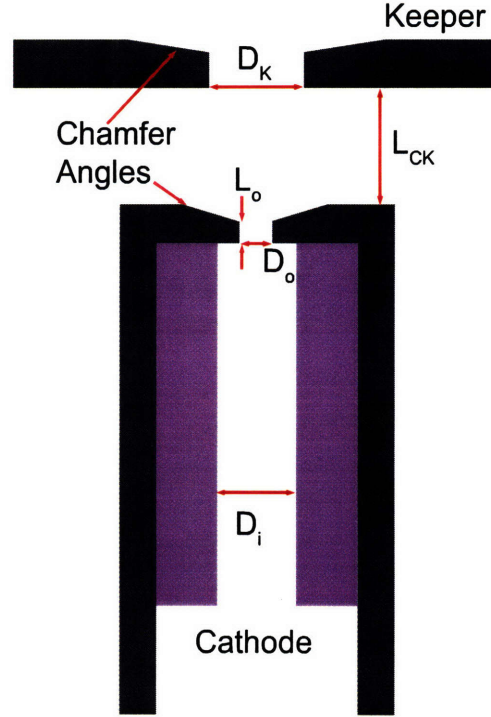
Figure 6-13: Geometrical parameters affecting hollow cathode design.

$BaO - W$ cathodes[53], at low flows, pressures around $\sim 0.3 Torr$ are common. However, in LaB_6 hollow cathodes, internal pressures of a few $Torr$ have been recommended to ensure relatively uniform heating of the insert while also yielding plasma densities sufficient to prevent plume mode operation, or even space charge limited emission[50] at low densities.

Given that the pressure downstream of the cathode orifice will be significantly lower than the upstream pressure, it is reasonable to assume that the flow will be choked at the exit. Assuming a roughly parabolic flow profile has evolved along the orifice tube, the pressure at this choking condition can then be expressed as a function of the flow rate $\dot{m}$, the orifice diameter D_o and the neutral temperature T as in equation 6.4.

$$P_e = \sqrt{\frac{64 \dot{m}^2 R_g T}{3 \pi^2 D^4}} \tag{6.4}$$

In equation 6.4, R_g is the specific gas constant for xenon ($63.5 J/kgK$). The internal pressure P_i within the insert region can be estimated by the stagnation pressure, assuming isothermal

inviscid flow upstream of the orifice exit plane, given by equation 6.5.

$$P_i \approx P_o \approx P_e e^{3/8} \tag{6.5}$$

In the equation, the factor 3/8 is a consequence of the assumed parabolic profile in contrast to a factor of 1/2 when uniform flow is assumed. From a design perspective, a relationship between orifice diameter, flow rate and internal pressures is desired. Combining equations 6.4 and 6.5, the orifice diameter can be expressed by equation 6.6.

$$D_o = 2 \left(\frac{4 R_g T}{3} \right)^{1/4} \sqrt{\frac{\dot{m} e^{3/8}}{\pi P_o}} \tag{6.6}$$

The flow temperature is unknown but can be assumed to be similar to the wall temperatures required for emission. Figure 6-14 shows the relationship between orifice diameter and neutral flow rate as given by equation 6.6, assuming neutral temperatures of $T = 1700K$. As stated in section 6.3.2, a cathode capable of operating efficiently at close to $1sccm$
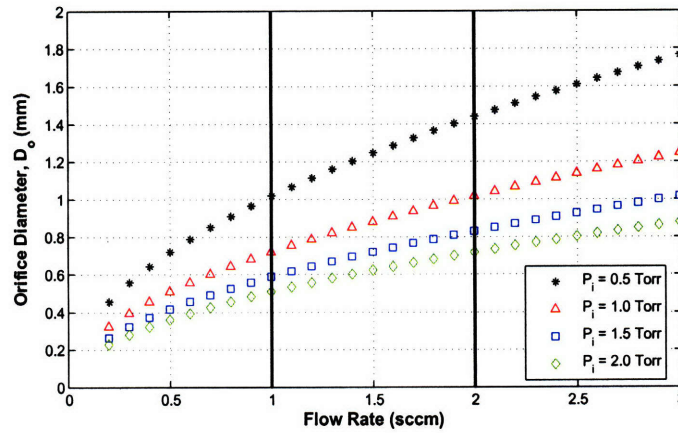
Figure 6-14: Diameter and flow rate relations predicted to result in the indicated insert pressures by equation 6.6. The neutral temperature was assumed to be roughly $1700K$, or approximately the insert wall temperature during emission.

was desirable. According to Fig. 6-14 an insert diameter of $1.0mm$ may be adequate for internal pressures between roughly $0.5Torr$ and $1.0Torr$. The pressure would hence be slightly higher than in the cited $BaO - W$ type cathodes while still on the order of the pressures recommended for LaB_6 cathodes.

Compared with hollow cathodes optimized for similar discharge currents [59, 61, 49] an orifice diameter $1.0mm$ is quite large. However, given that the cathodes in the references were of the $BaO - W$ kind, we elected to design towards the recommended pressures. The insert, described in section 6.4.1 is therefore only 1.3 times D_o, making the constriction from insert to orifice region much smaller than many of the referenced designs, where D_i can be as much as an order of magnitude larger than the orifice diameter. Furthermore, for orifice lengths on the order of a few insert diameters, we do not expect the length to have a significant impact on the internal pressure. Hence, the orifice diameter may be the primary factor influencing spot to plume mode transitions.

Orifice Aspect Ratio

The aspect ratio of the orifice, defined as $AR = L_o/D_o$ has been the subject of significant review [59] as an important parameter when designing hollow cathodes. For a simple insight into the relative importance of the orifice length, consider the desired condition of spot mode operation at minimal power. Spot to plume mode transitions occur when the density of plasma emerging from the orifice falls below that required to maintain current extraction from a quasi neutral plasma downstream. Since the orifice region is not emitting, the discharge current is simply drawn through the orifice plasma, which has some finite conductivity, σ. The power, W_o deposited through this process can be written,

$$W_o = \frac{L_o I^2}{\sigma \pi D_o^2}.$$ (6.7)

Therefore reductions in orifice length may be effective at reducing lost power with limited variation to spot mode transition flow rates, particularly in the case were the orifice length is comparable to the diameter. As a result, a relatively low aspect ratio, $AR = 0.5$ was initially selected. This can be compared with similar BaO cathodes where aspect ratios between 1 and 6 are common[49].

Finally, as shown in Fig. 6-13, a chamfer angle has been included in the orifice geometry. This angle was primarily included due to concerns in manufacturing. Specifically, requiring the entire upper surface of the cathode tube to have a thickness equal to the orifice length of $0.5mm$ was deemed impractical.

6.4.3 Cathode Keeper

The keeper electrode was described in section 6.2.2. Although both open and closed keepers can be used, referring to Figs. 6-10 and 6-11, the keeper employed here is the closed type as it also forms the enclosure which houses the cathode assembly.

With the external anode deactivated, the keeper is the sole collector of emitted current from the cathode tube. The key geometrical factors within the keeper are the orifice diameter D_K and the cathode to keeper distance L_{CK} both shown in Fig. 6-13. Qualitatively it is clear that both factors will influence the current collected for a given current density available from the orifice tube by varying the interception area, and hence should directly influence spot mode transitions when the keeper is collecting the discharge current. Similarly, a small orifice could prevent plasma flow out of the cathode, particularly at low densities where the sheath thickness increase in size. Despite experimental indications that variations in the keeper orifice may have a significant impact on the spot to plume mode transitions[51], no parametric studies of keeper geometries were known to the author. As a result the ratio of keeper orifice to cathode orifice diameters, D_K/D_o of 1.7 used by NASA JPL LaB_6 cathodes[53] was employed here. Similarly, limited studies concerning the cathode to keeper gap for small hollow cathodes were available. However, it is clear that as the gap is reduced the effective area of the current collecting surface of the keeper will also be reduced (essentially reaching a minimum when the keeper touches the cathode tube).
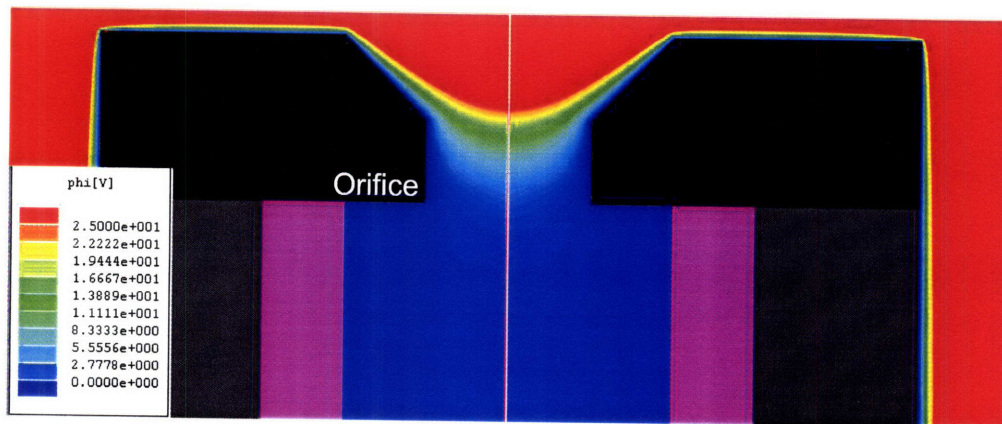
Figure 6-15: Simulated vacuum potential distribution at the cathode tip with 600V applied between the keeper and cathode (ground).

The internal plasma must be initiated by energetic electrons colliding with neutrals

within the cathode. In order to facilitate these ionizations, a potential on the order of the ionization potential must be present in the vicinity of the emitter region near the orifice. The electrostatic potential field, in a vacuum, was modeled using the Maxwell SV software[31] previously applied to magnetic fields within the DCF thruster in section 2.3.2. Although the potential distribution would change significantly once a plasma forms, the vacuum model was assumed to be a reasonable approximation prior to ignition. The results in Figure 6-15, show that for $L_{CK} = 2.0mm$ the potential near the orifice upstream entrance approaches $10V$, compared with the ionization energy of Xenon of approximately $12.1eV$.

As with the primary cathode tube, and similar to the JPL design[51], the keeper electrode was machined from a single piece of Poco graphite. Electrical connections were made with the support screws, seen in Fig. 6-10, which were electrically insulated from the base structure using ceramic sheaths and washers.

6.4.4 External Heater

As described in section 6.2 the ideal hollow cathode is self heating while in operation, meaning that heating directly from the internal plasma in the emitter region is sufficient to maintain the required surface temperature without external heating. However, in order to start the process with the keeper electrode described above, an external heater was required. Referring to section 6.4.1 the emitting surface must reach temperatures around $1770K$ for the desired emission to begin. This requirement presented several thermal constraints on the heater and overall design.

The high temperatures required for heating were well supported by refractory metals. Although tungsten is commonly used, tantalum was selected as the heating element due to its combination of high resistivity and less brittle behavior at high temperatures[57]. Specifically, a $0.25mm$ diameter tantalum wire was used.

Many resistive heaters consist of sheathed or beaded wires wrapped around the main cathode tube. Although simple, for small cathode tubes this approach may not be the most effective method of heating the insert. Commercially manufactured alumina beads were initially considered, however the physical dimensions ($3.1mm$ OD, $1.3mm$ ID, $3.25mm$ in length) of those available would have limited the number of turns focused around the emitting surface to only 3 or 4 turns. As a result, we would not expect uniform, efficient heating of the insert. As an alternative, a threaded ceramic tube tightly wrapped in tantalum wire

provided better surface contact between the heater assembly and the cathode tube compared with insulated wire coils and accommodated more turns per unit length. Specifically a boron nitride (see table 6.1) tube was machined with a thread on the outer surface. As shown in Figure 6-16, an additional ceramic sheath houses the assembly to prevent the coil from unwinding. The initial design used a $3/8-24$ thread on a $13.50mm$ long boron nitride tube with an OD of $9.0mm$ and ID of $5.0mm$(to slide over the cathode tube). Initially, a Cotronics 960 Alumina sheath, with $1.0mm$ wall thickness, was used to contain the heater. The heater current was intended to be returned through the cathode tube itself, with contact made near the cathode tip. This arrangement proved troublesome for several reasons. (1) A reaction between alumina and the tantalum wire[62] at high temperatures resulted in severe degradation of the assembly and deposited residue on the keeper and cathode housing. (2) The current return though the cathode tube may have been responsible for a temperature imbalance, leading to uneven thermal expansion and subsequent failure of the heater.

In the final design, the heater size was decreased, to a $5/16-24$ thread on a $7.30mm$ OD boron nitride tube, while the sheath material was replaced with boron nitride and reduced in size (to a $7.30mm$ID and $1mm$ wall thickness). In addition to avoiding the alumina-tantalum reaction, this modification allowed sufficient clearance between the heater and radiation shield (see section 6.4.4) for the current to be returned via the outside of the heater. Further modifications and photographs of heater are presented in section 7.1.2.
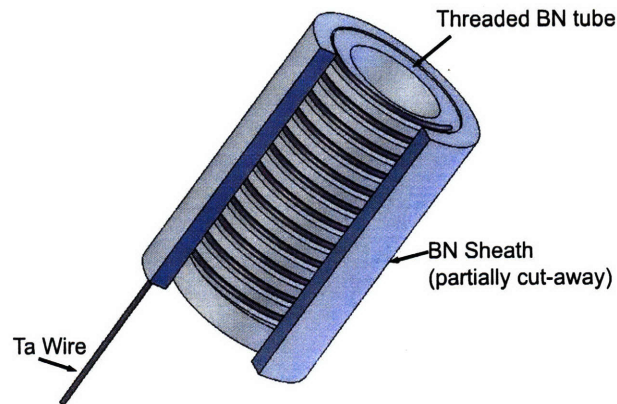
Figure 6-16: Partial cut-away view of the heater assembly used to heat the cathode insert to the temperatures required for emission.

6.4.5 Thermal Considerations

Although no detailed thermal model of the operating hollow cathode was performed, several measures were employed in order to reduce heat losses. These included considerations of both heat conduction and radiative losses.

Conduction Losses

The support structure and mounting flange were created from stainless steel and connected to the mounting structure within the vacuum chamber. As described previously, the cathode tube was designed to be as thin and long as possible in order to reduce heat conduction to this base. In order to further minimize heat flow, an alumina junction between the cathode tube and base was inserted. This also provided electrical insulation between the keeper and cathode potentials, see Figs. 6-10 and 6-11. The alumina junction was created from two pieces of Cotronics 960 machinable alumina, with a thermal conductivity of approximately $4.6W/mK$. Compared with the Poco graphite, with thermal conductivity of approximately $95W/mK$, a significant reduction in thermal energy loss can be expected.

Radiative Losses

As discussed above, the heater element must operate at high temperatures in order to heat the emitting element to the temperatures required for thermionic emission. The need for reducing radiative heat losses can be demonstrated most clearly with a simple example. The power radiated from the heater element and keeper electrode surfaces can be approximated using the modified Stefan-Boltzman relation[63], equation 6.8.

$$E_{rad} = \epsilon \sigma T^4 \tag{6.8}$$

Here, E_{rad} is the total radiated power per unit area, ϵ is the material emissivity, σ is the Stefan-Boltzman constant and T is the surface temperature. In a steady state condition, heat will be transferred between the heater and keeper by radiation, this power would then be dissipated either through radiation or conduction to the surroundings. Of interest is the power lost through radiation from the heater surface given by equation 6.9.

$$\dot{Q}_1 \approx \frac{\sigma(A_h T_h^4 - A_k T_k^4)}{\frac{1}{\epsilon_h} + \frac{1}{\epsilon_k} - 1}. \tag{6.9}$$

Here, A_h and A_k refer to the boron nitride heater and graphite keeper surface areas respectively. When, a large thin(at uniform temperature) heat shield is inserted between the heater and keeper (as shown in figures 6-11 and 6-10) equation 6.9 is modified as in equation 6.10.

$$\dot{Q}_2 \approx \frac{\sigma(A_h T_h^4 - A_k T_k^4)}{\left(\frac{1}{\epsilon_h} + \frac{1}{\epsilon_k} - 1\right) + \left(\frac{2}{\epsilon_s} - 1\right)}. \tag{6.10}$$

Where ϵ_s is the emissivity of the heat shield. Consider, for example, the power lost when the heater is held at a temperature of $1800K$, while the keeper is held at $500K$. The emissivities of boron nitride, graphite and tantalum are approximately 0.9 , 0.7 and 0.2 respectively (see table 6.1) at the temperatures of interest. Without the shield, from equation 6.9, $\dot{Q}_1 \approx 165W$. With the shield, from equation 6.10, $\dot{Q}_2 \approx 25W$, or 85% less than without a shield. Although this has been a crude and highly simplified analysis, the potential benefits of a heat shield are clear. Given this result, a $0.01''$ thick sheet of tantalum was rolled into a $12mm$ diameter tube and inserted between the keeper and cathode surfaces, as shown in Fig. 6-10. The shield is held in place by a small notch at the top of the keeper and contact with the alumina spacer at the base of the cathode, as shown in the figure.

6.4.6   Additional Features

Some additional aspects of the cathode design are briefly discussed here:

Propellant Flow: Flow is fed to the cathode by a single 1/8" OD, 0.055" ID type 316 stainless steel tube electron beam welded to the base support flange. In order to minimize flow losses, each component transition along the flow path was designed to couple to the next, as has been employed previously[51]. The couplings, seen in Fig. 6-11 consisted of corresponding outcrops and insets $5mm$ in diameter and $1mm$ in depth at both the cathode tube to alumina and alumina to base flange junctions.

Electrical Connections: In order to accommodate electrical connections to the cathode heater and an internal thermocouple two channels were cut into the lower alumina spacer at the cathode base. Shown in Figure 6-17, this feature, in addition to alumina insulation sleeves, allowed electrical connections to be made in a flexible configuration.

Thermocouple: During initial trials and heater testing, a small Type C Tungsten 5%-
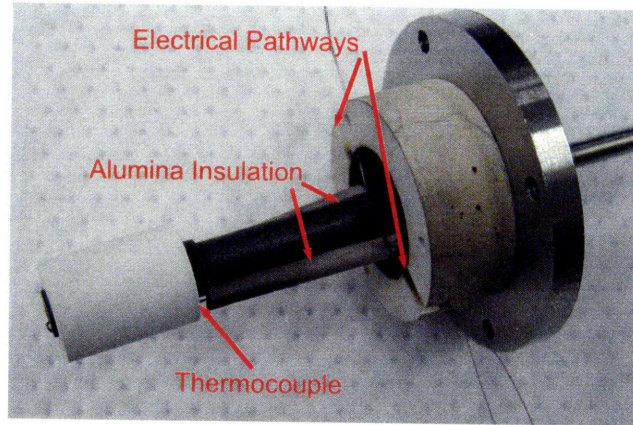
Figure 6-17: Electrical connection slots and thermocouple position. Alumina sleeves insulating the heater and thermocouple wires are shown in position along the cathode tube.

Rhenium versus Tungsten-26%-Rhenium thermocouple from *Omega* was installed as shown in Fig. 6-17. Although the maximum rated temperature of $2320 \deg C$ was likely not exceeded, the brittle nature of this type of thermocouple led to frequent failures during heating and subsequent changes to configuration between trials. Due to these failures, limited thermocouple data will be presented in section 7.1.2.

Chapter 7

LaB_6 Hollow Cathode Characterization

7.1 LaB_6 Hollow Cathode Testing

In order to characterize the MIT LaB_6 hollow cathode, a series of tests were preformed. These included an evaluation of the preheating method, current extraction to the keeper electrode and finally current extraction to an external anode. This chapter details the experiments performed and provides discussion and recommended operating settings for the cathode.

7.1.1 Experimental Configuration

The cathode was tested within the MIT SPL main vacuum chamber, described in section 3.1 for use with the DCF. A schematic overview of the experimental set up is shown in Figure 7-1. The two *Sorensen* DC power supplies described in section 3.1 were used to supply the keeper and anode potentials. Similarly the *MPJA* power supply used to heat the Busek cathode in chapter 3 was used as the heater power supply. Research grade (99.999% purity) xenon, from *Spectra Gasses* was used as the feed gas in all results presented here. The flow was regulated by one of the *Omega* external flow controllers described in section 3.1. The thermocouple voltage was measured using a hand held multi-meter and referencing the *Omega* calibration table for Type C thermocouples[38] while compensating for the reference temperature (assumed to be approximately room temperature). A cylindrical anode similar
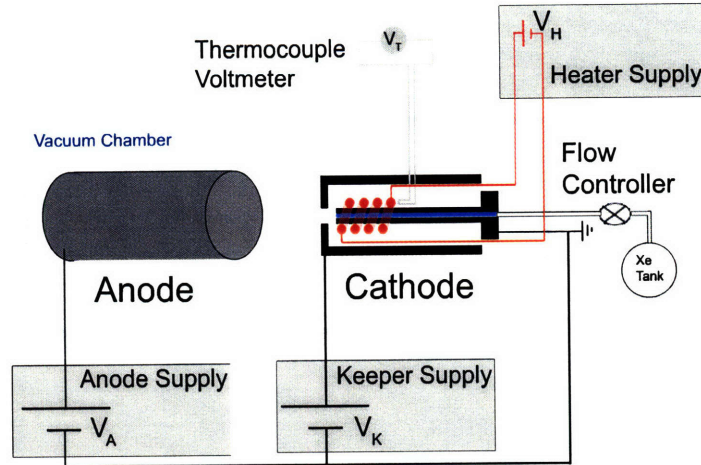
Figure 7-1: Sketch of experimental configuration used when characterizing the LaB_6 hollow cathode.

to others used in characterizing hollow cathodes[64, 52] has been employed. The anode was a $10cm$ long, $5cm$ diameter tube made of $0.005''$ perforated 316 stainless steel. See Figure 7-2 for a photograph of the anode configuration. The entrance to the anode was placed directly in line with the cathode keeper exit plane as can be seen in the figure.

7.1.2 Cathode Heating and Temperature Measurements

The cathode was been heated while $1sccm$ of xenon flow was passed through the insert. The heating element thermocouple described in section 6.4.6 was used to establish if temperatures approached the roughly $1500°C$, or $1773°K$ level required for emision, and to gauge the settling time for the temperature. Although the thermocouple continuously failed, sample data of the measured temperatures achieved are shown as a function of time in Figure 7-3. Recall, from section 6.4.6, that this temperature is not the insert temperature but rather that on the outside of the heater. The two curves in Fig. 7-3 represent the first two iterations of heater, both of the initial, larger, type described in section 6.4.4. In both cases, the heater current was increased to approximately $4.5A$. The first case, heater 1, included a portion of exposed wire outside the heater, roughly $3cm$, before it was connected to a thicker copper wire. Here, maximum power deposited was roughly $67W$ and the temperature appeared to settle around $870°K$ before the heater failed. The only modification made
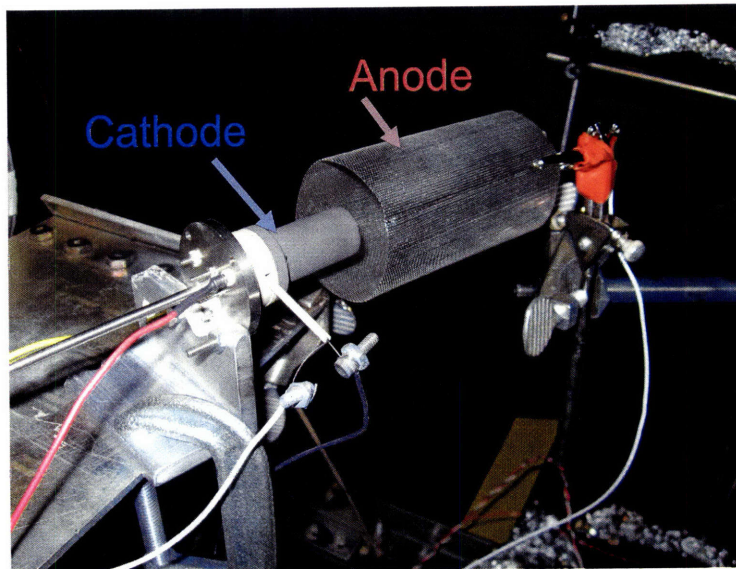
Figure 7-2: The LaB_6 cathode aligned with the cylindrical, stainless steel anode.
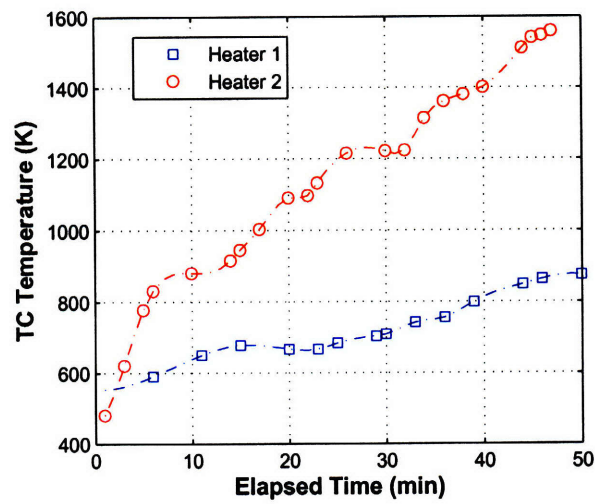
Figure 7-3: Measured thermocouple temperatures as a function of time. Heater 1 included a portion of unprotected wire, the Ta wire for heater 2 was entirely enclosed. In both cases the heater current was ramped up to roughly $4.5A$.

to heater 2 was to reduce the exposed wire length outside the cathode enclosure by including alumina insulating beads, as shown in Figure 7-4(a). Clearly this simple modification had a substantial effect, presumably through a reduction in radiative heat losses. Again, the current was ramped to roughly $4.5A$, but in this case the temperature (and hence heater resistance) increased significantly. Although the thermocouple failed at roughly $1580°K$, while depositing roughly $130W$ of power, this second case demonstrated that the desired temperatures may be within reach.

Given the discrepancies between heater trials shown in Fig. 7-3, further efforts were made to reduce heat losses. In addition to the design modifications already discussed (section 6.4.4), the length of high resistance tantalum wire was shortened as much as possible. This was accomplished through spot welding the heater wire to $0.4mm$ diameter molybdenum wire at the heater assembly, as shown in figure 7-4(b). A larger diameter molybdenum wire was selected as the material can withstand high temperatures[57], while the larger diameter was intended to reduce Ohmic losses away from the heater assembly. This reduced the final heater wire length from approximately $270mm$ to $192mm$. In addition, given the the apparent reliability issues and possible heat conduction path, the thermocouple was removed.

Relative temperatures could have been inferred from measuring the wire resistance as temperature varied, see[54]. For example, accounting for the approximately 1.4Ω line resistance between the power supply and heater wire, the heater resistance varied from 0.8 to 4.4Ω with zero current (heater off) and $4.5A$ of current(pre-ignition point) respectively. These recordings correspond to a resistivity range between $20\mu\Omega cm$ and $112\mu\Omega cm$ or to temperatures between about $100°C$ and $2600°C$ when a polynomial fit is used to interpolate the data in the referred data[54]. However, the sensitivity to wire dimensions meant that accurate temperature measurements were unreliable by this method.

Using the final heater iteration, temperatures required for ignition were reached after approximately 30 minutes of heating, beginning at $3.0A$ increasing to $4.5A$ of current supplied to the heater. At maximum heating, the total power was roughly $110W$, corresponding to·about $24V$ and $4.5A$ through the heater circuit. Although ignition temperatures were reached consistently using this configuration, the spot weld shown in Fig. 7-4(b) frequently failed. As a result, the present design iteration often requires that the chamber be vented to repair the circuit whenever the cathode discharge is stopped. Clearly this is not acceptable,

given that one of the proposed advantages of LaB_6, from section 6.3.1 was the ability to have a cathode available quickly and without the need for conditioning or other delays.

7.1.3 Current Extraction to the Keeper Only

The goal of these trials was to determine if the cathode emission could be sustained with a minimal amount of external heating. After heating the insert as described in the previous section, the keeper was biased to $600V$ with respect to the cathode tube in order to initiate a discharge. Once the discharge had been initiated, the keeper power supply was switched to a current limited state and the keeper potential decreased significantly to the levels presented in this section. Flow rate scans with keeper currents of $0.5A$, $0.75A$, $1.0A$ and $1.5A$ were performed with the results shown in Figure 7-5. For all tests the external heater was deactivated. In addition, the external anode circuit was open so no current was collected outside of the cathode assembly. The results clearly show that steady operation can be sustained at low flow rates with no external heating. Although plume mode transitions were expected theoretically, they were not observed in this configuration. A possible explanation may be that the low flows required for plume mode operation were not within the resolution/uncertainty of the flow meters available ($\pm 0.1 sccm$).

7.1.4 Current Extraction to the External Anode

In order to characterize the LaB_6 cathode spot to plume mode transitions, flow scans were performed using the anode configuration detailed in section 7.1.1. Although this experiment was intended to simulate the cathode performance when current is drawn to an external collector, say a Hall thruster anode, it is important to note that coupling potentials frequently have a strong dependence of the specific anode configuration[65, 50]. As a result, these data should not be seen as a quantitative representation of the actual power, or coupling losses of the cathode when operated with a particular thruster. During these trials, the anode current (I_A) and keeper current (I_K) were both held constant at the values indicated in Figures 7-6 to 7-8. The figures indicate the measured anode and keeper voltages, represented by V_A and V_K respectively in Fig. 7-1. The figures clearly demonstrate the transition from spot mode (low discharge voltages) to plume mode (high discharge voltages). In all runs the transitions began between roughly $1 sccm$ and $2 sccm$. In addition to the observed variations in voltage, a visual change in the plume was also

observed and can be seen in Figure 7-9. Here the apparent increase in the dominant visual wavelength from a violet to blue plume suggests an increase in the population of excited xenon ions. Referring to the discussion of section 6.2.3, these observations appear consistent with ionizations occurring outside of the cathode tube during plume mode operation. Large voltage fluctuations were observed at flow rates above roughly $4sccm$ during many trials. Occasional arc discharges were observed between the anode and cathode body at these flow rates suggesting the instabilities may have been due to excessive neutral particles in the cathode to anode region.
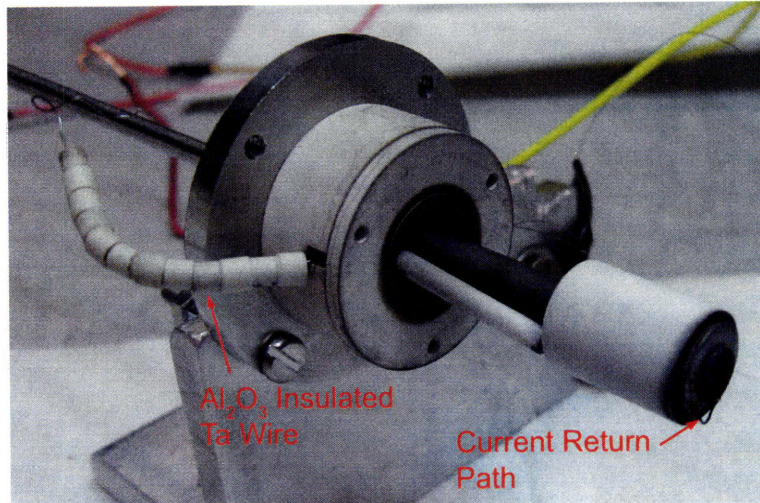
(a) Initially current flowed through a single Ta wire from outside the cathode through the heater and back through the cathode tube.
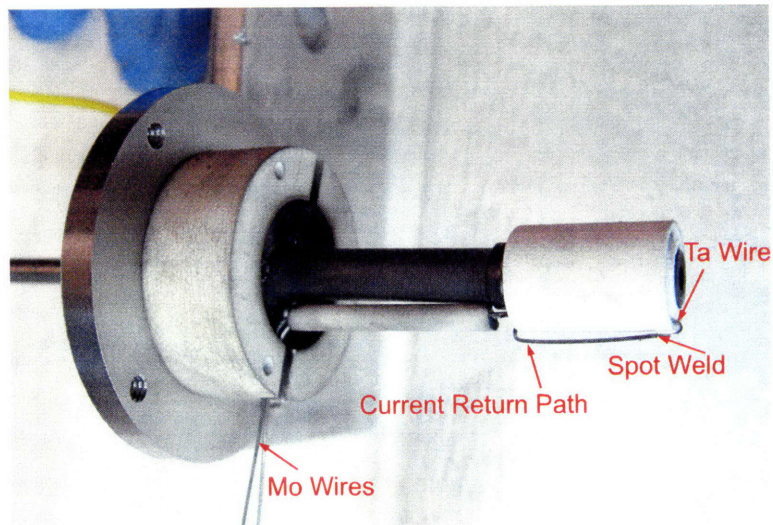
(b) The final heater configuration was electrically isolated from the cathode tube and incorporated Mo wires spot welded to the short Ta section in the heater.

Figure 7-4: Initial and final heater wire configurations.
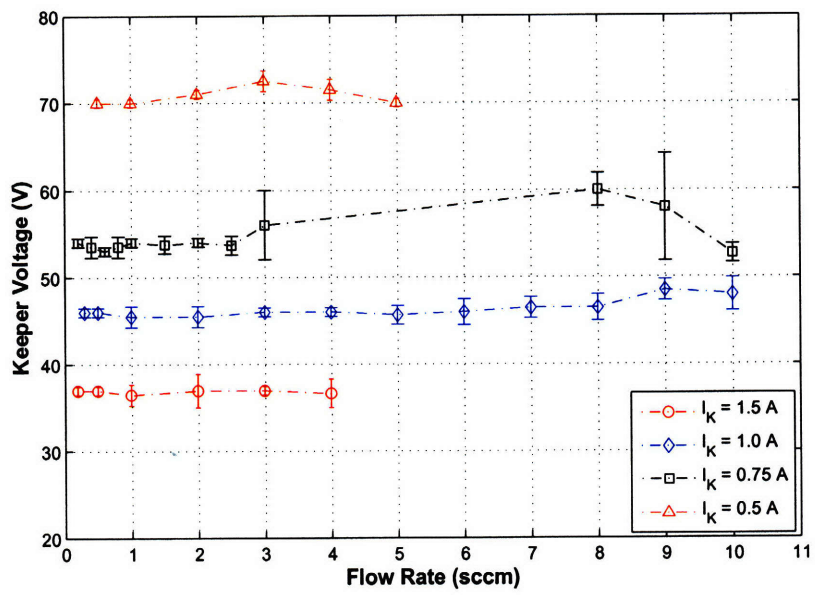
Figure 7-5: Keeper voltage with varying cathode flow rates, extracted current as indicated.
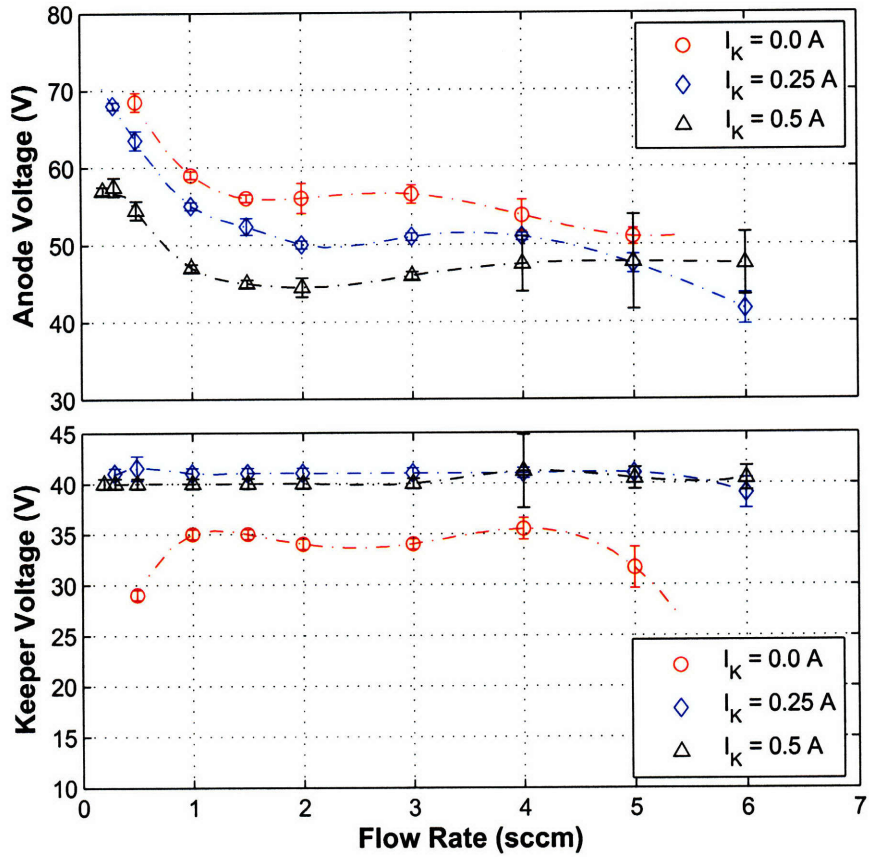
Figure 7-6: Plume mode transitions during flow scans with 1.0A drawn to the external anode and keeper current as indicated.
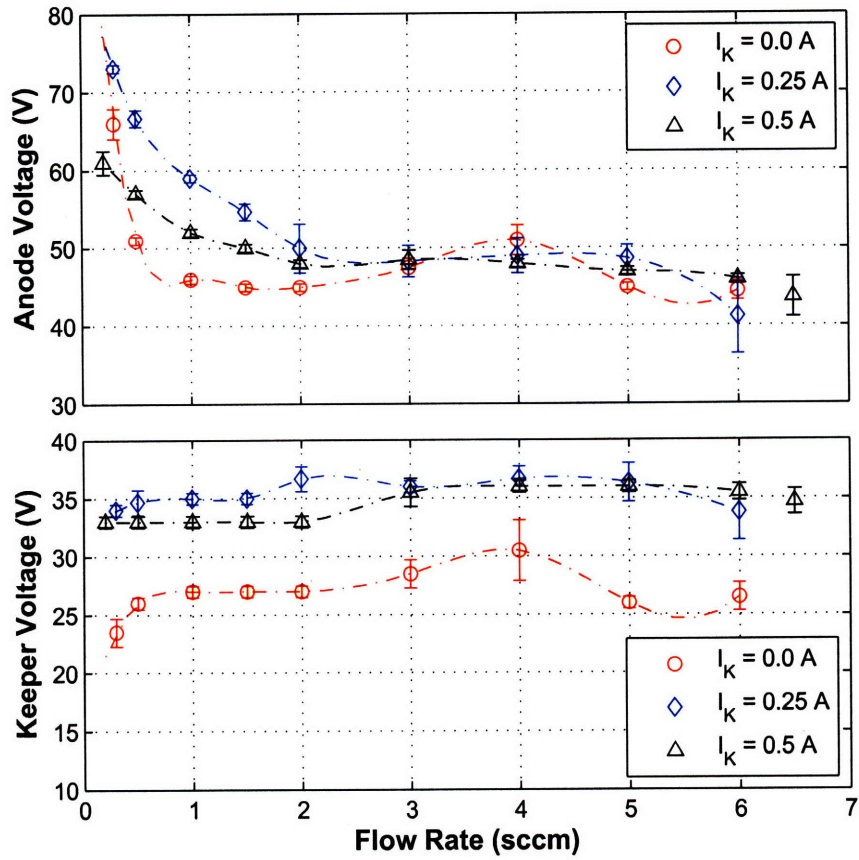
Figure 7-7: Plume mode transitions during flow scans with 1.5A drawn to the external anode and keeper current as indicated.
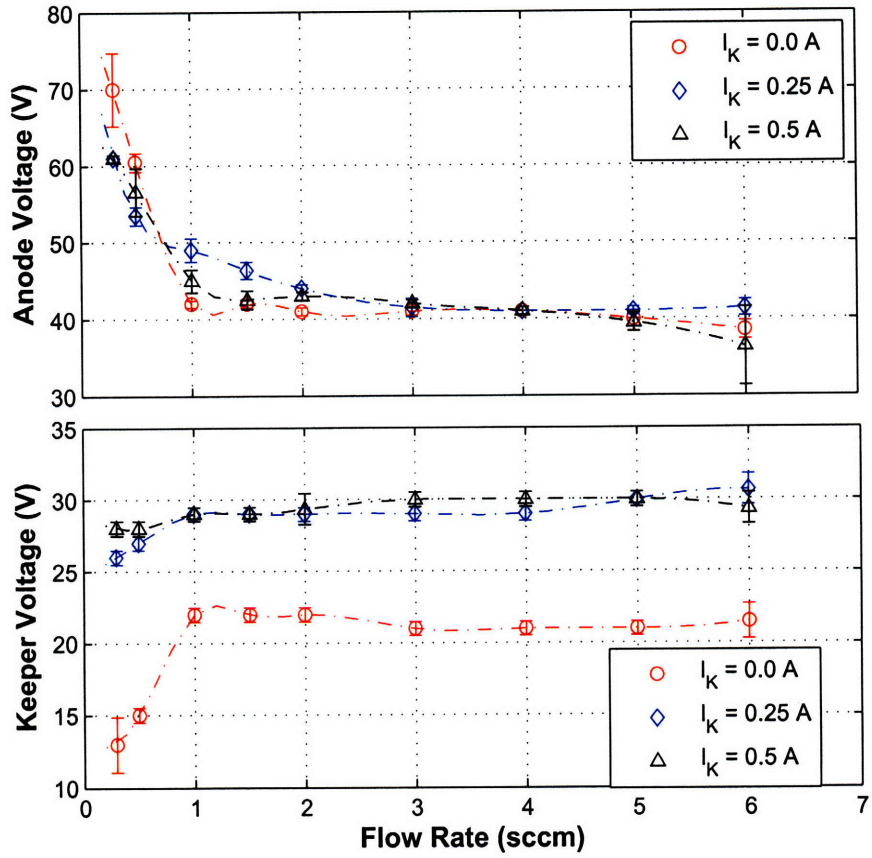
Figure 7-8: Plume mode transitions during flow scans with 2.0A drawn to the external anode and keeper current as indicated.
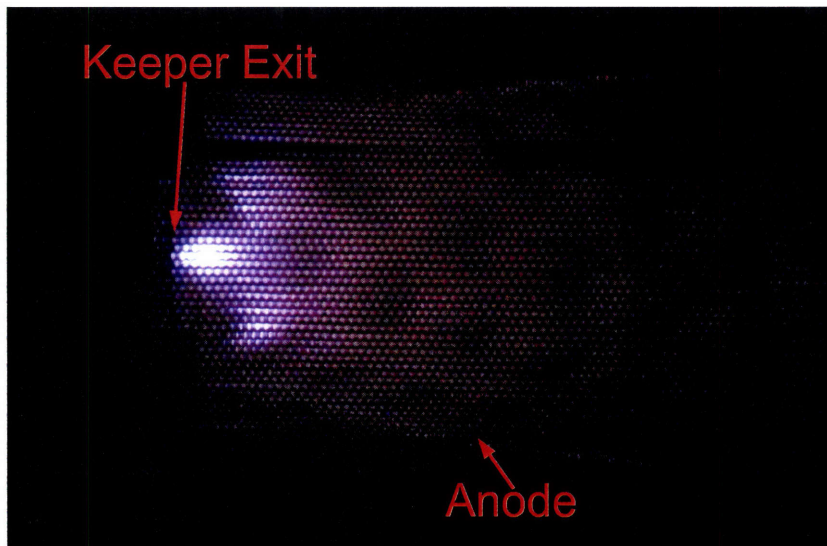
(a) Observed discharge during spot mode operation. The distinctly purple colouration is typical of excited neutral populations
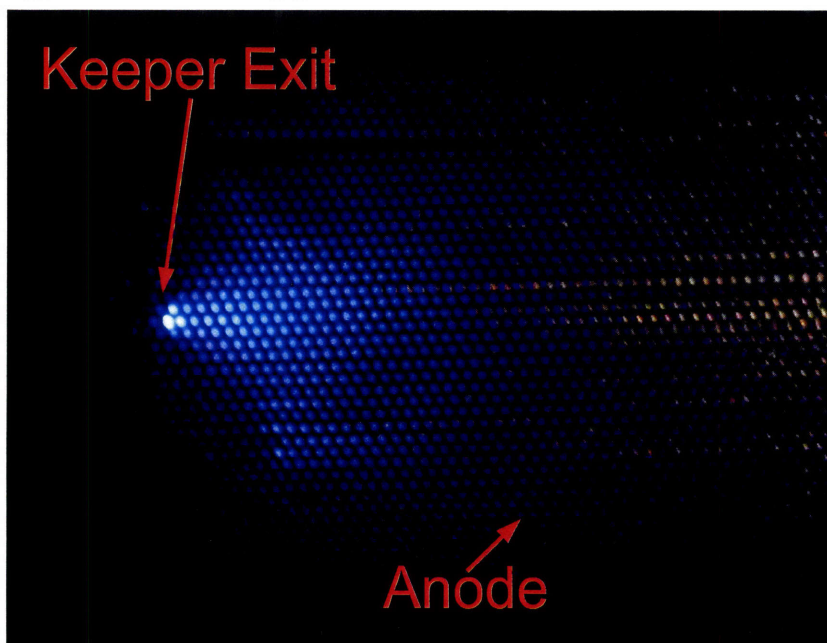
(b) Observed discharge during spot mode operation. The higher wavelength (more blue) colouration is typical of excited ion populations.

Figure 7-9: LaB_6 hollow cathode operating with the external anode.

7.2 LaB_6 Hollow Cathode Performance Evaluation

Given the results presented in the previous section, the cathode performed well in that operation was maintained with the external heater deactivated and anode currents could be drawn with the keeper circuit open. This section reviews the overall performance and comments on comparisons with similarly sized $BaO-W$ cathodes and larger LaB_6 cathodes. Specifically, plume to spot mode transitions will be discussed with an emphasis on the ideal operation conditions.

7.2.1 Heating Method

The threaded ceramic style of heater can be considered successful when compared with the heating mechanism employed in the Busek $BaO-W$ cathode. Just prior to emission, with $1sccm$ of flow the power being delivered to the LaB_6 cathode was roughly $110W$. Similarly, prior to emission the Busek cathode used in the DCF study used about $100W$, again with $1sccm$ of flow. The significantly higher temperatures required for the LaB_6 cathode for similar emission current densities suggest the heater used here was therefore reasonably efficient.

Below roughly $2sccm$, the keeper potential was relatively constant for all scans as shown in Fig. 7-5. The average power was therefore also roughly constant and has been plotted versus emitted current in Figure 7-10 for flow rates less than $2sccm$. As a basic assessment of the efforts performed in reducing heat transfer loses, notice that to maintain emission once the discharge was started, the keeper power was as low as $35W$ while emission was sustained. Thus the power required for self (plasma) heating was significantly less than the $110W$ used when achieving the required insert temperatures through external heating.

Regardless of the power required, confirmation that the cathode can be heated and operational within roughly 30 minutes verified one of the proposed advantages of the LaB_6 cathode discussed in 6.3.1; that using LaB_6 as the emitter eliminates the need for the lengthy conditioning processes required when using $BaO-W$ inserts.

7.2.2 Efficient Operating Regimes

From a practical point of view, when running cathodes in conjunction with a thruster, the operator typically desires stable cathode operation with both flow and power consumption

137
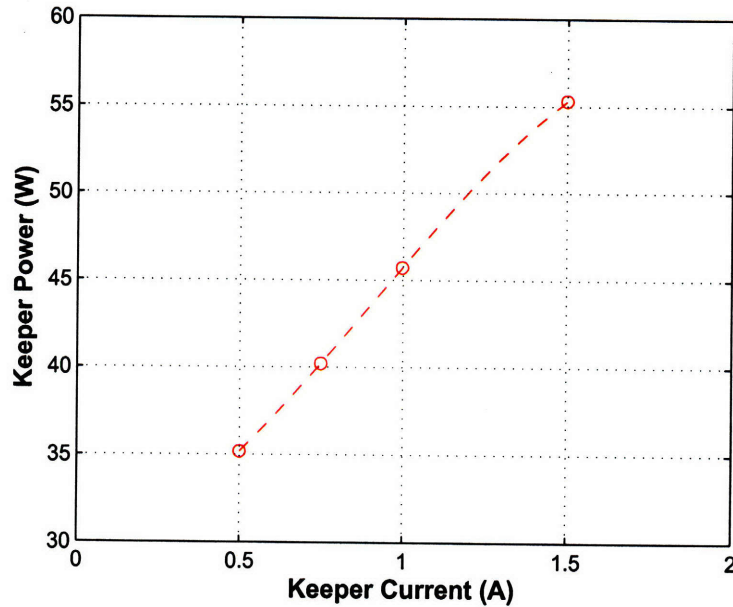
Figure 7-10: Average power required when operating with the keeper only, for flow rates less than $2sccm$.

minimized. With this in mind, the data of section 7.1.4 have been reproduced in Figures 7-11 to 7-13. In the figures, the total (anode plus keeper) power is plotted against flow rate. It is clear that at all anode currents the deactivated keeper provided the most efficient mode of operation. However, recall from section 6.2.1, figure 6-8 that the insert temperature required for emission is relatively insensitive to the current density within an order of magnitude of the current. Therefore at very low anode currents, it may be postulated that additional current drawn to the keeper may be the most efficient method of ensure sufficient insert heating. Figure 7-11, where $1.0A$ is extracted to the anode, may begin to indicate this as the discrepancies between curves are not as pronounced as with higher anode currents, although the keeper off state continues to be the most efficient. Further experimentation would be required to validate this concept. In all cases, for the lowest power state, plume mode transitions occurred around $1sccm$, indicating that operation at this flow rate (as desired in section 6.3.2) should be feasible.

138
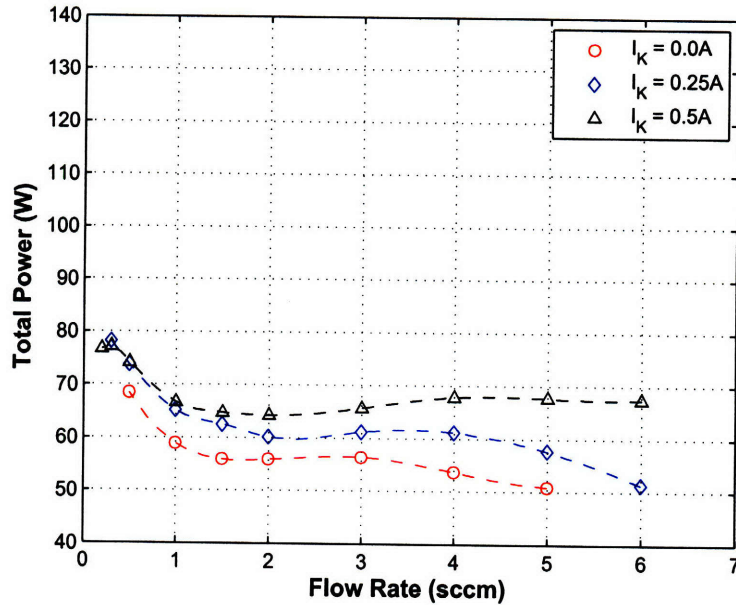
Figure 7-11: Total, keeper plus anode, power when extracting $1.0A$ to the anode.

7.2.3 Comparison with Similar Cathodes

In comparison with other hollow cathodes, discharge voltages consistently exceeded those of similarly sized $BaO - W$ type cathodes. This was expected given the higher work function of LaB_6. Specifically, consider operating with the keeper only and drawing $0.5A$ from the cathode. The LaB_6 cathode had a keeper potential of around $70V$ for all flow rates, thus consuming roughly $35W$, see Fig. 7-10. The Busek cathode used with the DCF, nominally requires approximately $10W$ to draw the same current ($\sim 20V, 0.5A$). Similarly the series of cathodes developed by Domonkos[49], required powers comparable to the Busek cathode, again using $BaO - W$ inserts.

When compared to the LaB_6 cathodes developed at JPL[51], the emission currents and physical cathode dimensions were far lower in this project. However the cathode to keeper powers were comparable. Here, the net current emitted ranged between 2.5 and $1.0A$ (at $I_A = 2.0A$, $I_K = 0.5A$ and $I_A = 1.0A$, $I_K = 0.0A$ respectively), while the emitting area was about $0.3cm^2$. The corresponding range in total current density from the emitter was hence 3 to $8.5A/cm^2$. Compared with a larger LaB_6 cathode developed by JPL[55], which had an estimated area of $2.5cm^2$, the same emitter current density corresponds to total currents

139
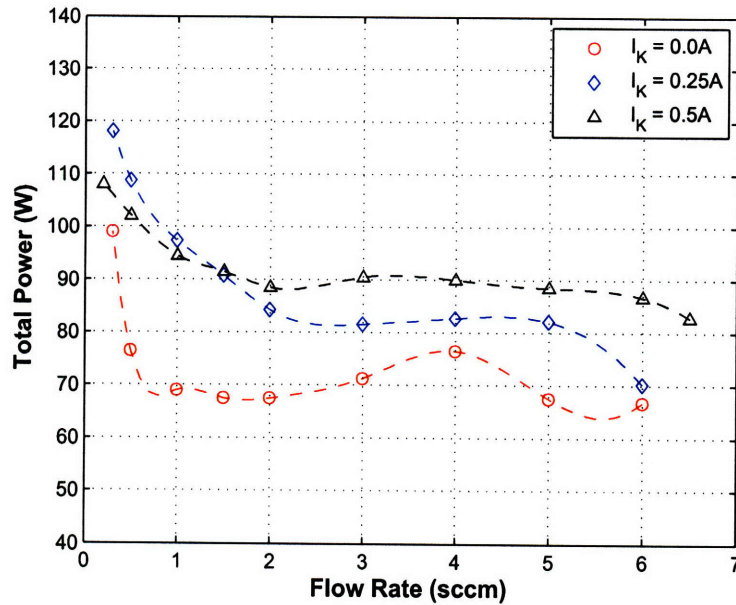
Figure 7-12: Total, keeper plus anode, power when extracting $1.5A$ to the anode.

between 7.5 and $21A$. Referring to the referenced data[55], the cathode to keeper power for the cathodes used in that study cathodes ranged between approximately $35W$ and $65W$. As shown in Figure 7-14, the LaB_6 cathode developed here required similar levels of cathode to keeper power for comparable current densities when considering the operating point just prior to plume mode transition. Recall that the coupling potential between the keeper and the anode (or thruster plume) potential is a strong function of anode configuration [50], as a result no comparisons are made on this basis.
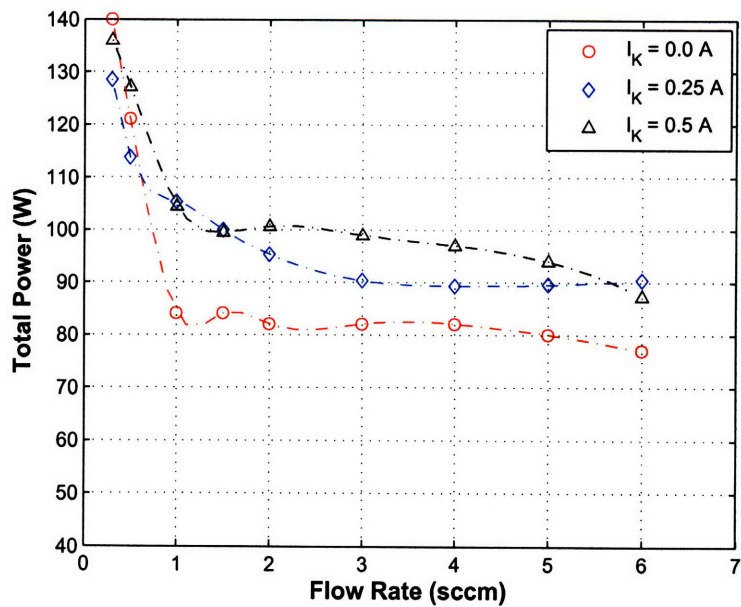
Figure 7-13: Total, keeper plus anode, power when extracting $2.0A$ to the anode.
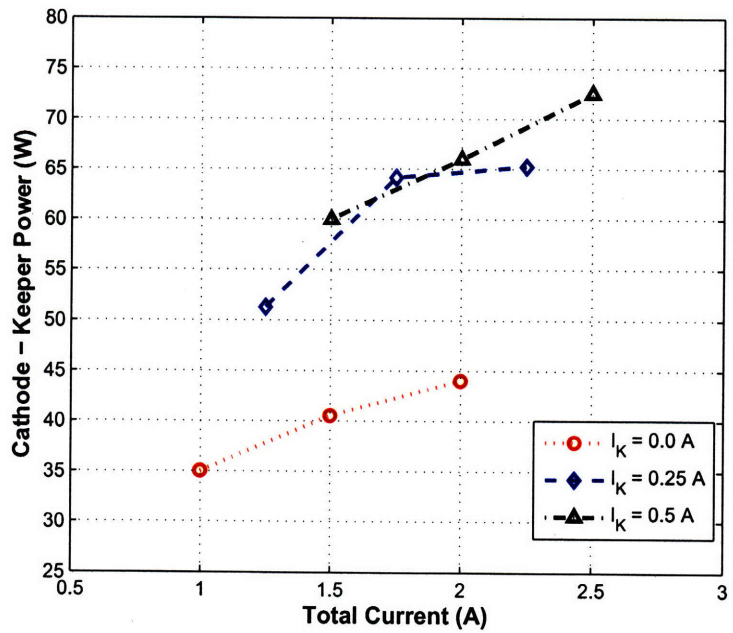
Figure 7-14: Cathode to keeper power deposited at minimum (for spot mode) flow rates, keeper currents as indicated.

7.3 Recommended Future Work

In addition to experimental and theoretical studies, several modifications to the overall design are recommended in this section.

7.3.1 Design Modifications

The principal modifications required after initial characterization are enhancements to promote more reliable and robust operation of the external heating element. The configuration used here failed after most runs, primarily at the spot weld location. In addition, the heater was not properly secured and can slide along the cathode tube if the spot weld breaks. Refer to Fig. 7-4(b) for visualization of these concerns. After the data presented here was collected the heater element broke free and made physical contact with the keeper electrode resulting in severe damage to the assembly through arcs and discharges in the cathode to keeper gap. The damage, shown in Figure 7-15, prevented further testing within the time span of this project. It may be possible to obtain a more robust physical connection by avoiding
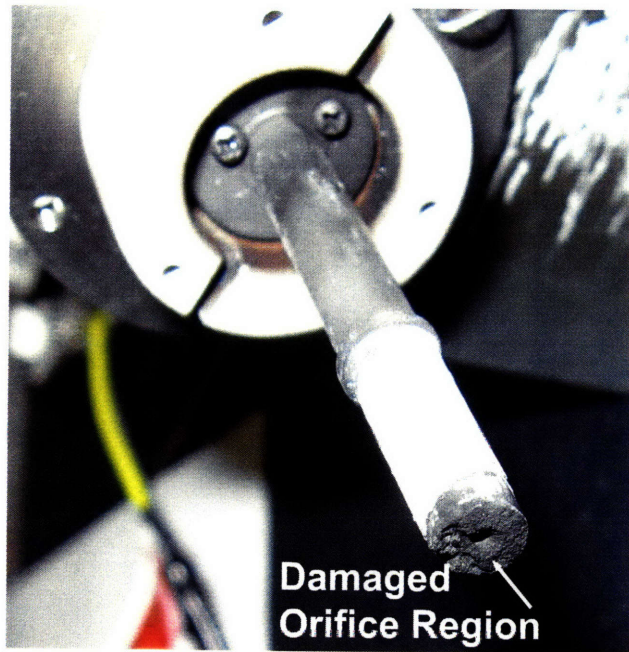
Figure 7-15: Damaged cathode tube after the heater assembly made contact with the keeper electrode during ignition.

a junction between differing materials at the spot weld junction. For example a tantalum

to tantalum (with different wire diameters) junction may be more secure. Another, more ideal, solution could be to create a variable diameter tantalum wire by electrochemically etching one section of a thick wire.

7.3.2 Experimental Studies

After the damage described above, the cathode tube was salvaged by reducing the top plate thickness. As a result the orifice aspect ratio was reduced to $AR = 0.3$. Specifically, the orifice length (as defined by Fig 6-13) was reduced to $0.3mm$. As can be seen in Figure 7-16, the damage was not completely repaired but the orifice appears to be relatively intact. The experiments presented in section 7.1 should be repeated with the modified aspect ratio. The results could allow some insight into the hypothesis made in section 6.4.2, that reducing the aspect ratio may primarily reduce the required power at such large orifice diameters.
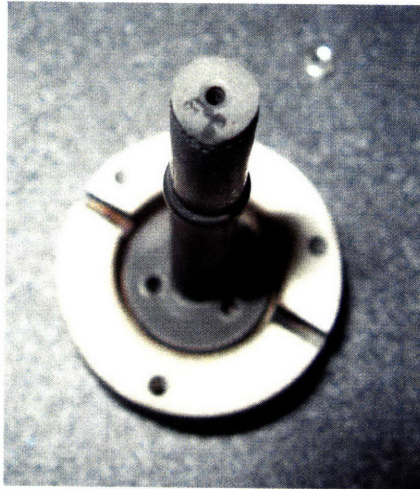
Figure 7-16: Cathode after reducing the orifice aspect ration to $AR = 0.3$. Not all damage seen in Fig. 7-15 could be repaired.

In addition to repeating the experiments with the new aspect ratio, the performance at lower anode currents should be evaluated. Not only is this important considering that the cathode will frequently be used at anode currents less than $0.5A$, but also to explore the most efficient operating regimes at low currents. It was postulated in section 7.2.2 that when supplying the low currents typically required for thrusters tested at SPL the most efficient mode of operation could require the keeper to draw some current at all times so as to maintain the required emitter temperature while still operating in spot mode.

Finally, repeating the trials with various propellants may be useful to determine their suitability for use in laboratory experiments. For example, argon may be a good cost effective alternative to xenon. In addition, given that LaB_6 should be relatively insensitive to impurity poisoning an experimental evaluation of the cathodes performance using cheaper, low grade xenon (or other propellants) would be useful.

7.3.3 Theoretical Developments

Several numerical models of hollow cathode discharge plasmas have been developed. Specifically a two dimensional model developed by Mikellides et. al[48] has shown excellent agreement with experimental measurements of the internal and cathode to keeper plasma regions within $BaO - W$ hollow cathodes. Application of this model to the LaB_6 cathode geometry employed here could be useful in optimizing the configuration. Similarly, a model of the plasma behavior from the orifice exit, through the keeper and coupling to a discharge plasma has been developed by Boyd et. al[66] with good agreement between theory and experiment. Again, if applied to this cathode, such a model may allow for optimization of the cathode to thruster plume coupling configuration. This may be particularly true when used with thrusters like the DCF, where cathode coupling was observed to have a significant impact on the thruster operation in chapter 3.

Finally, the theoretical explanations for the specific processes dictating spot to plume mode transitions at low flow rates[60, 58, 49] should be reviewed. An accurate criterion for the transition, rigorously explained through fundamental principles, would be extremely useful when developing future hollow cathodes.

7.4 LaB_6 Hollow Cathode Conclusion

The LaB_6 cathode presented in this study has operated at a satisfactory level in terms of the requirements outlined in section 6.3.2. Specifically, the cathode was shown to operate over a moderate range of discharge currents, in spot mode, at flow rates at or near to $1sccm$ in section 7.1.4. The cathode operated with the external heater deactivated during all trials, both with current drawn to the keeper electrode alone, or in combination with an external anode. When extracting current to an external anode, the discussion of section 7.2.2 demonstrated that the most efficient operating state occurred with the keeper electrode deactivated for all operating points explored.

Unlike common $BaO - W$ cathodes, this cathode does not require lengthy conditioning times and requires only a short 30 minute heating period to initiate a discharge. As discussed in section 7.2.1, peak heating powers were comparable with common $BaO - W$ cathodes[7] despite LaB_6 having a higher work function, and hence requiring greater temperatures for comparable emission.

The cathode design was based on previous LaB_6 cathodes developed at JPL[51, 55], modified to operate at lower discharge currents. Unique features, discussed in section 6.4 include a threaded ceramic heater which allowed for more turns of heater wire to be concentrated around the insert region compared with using simple insulated wires. In addition, a radiation shield was installed between the keeper and heater assemblies to reduce radiated heat loss within the cathode.

Prior to becoming a reliable cathode for use within the MIT Space Propulsion Laboratory, alterations to the heater mechanical design must be made to prevent the minor, and major, failures discussed in section 7.3.1.

145

Bibliography

[1] Koch, N., Harmann, H. P., and Kornfeld, G., "Status of the THALES High Efficiency Multi Stage Plasma Thruster Development for HEMP-T 3050 and HEMP-T 30250," 30th *International Electric Propulsion Conference*, Florence, Italy, September 2007, also IEPC-2007-110.

[2] Koch, N., Harmann, H. P., and Kornfeld, G., "Development and Test Status of the THALES High Efficiency Multistage Plasma (HEMP) Thruster Family," 29th *International Electric Propulsion Conference*, Princeton University, October-November 2005.

[3] Kornfeld, G., Koch, N., and Coustou, G., "First Test Results of the HEMP Thruster Concept," 28th *International Electric Propulsion Conference*, Toulouse, France, March 2003, also IEPC–03–134.

[4] Smirnov, A., Raitses, Y., and Fisch, N. J., "Enhanced Ionization in the Cylindrical Hall Thruster," *Journal of Applied Physics*, Vol. 94, No. 2, 2003.

[5] SAINT GOBAIN BORON NITRIDE, "HP Grade Boron Nitride," www.bn.saint-gobain.com/.

[6] Azziz, Y., "Experimental and Theoretical Characterization of a Hall Thruster Plume," Ph.D. Thesis, Massachusetts Institute of Technology, Cambridge, MA,, 2007.

[7] BUSEK COMPANY, "Natick, Massachusetts, USA," www.busek.com.

[8] Martínez-Sánchez, M. and Pollard, J. E., "Spacecraft Electric Propulsion - An Overview," *Journal of Propulsion and Power*, Vol. 14, No. 5, 1998, pp. 688–699.

[9] Martínez-Sánchez, M., "MIT Course 16.522, Space Propulsion Notes," MIT Open Coursware, http://ocw.mit.edu.

[10] Polk, J. E., Kakuda, R. Y., Brinza, D., Katz, I., Anderson, J. R., Brophy, J., Rawlin, V., Patterson, M. J., Sovey, J., and Hamley, J., "Demonstration of the NSTAR Ion Propulsion System on the Deep Space One Mission," 27th *International Electric Propulsion Conference*, Pasadena, CA, October 2001, also IEPC–2001–075.

[11] Kim, V., "Main Physical Features and Processes Determining the Performance of Stationary Plasma Thrusters," *Journal of Propulsion and Power*, Vol. 14, No. 5, 1998, pp. 736–743.

[12] Warner, N. Z., "Theoretical and Experimental Investigation of Hall Thruster Miniaturization," Ph.D. Thesis, Massachusetts Institute of Technology, Cambridge, MA, June 2007.

[13] Sovey, J. S., "Improved Ion Containment Using a Ring-Cusp Ion Thruster," 16th *International Electric Propulsion Conference*, New Orleans, LA, November 1982, also AIAA–82–1928.

[14] Zhurin, V. V., Kaufman, H. R., and Robinson, R. S., "Physics of Closed Drift Thrusters," *Plasma Sources Science and Technology*, Vol. 8, 1999.

[15] Smirnov, A., Raitses, Y., and Fisch, N. J., "Experimental and Theoretical Studies of Cylindrical Hall Thrusters," *Physics of Plasmas*, Vol. 14, No. 057106, 2007.

[16] Cheng, S. Y.-M., "Modeling of Hall Thruster Lifetime and Erosion Mechanisms," Ph.D. Thesis, Massachusetts Institute of Technology, Cambridge, MA, 2007.

[17] Hutchinson, I. H., *Principles of Plasma Diagnostics*, Cambridge University Press, Cambridge, UK, 2002.

[18] Kornfeld, G., Koch, N., and Harmann, H. P., "Physics and Evolution of HEMP-Thrusters," 30th *International Electric Propulsion Conference*, Florence, Italy, September 2007, also IEPC-2007-108.

[19] Kornfeld, G., Koch, N., and Harmann, H. P., "New Performance and Reliability Results of the THALES HEMP Thruster," 4th *International Spacecraft Propulsion Conference*, Cagliari, Italy, June 2004.

[20] Kornfeld, G., Coustou, G., and Emsellem, G., "Plasma Accelerator System," United States Patent 7,075,095 B2, 2006.

[21] Raitses, Y. and Fisch, N. J., "Parametric Investigations of a Nonconventional Hall Thruster," *Physics of Plasmas*, Vol. 8, No. 5, 2001.

[22] Kornfeld, G., "Plasma Accelerator Arrangement," United States Patent 6,523,338 B1, 2003.

[23] Harmann, H. P., Koch, N., and Kornfeld, G., "The ULAN Test Station and its Diagnostic Package for Thruster Characterization," 30th *International Electric Propulsion Conference*, Florence, Italy, September 2007, also IEPC-2007-119.

[24] Raitses, Y. and Fisch, N. J., "Cylindrical Geometry Hall Thruster," United States Patent 6,448,721 B2, 2002.

[25] Raitses, Y., Smirnov, A., Granstedt, E., and Fisch, N. J., "Overrun Discharge Current Operation of Low Power Cylindrical Hall Thrusters," 30th *International Electric Propulsion Conference*, Florence, Italy, September 2007, also IEPC-2007-222.

[26] Smirnov, A., Raitses, Y., and Fisch, N. J., "Plasma Measurements in a 100W Cylindrical Hall Thruster," *Journal of Applied Physics*, Vol. 95, No. 5, 2004.

[27] Raitses, Y., Smirnov, A., and Fisch, N. J., "Cylindrical Hall Thrusters," 37th *AIAA Plasmadynamics and Lasers Conference*, San Francisco, California, June 2006, also AIAA-2006-3245.

[28] Shiraskaki, A., Tahara, H., and Yoshikawa, T., "Plume Measurements and Miniaturization of Hall Thrusters With Circular Cross-Section and Discharge Chambers," 29th *International Electric Propulsion Conference*, Princeton, NJ, October 2005, also IEPC–2005–051.

[29] Ahedo, E., Martínez-Cerzo, P., and Martínez-Sánchez, M., "One-Dimensional Model of the Plasma Flow in a Hall Thruster," *Physics of Plasmas*, Vol. 8, No. 6, 2001.

[30] Kaufman, H. R., Robinson, R. S., and Seddon, R. I., "End-Hall Ion Source," *Journal of Vacuum Science and Technology A*, Vol. 5, No. 4, 1987, pp. 2081–2085.

[31] ANSOFT CORPORATION, "Maxwell SV," www.ansoft.com.

[32] DEXTER MAGNETIC TECHNOLOGIES, "Somariun Cobalt (Sm-Co) Magnets," http://www.dextermag.com/Samarium-Cobalt.aspx.

[33] Moskowitz, L. R., *Permanent Magnet Design and Application Handbook*, Krieger Publishing Company, 1995.

[34] ALPHALAB INCORPORATE, "DC Magnometer," www.trifield.com.

[35] Rose, E., "Eric's Machine Shop, Natick, MA," 508-655-2448.

[36] SMALL PARTS INCORPORATE, "Sintered S/S Filter Type 316L, 10μ Pore Size," www.smallparts.com.

[37] INSULATOR SEAL, "Cryogenic Break," www.isi-seal.com.

[38] "Omega Temperature Measurement Handbook, Volume 2010, 6th Edition," Omega Engineering Inc., 2007.

[39] Tartz, M. and Neumann, H., "Sputter Yields of Carbon Materials under Xenon Ion Incidence," *Plasma Porcesses and Polymers*, Vol. 4, 2007.

[40] POCO GRAPHITE, "AXF-5Q Grade Graphite," www.poco.com.

[41] Domonkos, M. T., Marrese, C. M., Haas, J. M., and Gallimore, A. D., "Very Near-Field Plume Investigation of the D55," 33rd *Joint Propulsion Conference and Exhibit*, Seattle, WA, July 1997, also AIAA-1997-3062.

[42] Fox, J., "Advances in Fully-Kinetic PIC Simulations of a Near-Vacuum Hall Thruster and Other Plasma Systems," Ph.D. Thesis, Massachusetts Institute of Technology, Cambridge, MA,, 2007.

[43] Gildea, S., "Fully Kinetic Modeling of a Divergent Cusped Field Thruster," M. Sc. Thesis Project, Massachusetts Institute of Technology, Cambridge MA, In Progress.

[44] MIT Course 16.83, S. S. E., "Propulsion Laboratory," Department of Aeronautics and Astronautics.

[45] Neamen, D. A., *Seminconductor Physics and Devices*, McGraw-Hill Higher Education, 2003.

[46] Anders, A. and Kühn, M., "Characterization of a Low-energy Constricted-plasma Source," *Review of Scientific Instruments*, Vol. 69, No. 3, 1998.

[47] Prewett, P. D. and Allen, J. E., "The Double Sheath Associated With a Hot Cathode," *Proceedings of the Royal Society, London,*, No. 348, 1976.

[48] Mikellides, I. G., Katz, I., Goebel, D. M., and Polk, J., "Hollow Cathode Theory and Experiment. II. A Two-Dimensional Theoretical Model of the Emitter Region," *Journal of Applied Physics*, Vol. 98, No. 113303, 2005.

[49] Domonkos, M. T., "Evaluation of Low-Current Orificed Hollow Cathodes," Ph.D. Thesis, University of Michigan, Ann Arbor , MI,, 1999.

[50] Goebel, D. M., "Personal Communications," 2007.

[51] Goebel, D. M. and Watkins, R. M., "LaB_6 Hollow Cathodes for Ion and Hall Thrusters," 41st *Joint Propulsion Conference and Exhibit*, Tucson, AR, July 2005, also AIAA–2005–4239.

[52] Fossum, E. C., Sommerville, J. D., and King, L. B., "Characterization of Near Field Plasma Environment of a Hollow Cathode Assembly," 40th *Joint Propulsion Conference and Exhibit*, For Lauderdale, FL, July 2004, AIAA-2004-3795.

[53] Goebel, D. M., Jameson, K. K., Watkins, R. M., Katz, I., and Mikellides, I. G., "Hollow Cathode Theory and Experiment. I. Plasma Characterization Using Fast Miniature Scanning Probes," *Journal of Applied Physics*, Vol. 98, No. 113302, 2005.

[54] "Handbook of Chemistry and Physics, 88th Edition," CRC Press, 2008.

[55] Polk, J. E., Goebel, D. M., and Watkins, R., "Characterization of Hollow Cathode Performance and Thermal Behavior," 42nd *Joint Propulsion Conference and Exhibit*, Sacramento, CA, July 2006, also AIAA–2006–5255.

[56] COTRONICS CORPORATION, "960 Grade Machinable Alumina," www.cotronics.com.

[57] ALFA AESAR, "A Johnson Matthey Company," www.alfa.com.

[58] Kaufman, H. R. and Rehn, L., "Correlation of Inert Gas Hollow Cathode Performance," 13th *International Electric Propulsion Conference*, 1978, also AIAA.

[59] M. T. Domonkos, A. D. G. and Patterson, M. J., "Parametric Investigation of Orifice Aspect-Ratio on Low Current Hollow Cathode Power Consumption," 1999.

[60] Mandell, M. J. and Katz, I., "Theory of Hollow Cathode Operation in Spot and Plume Modes," 30th *Joint Propulsion Conference*, Indianapolis, IN, June 1994, also AIAA–94-3134.

[61] Domonkos, M. T. and Gallimore, A. D., "An Evaluation of Hollow Cathode Scaling to Very Low Power and Flow Rate," 1997.

[62] Xu, X., Oh, W. S., and Goodman, D. W., "Interfacial Reactions between Oxide Films and Refractory Metal Substrates," *Langmuir*, Vol. 12, 1996, pp. 4877–4881.

[63] Çengel, Y. A., *Heat Transfer, A Practial Approach*, McGraw-Hill Higher Education, 2003.

[64] Warner, D., "Personal Communication," Air Force Institute of Technology, 2008.

[65] Sommerville, J. D. and King, L. B., "Effect of Cathode Position on Hall-Effect Thruster Performance and Cathode Coupling Voltage," 30th *International Electric Propulsion Conference*, Florence, Italy, September 2007, IEPC-2007-78.

[66] Boyd, I. D. and Yim, J. T., "Modeling of the Near Field Plume of a Hall Thruster," *Journal of Applied Physics*, Vol. 95, No. 9, 2004, pp. 4575–4584.

Appendix A

MIT Diverging Cusped Field Thruster Drawings

154

S Magnetic Orientation

N

45°

Ø44.9

Ø55.2

Ø64

12.5

Magnetic Orientation N

S

45°

Ø32.4

Ø42.8

Ø64

12.5

45°

S

N Magnetic Orientation

12.5

Ø64

Ø30.4

Ø20
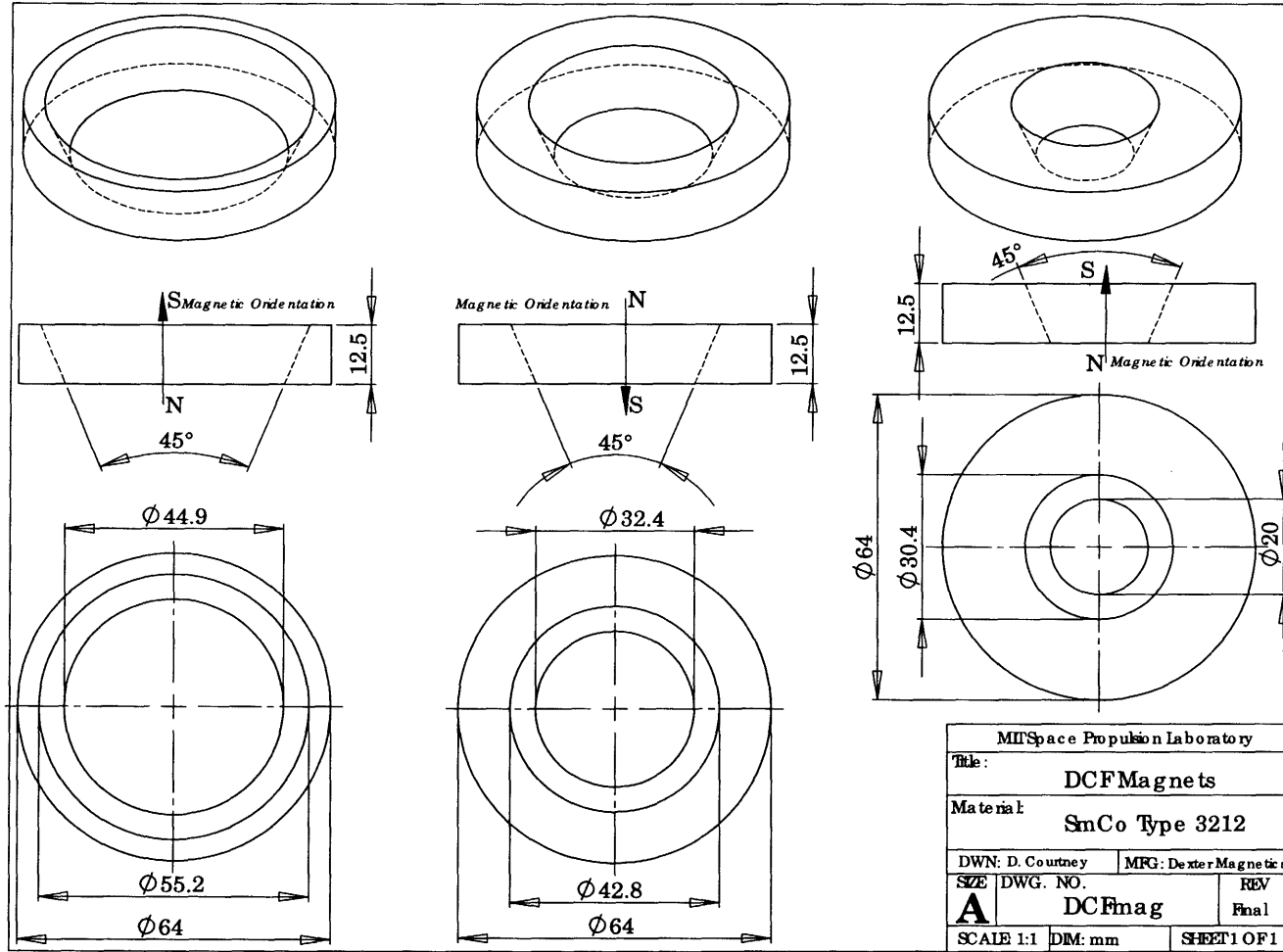
MIT Space Propulsion Laboratory		
Title: DCF Magnets		
Material: SmCo Type 3212		
DWN: D. Courtney	MFG: Dexter Magnetics	
SIZE A	DWG. NO. DCFmag	REV Final
SCALE 1:1	DIM: mm	SHEET 1 OF 1

2

1

Base Core

Space Cores

Hole Pattern:
Tap : 1/4-20
6 x 7/32" Drill
Depth: 12mm

∅3
∅3

∅9

12

64

2.50

64

∅30.36

2.50

∅44.85

∅32.42

∅42.78

12

64

24.50

7.50

∅15

1.59

19.05

MIT Space Propulsion Laboratory		
Title : DCF Core Pieces		
Material: 1018 Carbon Steel		
DWN: D. Courtney	MFG: D. Courtney	
SIZE A	DWG. NO. DCFcore	REV Final
SCALE 1:1	DIM: mm	SHEET 1 OF 1

2

1

SIDE

74

67.50°

3

4

74

9.6

12

Ø64

Hole Pattern:
Tap : 10-24
6 x # 20 Drill
Depth: 9.6mm

Ø55.2

TOP

Hole Pattern:
For 1/4-20 Shoulder Cap Screw
6 x 5/16" Thru
6 x 7/16" to 2.65mm Depth

(36)

BOTTOM

Ø58.5

Ø82

MIT Space Propulsion Laboratory		
Title : DCF Casing		
Material: 316 Stainless Steel		
DWN: D. Courtney	MFG: D. Courtney	
SIZE **A**	DWG. NO. DCF Case	REV Final
SCALE 1:1	DIM: mm	SHEET 1 OF 1

2

1

Anode:
316 Stainless Steel

Nut:
(Thread to match anode)
316 Stainless Steel

Sheath:
HP Boron Nitride

Large Spacer:
HP Boron Nitride

Spacer:
HP Boron Nitride
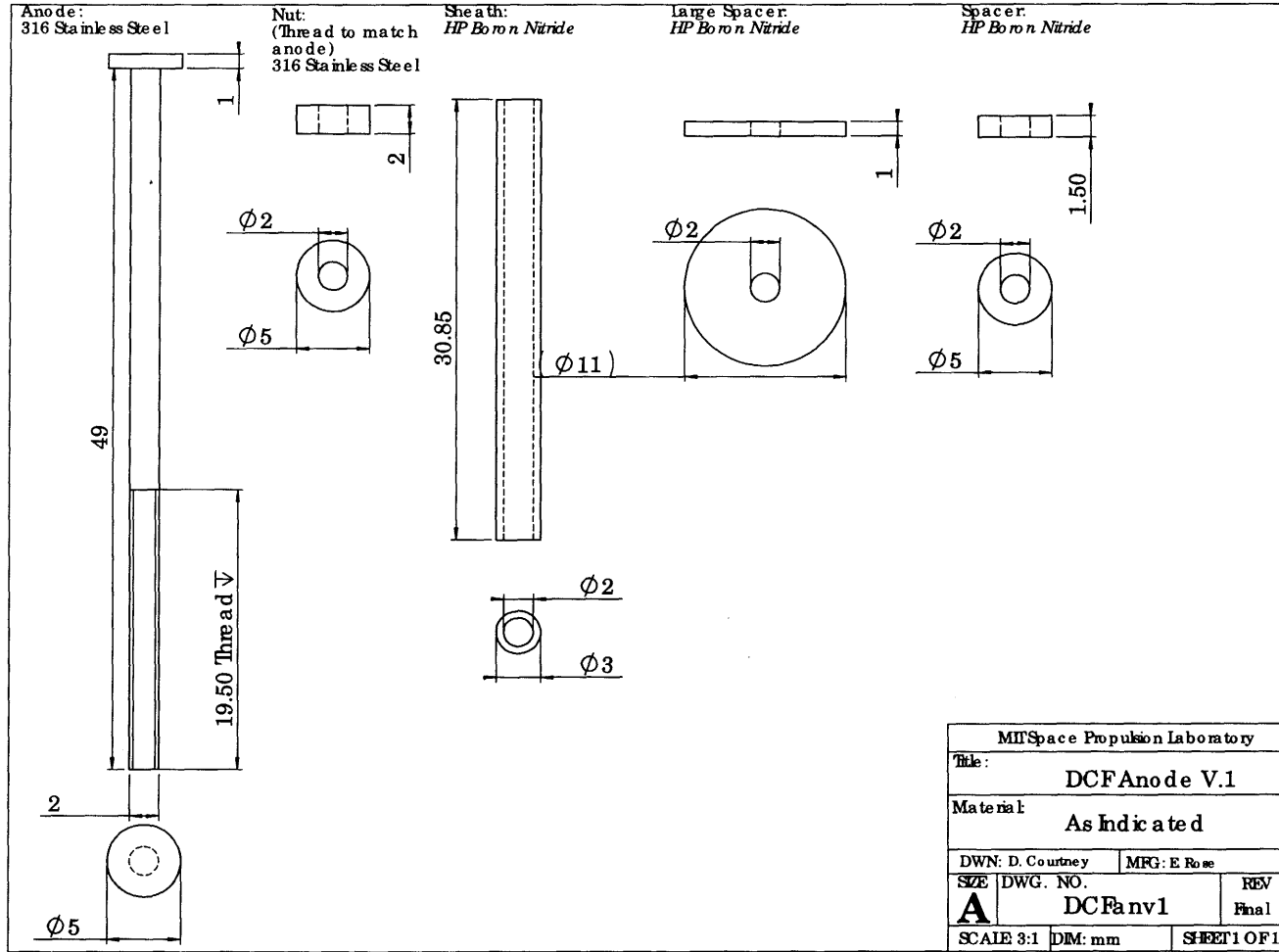
MIT Space Propulsion Laboratory

Title :	DCF Anode V.1		
Material:	As Indicated		
DWN: D. Courtney		MFG: E Rose	
SIZE A	DWG. NO. DCFanv1		REV Final
SCALE 3:1	DIM: mm		SHEET 1 OF 1

Anode:
AXF-5Q Poco Graphite

Anode Disc:
HP Boron Nitride

Anode Riser:
HP Boron Nitride

Diffuser Disc:
316 Stainless Steel
Porous/10um pores

$\phi 11$

$\phi 5$

$\phi 2$

$\phi 2$

$\phi 19.05$

$\phi 9$

$\phi 5$

1.59

50

2

MIT Space Propulsion Laboratory		
Title : DCF Anode V.2		
Material: As Indicated		
DWN: D. Courtney	MFG: D. Courtney	
SIZE **A**	DWG. NO. DCFanv2	REV Final
SCALE 3:1	DIM: mm	SHEET 1 OF 1

45°

56

3

49.5

15

20

58.5

Ø74
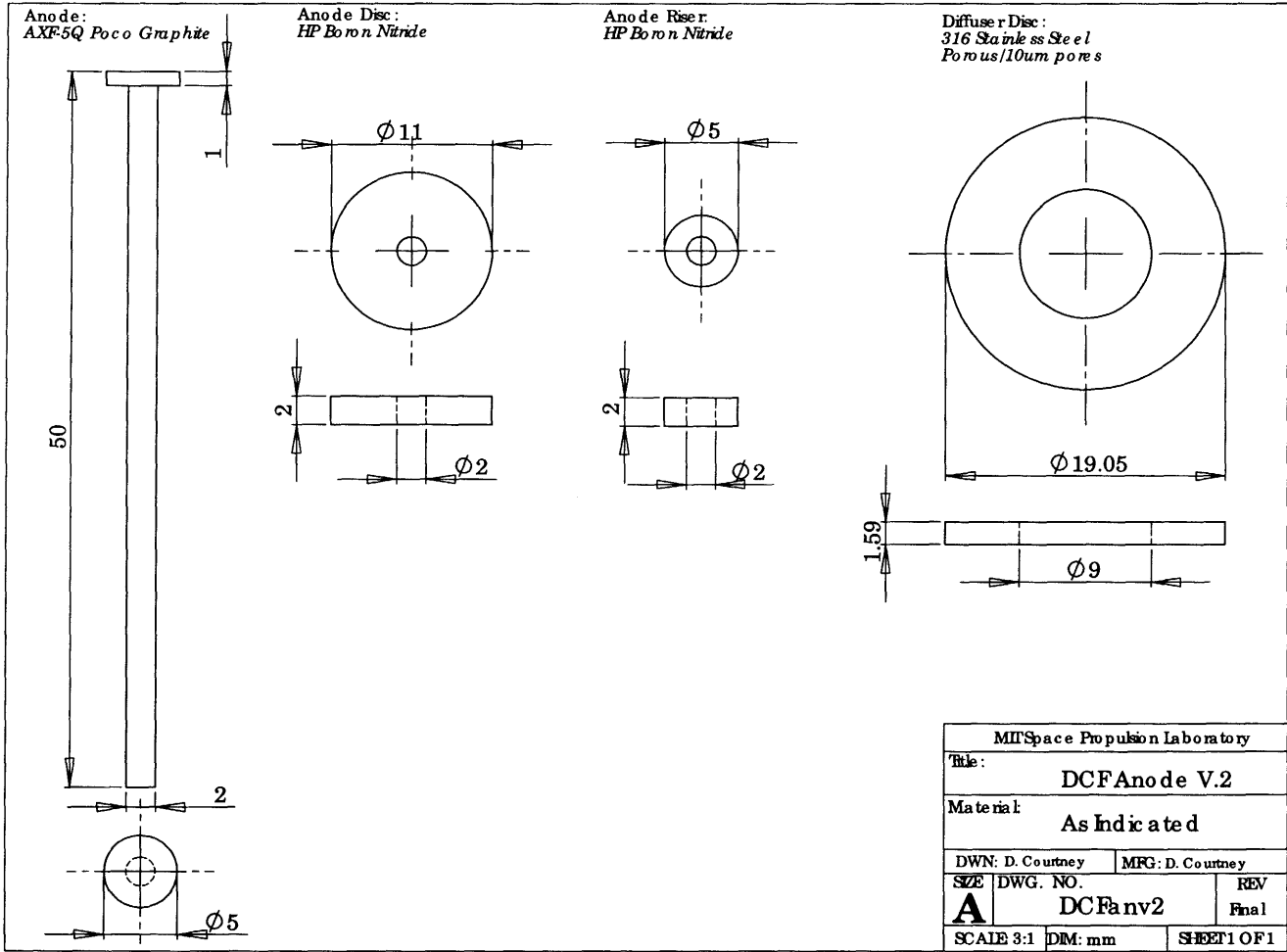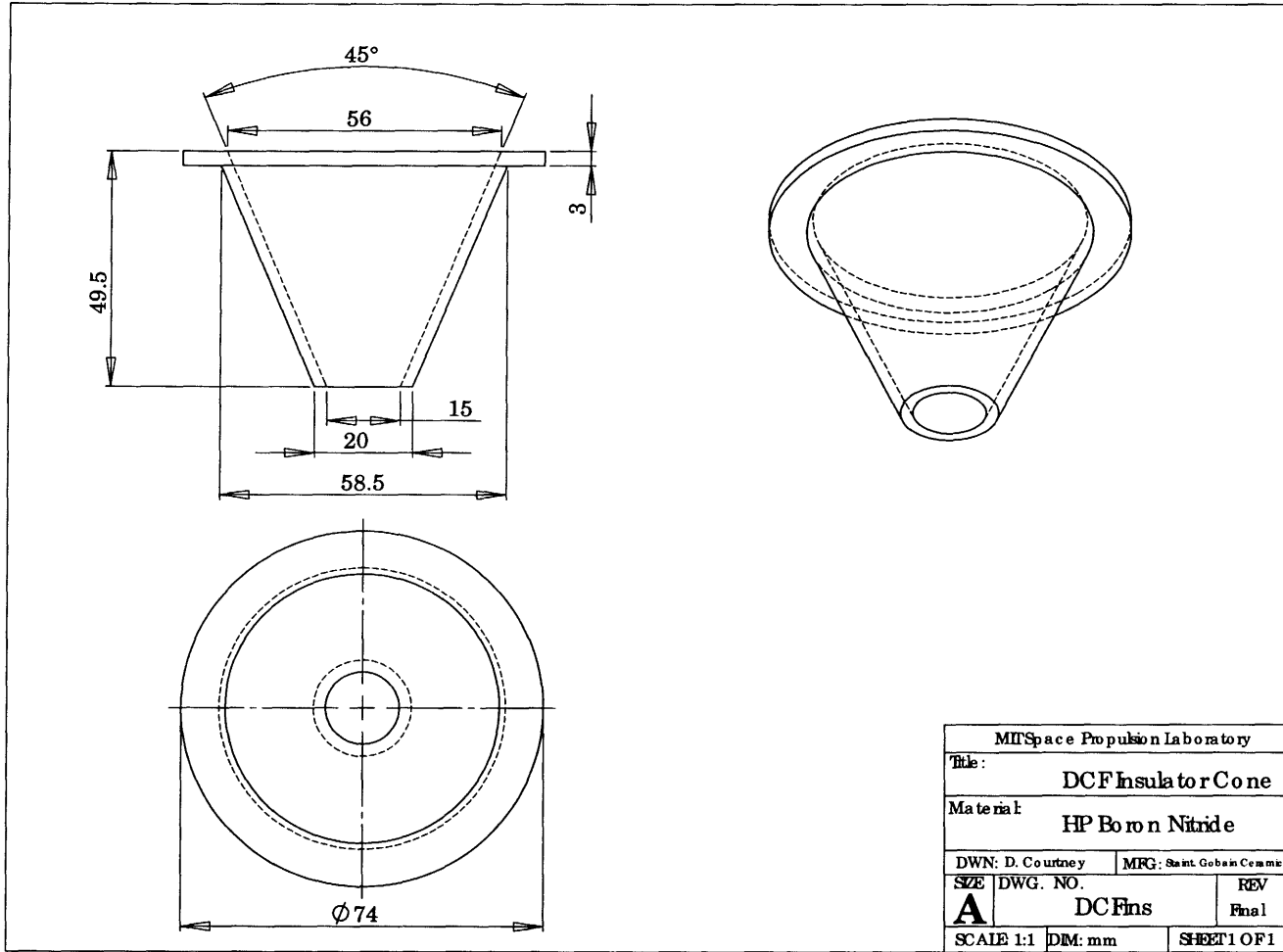
MIT Space Propulsion Laboratory		
Title: **DCF Insulator Cone**		
Material: **HP Boron Nitride**		
DWN: D. Courtney	MFG: Saint Gobain Ceramics	
SIZE **A**	DWG. NO. **DCFins**	REV **Final**
SCALE 1:1	DIM: mm	SHEET 1 OF 1

2

1

Back Plate:
316 Stainless Steel

Base Plate:
316 Stainless Steel

Support Bracket:
Aluminum

Insulator Cap:
Aluminum

160

9.1

Ø4.3

82

6.4

6.4

12.5

82

25

Tap: 8-32 x 3

4.8

82

Ø3

68

7

10

Hole Pattern:
6 x # 9 Drill
Thru Hole

R36

Ø3

R41

Ø4

75

18.9

31   31

10

Ø4.5

Ø9.1

8-32 screw
Thru holes
W/ Cntrsink

75

31

31

82

25

31   31

4.8

25

Tap: 8-32 x 3

Ø88

MIT Space Propulsion Laboratory

Title:
DCF Support

Material:
As Indicated

DWN: D. Courtney   MFG: D. Courtney

SIZE
A

DWG. NO.
DCF ext

REV
Final

SCALE 1:2   DIM: mm   SHEET 1 OF 1

2

1

Cathode Support
Assembly Cylinder

6.4

12.7
30.5
6 x 4-40
Thru Holes
On 53.2mm Dia.

22.3
Ø6.4
140
6.4

10-24 Thru Hole
Channel
Countersink
as needed

10

12.5
36
10
61

250

Ø64
82

MIT Space Propulsion Laboratory		
Title:		
DCF Misc. Parts		
Material:		
Aluminum		
DWN: D. Courtney	MFG: D. Courtney	
SIZE	DWG. NO.	REV
A	DCFmisc	Final
SCALE 1:2	DIM: mm	SHEET 1 OF 1

2
1

Appendix B

MIT Lanthanum Hexaboride Hollow Cathode Drawings

Cathode Tube

Ø13

Ø8

Rear View

3 x 0-80
Thru Hole
#52 Drill

Ø25

Ø14

3 x 0-80
Thru Hole
#52 Drill

Ø21

Ø12.5

Rear View

Chamfer Orifice
to suit AR
(Angle Not Crucial)

Ø3

Ø1.8

Tube Shunt

10.4

Keeper

5

Chamfer Orifice
to suit AR
(Angle Not Crucial)

Ø1

1

6

1.5

44

28

Ø3

5

4

1.7

1.5

38

4

34
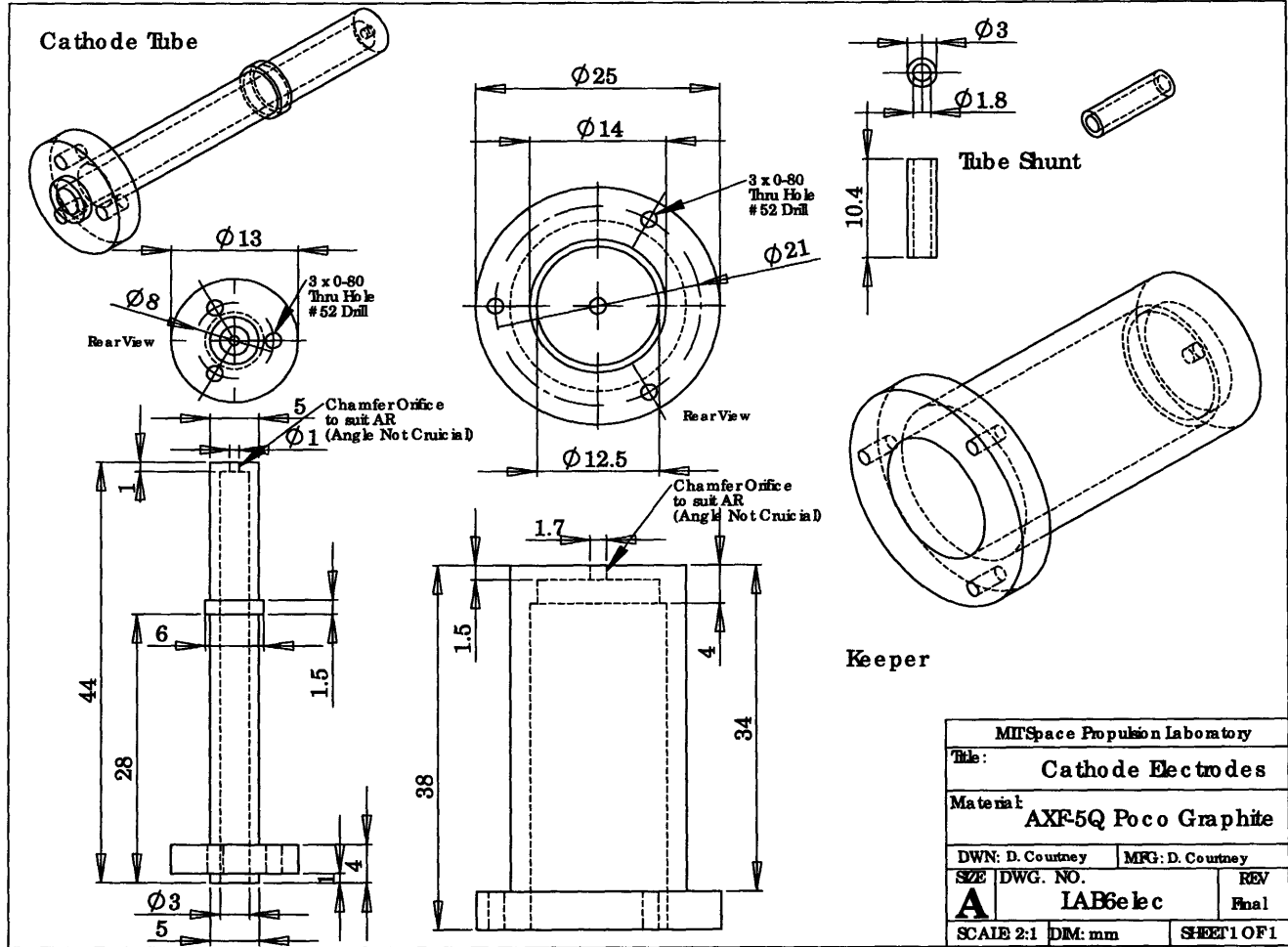
MIT Space Propulsion Laboratory		
Title: Cathode Electrodes		
Material: AXF-5Q Poco Graphite		
DWN: D. Courtney	MFG: D. Courtney	
SIZE **A**	DWG. NO. IAB6elec	REV Final
SCALE 2:1	DIM: mm	SHEET 1 OF 1

2

1

Heater

Heater Sheath

5/16-24 Thread
Cut thread onto
undersize dia.

13.5

12

Ø5

6.6

Ø7.3

14

Ø7.3

Ø9.3

MIT Space Propulsion Laboratory		
Title:	Cathode Heater	
Material:	HP Boron Nitride	
DWN: D. Courtney	MFG: D. Courtney	
SIZE	DWG. NO.	REV
A	IAB6heat	Final
SCALE 4:1	DIM: mm	SHEET 1 OF 1

2

1

14.5
5
2.5
10
7
6
Ø2.9
5
25

12.5
Ø7
2
25

3 x 0-80
Thru Hole
52 Drill

Ø21

2

25°

3 x 0-80
Thru Hole
52 Drill

Ø8

3 x 0-80
Thru Hole
52 Drill

Ø21

MIT Space Propulsion Laboratory		
Title : Cathode Insulators		
Material: 960 Cotronics Machinable Alumina		
DWN: D. Courtney	MFG: D. Courtney	
SIZE A	DWG. NO. LAB6ins	REV Final
SCALE 2:1	DIM: mm	SHEET 1 OF 1

2

1

Insert
Lanthanum Hexaboride

Insert Spring
Tungsten Wire

Keeper Elec. Insulator
HP Boron Nitride

Heat Shield
NOTE: 2:1 Scale
Tantalum Foil 0.01" Thick

$\emptyset 2.71$

$\emptyset 0.51$

$\emptyset 12$

3

7.11

$\emptyset 1.31$

$\emptyset 1.61$

4

$\emptyset 2$

37

12.50

MIT Space Propulsion Laboratory		
Title: Cathode Misc.		
Material: As Indicated		
DWN: D. Courtney	MFG: D. Courtney	
SIZE A	DWG. NO. IAB6misc	REV Final
SCALE 5:1	DIM: mm	SHEET 1 OF 1

2   1

40

5

1

10

6

4.50

Ø2

Fuel Line Inlet
Adjust to suit pipe dia.
Weld Line in Place

4 x 4-40 Tap
#41 Drill

Ø21

Ø8

Ø33

3 x 2mm dia.
Supports Insalotrs
See LAB6misc

3 x 0-80
Thru Hole
#52 Drill
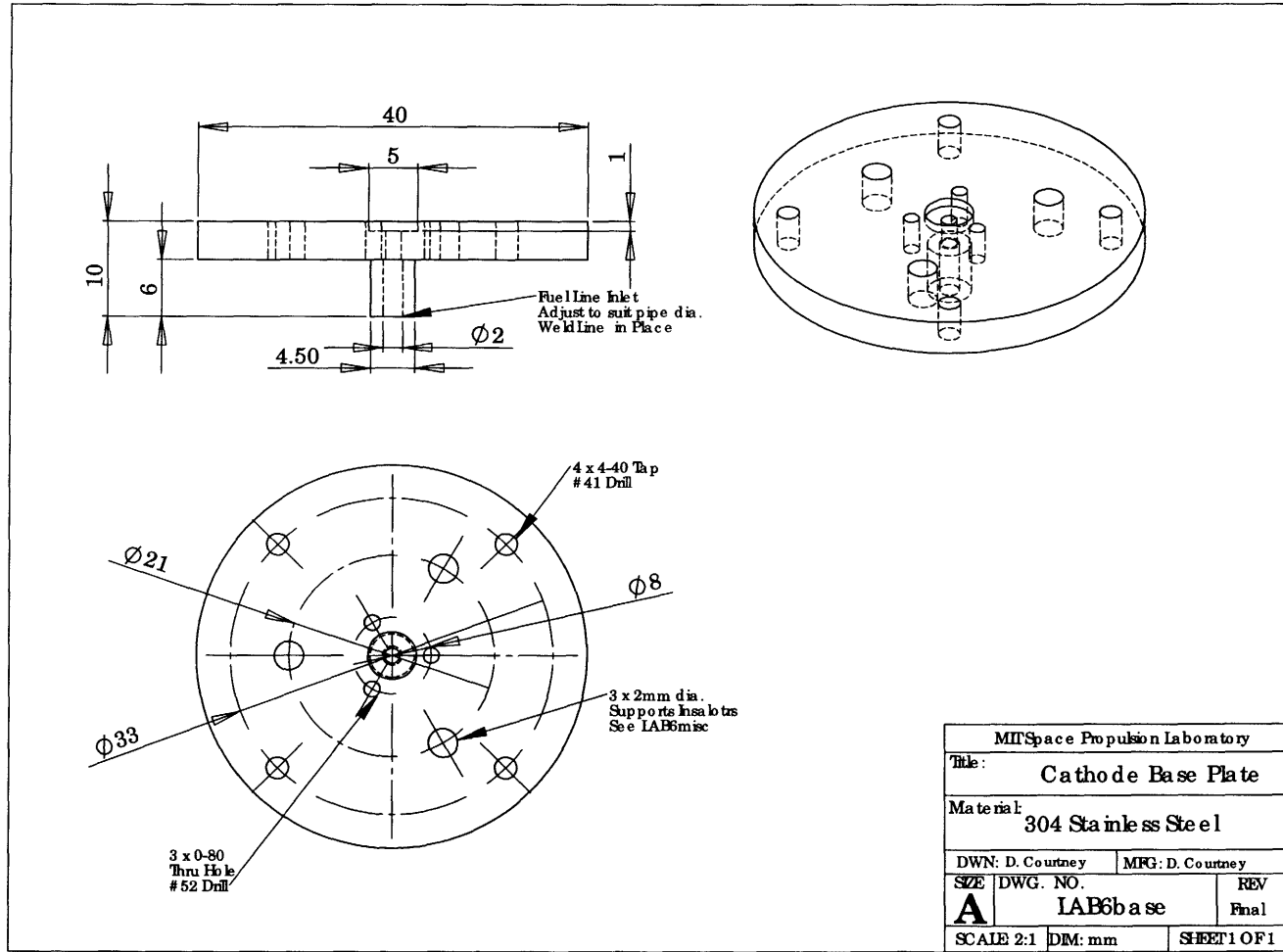
MIT Space Propulsion Laboratory			
Title : Cathode Base Plate			
Material: 304 Stainless Steel			
DWN: D. Courtney		MFG: D. Courtney	
SIZE A	DWG. NO. LAB6base		REV Final
SCALE 2:1	DIM: mm		SHEET 1 OF 1

2

1

Appendix C

SmCo Magnet Data Sheet

DEXTER
Magnetic Technologies

S3212

BH_{max} = 32 MGOe
B_r = 11.5 kG
H_{ci} = 12.0 kOe
H_c = 10.0 kOe
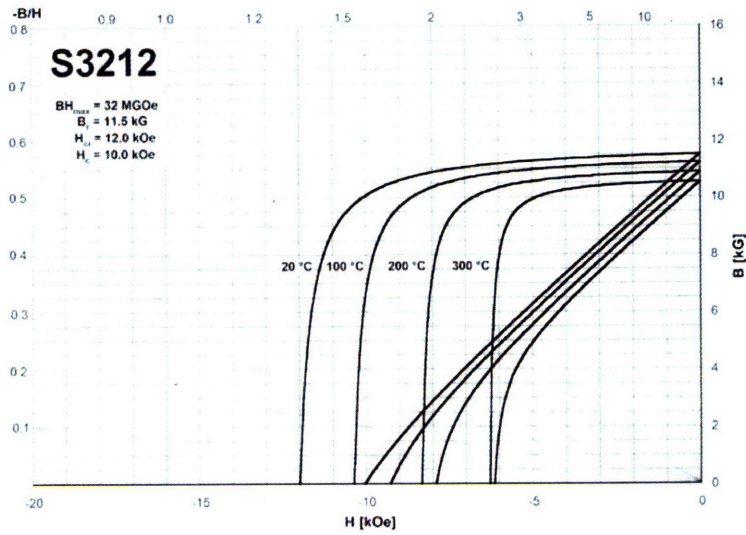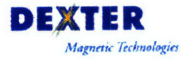
Grade	Maximum Energy Product BHmax	Residual Induction Br	Minimum Intrinsic Coercivity Hci	Coercivity Hc	Maximum Operating Temp Tmo	Curie Temp Tc	Coefficient Induction 20-150 °C] α	Coefficient Coercivity 20-150 °C] β
	MGOe	kG	kOe	kOe	°C	°C	% / °C	% / °C
S3212	32	11.5	12	10.0	300	825	-0.03	-0.17

170